VO_2-BASED MEMS MIRROR

By

David Torres-Reyes

A DISSERTATION

Submitted
to Michigan State University
in partial fulfillment of the requirements
for the degree of

Electrical Engineering – Doctor of Philosophy

2017

ABSTRACT

VO$_2$-BASED MEMS MIRROR

By

David Torres-Reyes

This work presents the design, fabrication, and characterization of the first micro-electro-mechanical-systems (MEMS) mirrors where the actuation mechanism is based on the structural phase-change of smart material thin films monolithically integrated within the device. MEMS mirrors are microstructures with a reflective layer used to redirect incident light. They can be actuated by different techniques including electrostatic, electromagnetic, piezoelectric, and electrothermal mechanisms. In this work, the mechanical actuation of the device's platform (i.e. tilting angle and vertical displacement) is achieved by mechanical stress generated during the structural phase transition of a vanadium dioxide (VO$_2$) thin film. VO$_2$ is a smart material with a solid-to-solid phase change transition at temperatures in the vicinity of 68 °C, that shows hysteretic behavior spanning about 10 °C. During the transition, the crystal structure of the VO$_2$ changes from monoclinic to tetragonal. Consequently, the optical, electrical, and mechanical properties of the material change drastically. Since the transition temperature is very close to room temperature, VO$_2$ can be integrated into MEMS devices lowering the power needed for maximum actuation. The device is operated electro-thermally through integrated resistive heaters, and its behavior is characterized across the phase transition of VO$_2$. Individual actuation of each actuator allows for mirror tilting, while simultaneous actuation of the four legs allows for vertical displacement of the mirror platform. The integration of VO$_2$ into the device allows for the programming of mechanical displacement for tilting angles and vertical displacements.

To my wife, family and friends, for their unconditional support.

ACKNOWLEDGMENTS

I would like to first thank my advisor and mentor Dr. Nelson Sepulveda for all his support and encouragement throughout the years I have known him. Dr. Sepulveda has been a great inspiration to my professional development and has provided valuable technical, professional and research guidance. I would not be where I am today without his continued support.

Additionally, I thank all the current and past members of the Applied Materials Group for their friendship, guidance, and input. I would specifically like to thank Dr. Rafmag Cabrera and Dr. Emmanuel Merced for their training and support when I first joined the lab. Special thanks to Tongyu Wang and Dr. Wei Li, for their support, friendship, and helpful discussions. I am deeply grateful to the support of the members of the Smart Microsystems Laboratory who have provided valuable collaborations in the development of this thesis. I am also appreciative to Dr. Xiaobo Tan for his insights and advice during the development of the VO_2 MEMS mirrors and through my research career. Special thanks go to Dr. Jun Zhang for sharing his expertise in modeling and compensation of hysteresis systems.

I am grateful for the support from the members of my graduate committee; Dr. Xiaobo Tan, Dr. Tim Hogan, and Dr. Chong-Yu Ruan. I would also like to thank the Science, Mathematics, And Research for Transformation (SMART) Scholarship for Service Program for funding my final year in my Ph.D. studies. Thanks to the Air Force Research Laboratory at Wright-Patterson Air Force Base for technical support during the fabrication of the VO_2 MEMS mirrors. I would specifically like to thank Sarah Dooley and Dr. John (Jack) Ebel for their invaluable input and contributions to this thesis project. Additionally, I would like to thank the SLOAN organization for their support, in particularly to Dr. Pierre.

Finally, I would like to thank my wife for her unconditional support and encouragement through my Ph.D. studies. Thanks also to my family and friends for believing in me and providing great emotional support along the way.

TABLE OF CONTENTS

LIST OF TABLES

LIST OF FIGURES

CHAPTER 1

INTRODUCTION

Vanadium dioxide (VO_2) is a smart material that goes through a solid-to-solid phase transition which can be induced by an increase of temperature with a transition temperature of ~68 °C. During its phase transition, VO_2 experiences a fully reversible crystallographic transformation, through which the electrical [19], optical [20] and mechanical [21] properties change drastically. The changes in mechanical properties are caused by a decrease in the area of the thin film crystals that are parallel to the substrate. Therefore, the generated force and deflection is higher for highly oriented films. This process generates stress levels close to $-510\,\mathrm{MPa}$ and strain energy densities in the order of $10^6\,\mathrm{J\,m^{-3}}$, which is close to 1 order in magnitude larger than values for electrostatic or piezoelectric actuation [15]. Given the large work-per-unit-volume, memory capability, and small temperature window during which the phase transition occurs (spanning about 10 °C), VO_2-based micro actuators have been studied extensively in recent years [21, 22, 23, 24, 25, 26, 27, 15, 17, 28, 29, 1, 16, 30]. Furthermore, the behavior of VO_2 across the phase transition shows hysteresis, which has made the development of programmable micro-electro-mechanical-systems (MEMS) actuators [17] and resonators possible [24]. Although there are multiple solid-solid phase transition materials, VO_2 is the material with phase transition temperature closest to room temperature [31], reduces the power consumption for most practical applications.

This work presents the integration of VO_2 into rather complex 3D MEMS devices and used as the actuation mechanism for MEMS mirrors, resulting in the development of, the first VO_2-based MEMS mirrors. MEMS mirrors have been the subject of research in the past decades [32, 33, 34, 35, 4, 36, 37, 38, 39, 40, 5, 41, 42, 43, 44, 45, 46, 8, 47, 48, 49, 50, 51, 52, 10, 53, 54, 3, 55, 56, 57, 9, 58, 59, 60, 7, 61, 62, 2, 63, 64, 65, 66]. The most common actuation mechanism implemented on these devices are: electrostatic [33, 34, 35, 5, 43, 47, 54, 59, 65], electromagnetic [41, 40, 42, 44, 48, 7, 64], piezoelectric [8, 49, 9, 66] and electrothermal [45, 46, 67, 11, 51, 10, 3, 57, 62]. The conventional electrothermal actuation is based in the difference of thermal expansion coefficient (TEC) between two materials. When two materials of different TEC are in physical contact and subjected to a temperature gradient, they expand (or contract, depending on the sign of their TEC) at different rates, creating mechanical bending. This process can require temperature variations of up to 300 °C for maximum actuation [46, 11, 10, 62]. Since the phase transition of VO_2 occurs at 68 °C and spans only about 10 °C, replacing the thermal expansion difference mechanism with the phase change of VO_2 is expected to reduce the required power to actuate the MEMS mirror device.

1.1 Problem Description and Motivation

VO_2 is not a common material used in standard micro-fabrication. This complicates the integration of the material in MEMS, and the use of the drastic changes of the material's properties for increasing device performance. Even if a VO_2 thin film survives a microfabrication process its quality can be affected by common chemicals and processes used during micro-fabrication. In this work, VO_2 thin films were successfully integrated into the fabrication process of MEMS mirrors. The characterization of such device is presented, together with discussions on device performance and the use of its hysteretic behavior for programming of tilting angles and vertical displacements. The problems addressed in this work are:

- Integration of VO_2 thin films in the design and fabrication of a MEMS mirror with monolithic resistive heater.
- The characterization of the MEMS mirror actuators across the transition during individual actuation of each element (i.e. angular tilting rotation) and synchronous

actuation of the 4 elements (i.e. vertical piston-like movement) in terms of quasi-static and dynamic responses.

- Increasing energy efficiency of electrothermal MEMS mirror devices.
- The derivation of a mathematical model to describe the actuation of the VO_2-based MEMS mirror, based on theoretical simulations and experimental measurements of the device.
- The demonstration of memory capabilities on the VO_2-based MEMS mirror, where tilting angles and vertical displacements were programmed by using electrical pulses.

A series of experiments, simulations and analytical approaches are used to address these problems. Additionally, the techniques used for the fabrication and characterization of these devices can also be used to develop more complex VO_2-based MEMS devices. Furthermore, the mathematical model presented, can also serve as a platform for the design of other MEMS mirrors devices to be operated by any electro-thermal process –i.e. not limited to the use of phase-change materials.

1.2 Thesis Statement

The main contribution of this work is the demonstration of a new thermal actuation mechanism for MEMS mirrors and the fabrication of a complex MEMS device with VO_2. Although VO_2-based MEMS actuators have been reported before [15, 16, 30, 17, 24, 1, 29], the monolithic integration of VO_2 thin films in rather complicated 3D MEMS devices, such as MEMS mirrors, has not been demonstrated. The microfabrication process for the present VO_2-based MEMS mirror is discussed in detail. The characterization of the device includes vertical displacement, tilting angle, dynamic response, and power consumption. Furthermore, a mathematical model is derived to describe the movement of the device. Finally, different programmable states are demonstrated for two different actuation modes: angular tilting rotation and piston-like movement by exploiting the intrinsic hysteretic behavior of VO_2.

Thesis Statement: *The development of the first monolithic VO_2-based micro-electro-mechanical mirror is achieved through the successful integration of VO_2 thin films in the fabrication process, resulting in a multifunctional, low-power, programmable MEMS mirror device.*

1.3 Research Contributions

In this dissertation, the problems described in **Section 1.1** will be addressed. A discussion of integrating VO_2 thin films on complex micro-fabrication will provide a reference for future VO_2-based MEMS devices. Moreover, characterization of the VO_2-based MEMS mirror will demonstrate the advantages of integrating VO_2 thin films to such devices, including a power consumption reduction for a similar displacements compared to other actuation mechanisms based on resistive heating, and the capability to create programmable MEMS mirrors.

1.4 Outline

The remaining of this thesis proposal is organized as follows: Chapter 2 presents an overview of micro-mirror technologies with a thorough background on currently used actuation methods, performance, advantages, and applications. The chapter ends with a review of VO_2, the explanation of the mechanism that generates bending in VO_2 MEMS, and the current state-of-the-art in VO_2 based actuators. In Chapter 3, the design and fabrication of VO_2-based MEMS mirrors is presented, starting with device simulation and ending with successfully fabricated devices. The fabrication process flow is clearly described and the challenges are discussed. In Chapter 4, the device is characterized for two different movements: angular tilting rotation and vertical piston-like movement. In Chapter 5, a mathematical model is derived from a combination of analytical methods, numerical simulations and experimental results. The model incorporates the linear and non-linear behavior of the system, where the non-linear behavior is captured with a Preisach algorithm. In Chapter 6, programmable mechanical states for the two movements (angular tilt and vertical piston) are demonstrated by programming two different states. Furthermore, the capability to have multiple programmables states by applying different input sequences is demonstrated. Finally, Chapter 7 shows a summary of contributions of this work.

CHAPTER 2

BACKGROUND

2.1 Micro-mirror

In the past few decades MEMS mirrors have been a subject of research [32, 33, 34, 35, 4, 36, 37, 38, 39, 40, 5, 41, 42, 43, 44, 45, 46, 8, 47, 48, 49, 50, 51, 52, 10, 53, 54, 3, 55, 56, 57, 9, 58, 59, 60, 7, 61, 62, 2, 63, 64, 65, 66, 68]. MEMS actuators are micro-devices capable of generating a mechanical displacement with an electrical stimulus. In MEMS mirrors the displacement is used to redirect an incident beam of light to a desired position. Currently, the actuation mechanisms implemented on these devices are: electrostatic [33, 34, 35, 5, 43, 47, 54, 59, 65], electromagnetic [41, 40, 42, 44, 48, 7, 64], piezoelectric [8, 49, 9, 66] and electrothermal [45, 46, 67, 11, 51, 10, 3, 57, 62]. An actuation mechanism can be driven by directly applying a force to the frame of the mirror (direct drive) or by applying the force through a mechanical coupling to amplify the displacement of the mirror (indirect drive). Depending on the mechanical movement generated, MEMS mirrors can be classified by either one (1D) or two (2D) dimensional movement, as shown in **Figure** 2.1. A 1D mirror can reflect the light to create a 1D image, while a 2D mirror can create a 2D image. Additionally, a Tip-Tilt-Piston (TTP) mirror is a different type of MEMS mirror that combines the 2D movement with the capability of changing the elevation of the mirror with a piston-like movement, as shown in **Figure** 2.2.

MEMS mirrors have a variety of applications in multiple fields, including optical phase arrays [37, 10] spectroscopy [51], optical switches [69], track-positioning [67], scanners [70], microscopy [71], optical displays [35, 48] and medical imaging [57, 60, 72]; the last two examples are shown in **Figure** 2.3. Given the wide range of applications for MEMS mirrors, it is difficult to choose a figure of merit that can describe the performance of the devices. The

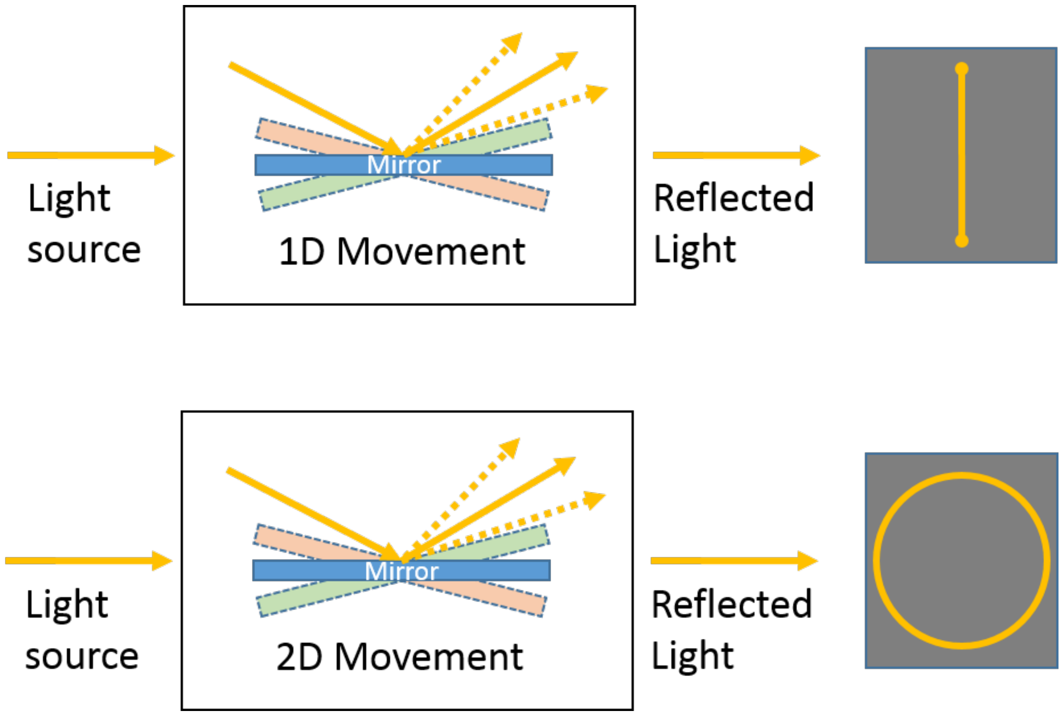

Figure 2.1 1D and 2D movement mirrors with resulting image created by each movement.
.

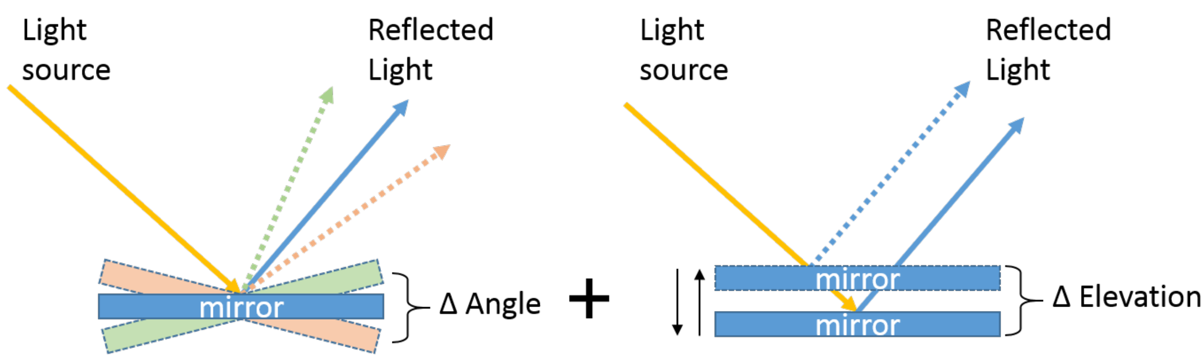

Figure 2.2 Tip-tilt piston mirror movement.

best properties of a mirror will depend on the specific application. For example, a large tilt angle is essential for microendoscope and scanning tracking applications to increase the field of view. Other cases such as projections, need very fast movement but do not require a large tilt angle [32, 4]. However, regardless of application, power consumption is always a concern and should be reduced as much as possible. Although it can be argued that increasing displacements/tilting angles and decreasing power consumption will result in better MEMS mirrors; the technologies that have been used for these devices do not include a single mechanism that can optimize both [63]. Even-though different mechanisms can achieve a reduction of power consumption, such as piezoelectric and electrostatic actuation, they usually require high voltage (for example: 115 V and 40 V for electrostatic and piezoelectric, respectively) [65, 66].

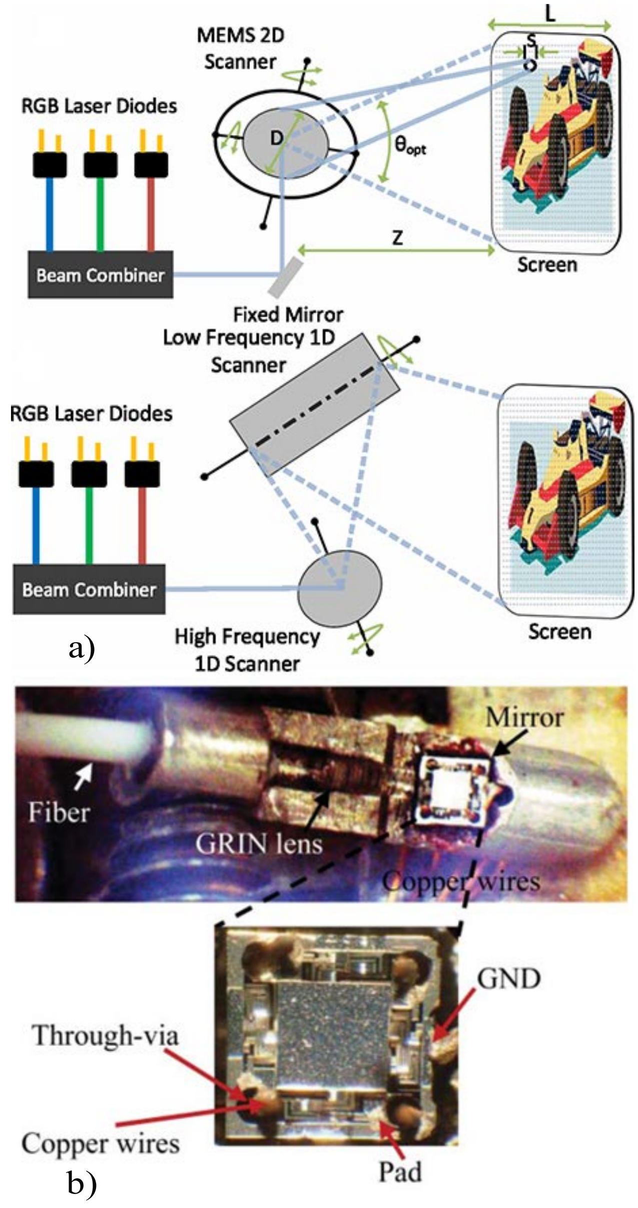

Figure 2.3 MEMS mirror applications examples: a) MEMS mirrors array used to created optical projection [2], b) MEMS mirror used in an endoscope, increasing the field of view without the movement of the instrument [3].

2.1.1 Actuation Mechanism

The actuation mechanism is the main factor that determines MEMS mirror performance. Indeed, the device design is based on its actuation mechanism and affects the device fabrication process flow. One important aspect for the fabrication of the devices is the compatibility of the design with standard micro fabrication processes, such as the one use in complementary metal-oxide semiconductor (CMOS). The most common actuation mechanisms that have been implemented with MEMS mirrors are described below.

2.1.1.1 Electrostatic

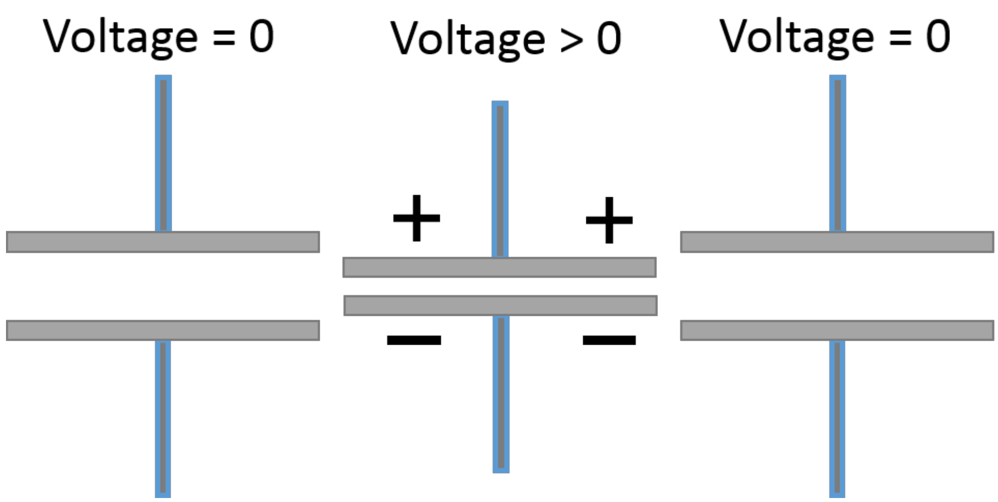

Figure 2.4 Electrostatic actuation mechanism between two conductive plates, where a differential voltage create an attraction force between the plates.

The electrostatic actuation method, relies on the repelling/attracting forces of two oppositely charged plates to move the mirror platform from a resting state [73] (see **Figure** 2.4). The two most common and effective configurations for this mechanism are the parallel-plate actuation [34, 35, 43, 54] and the comb drive (an array of parallel plates interlocked with each other to increase tilting angle), examples of these configurations are shown in **Figure** 2.5 [33, 5, 47, 59, 65]. The displacement generated using these methods is proportional to the change in capacitance between the plates, therefore, you can control the displacement by measuring the capacitance [33]. The speed of the mechanism will be proportional to the variation in voltage at the plates, able to reach frequencies in the of range of 10 kHz [5]. The fabrication process for this method is compatible with the CMOS process since it does not require any unusual materials and can be fabricated using the same technique as the one uses in the CMOS processes. To create the interaction between the parallel plates and generate displacement of the mirror, usually a high input voltage is needed (>20 V) [33, 5, 43, 47, 59, 2, 65]. These devices can sustain very high electric fields due to the distance between charged surface being lower than the mean free path of particles in air at room temperature (∼6 µm) [65]. Since the system is basically an open circuit, only a very low current is consumed to charge the plates, yielding a very low power consumption[2]. However, the downside of this mechanism is that it can only generate low forces. The electrostatic force between the two plates can be expressed as:

$$F_{es} = \frac{A\epsilon V^2}{2g^2}$$

where A is the overlap area of the plates, ϵ is the dielectric constant of the medium (e.g. air), V is the voltage difference applied between the plates and g is the gap between the two plates. This force is limited by the pull-in instability, where the equilibrium position of the frame between the electrostatic and mechanical forces is broken with the increase in voltage causing the collapse of the plates. The limiting voltage (also known as pull-in voltage) is given by:

$$V_{pull-in} = \sqrt{\frac{8kg_0^3}{27\epsilon A}}$$

where the k is the spring constant and g_0 is the initial gap (without actuation) between the plates. This limit the maximum deflection of the plate to 1/3 of the initial gap [74, 75, 76].

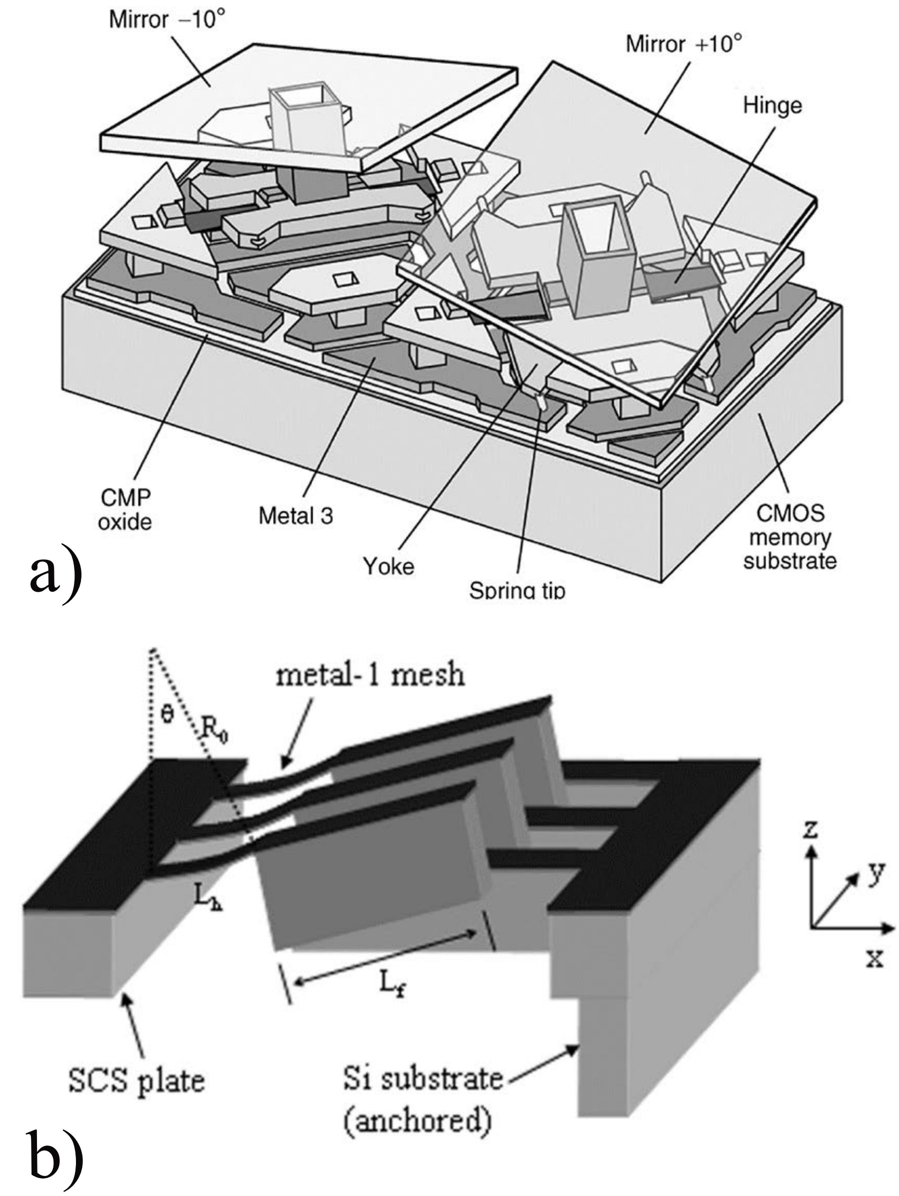

Figure 2.5 Examples of electrostatic MEMS mirror device: a) parallel plate design used by Texas Instrument for displays projection [4], b) a close-up look to the comb drive design [5].

2.1.1.2 Electromagnetic

The electromagnetic actuation method generates movement as the result of the interaction between two magnetic fields,where Lorentz force governs [48]. In this method two design configurations are used: 1) a combination of an external permanent magnet (static magnetic field) and an electromagnetic coil (dynamic magnetic field) are used to generate the two magnetic fields, where the magnitude of the electromagnetic field created by the coil is dependent on the input current (see **Figure** 2.6); 2) a magnetic influenceable material is attached to the mirror and an external moving magnetic field (create by an electromagnetic coil or a permanent magnet) move the device (see **Figure** 2.7) [41, 40, 42, 44, 48, 7, 64]. The inclusion of a permanent magnet on either design configuration limits the minimum size of the design. Its fabrication process can be CMOS compatible, depending on the design configuration that is implemented where the magnetic materials are incompatible with CMOS processes; as an example the material can be added after the fabrication [7].

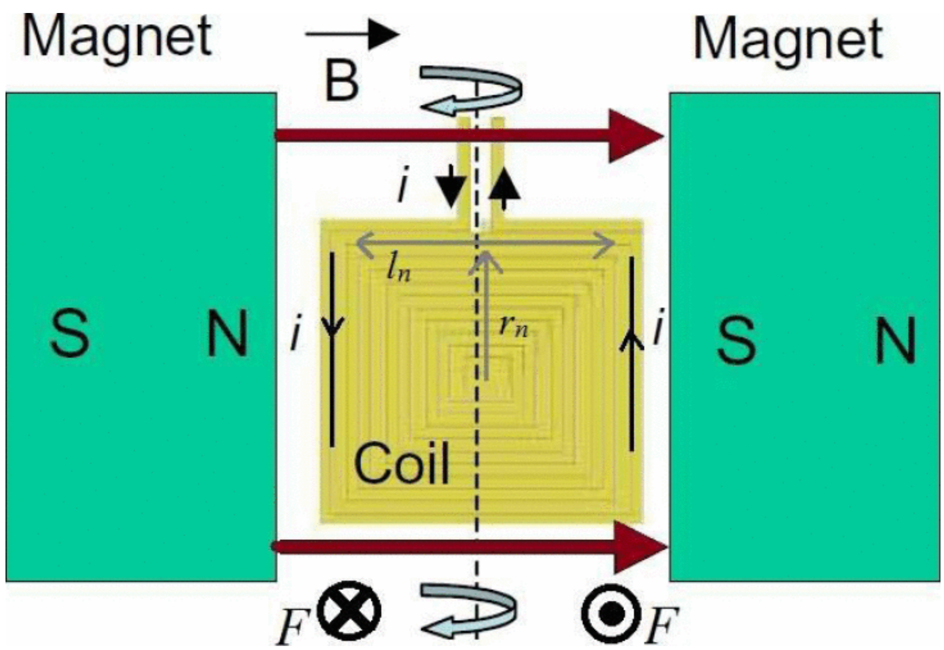

Figure 2.6 Example of an electromagnetic MEMS mirror device with of a moving coil and permanent magnet outside the device to supply the magnetic field, where B is the magnetic field, F is the force generated by the interaction between B and the electromagnetic field generated from the coil by the current i, r_n and l_n is the electrical resistances and length of the coil, respectively [6].

Another advantage (when using a coil in the device) is the linear relationship between the output (displacement) and the input (electrical signal), this can be used to easily control the output of the mirror. The current necessary to generate an electromagnetic field to move the device can reach values up to 515.17 mA for optimum performance [64]. Although a low voltage is able to induce the desired displacement, the high current needed for this actuation method results in a large power consumption. The following equations can be used to describe this actuation method and are shown in **Figure** 2.6:

$$F_{Lorentz} = Bil$$

$$T_{mag} = 2\sum_{n=1}^{N} Bil_l r_n$$

$$P_{coil} = i_{rms}^2 R_{coil}$$

where $F_{Lorentz}$ is the generated force, B is the magnetic field, i the current, l the length of the conductor, T_{mag} is the generated torque, N the number of the coil turns, r_n the distance of the nth coil turn from the center, P_{coil} is the consume power by a coil, and R the resistance of the coil.

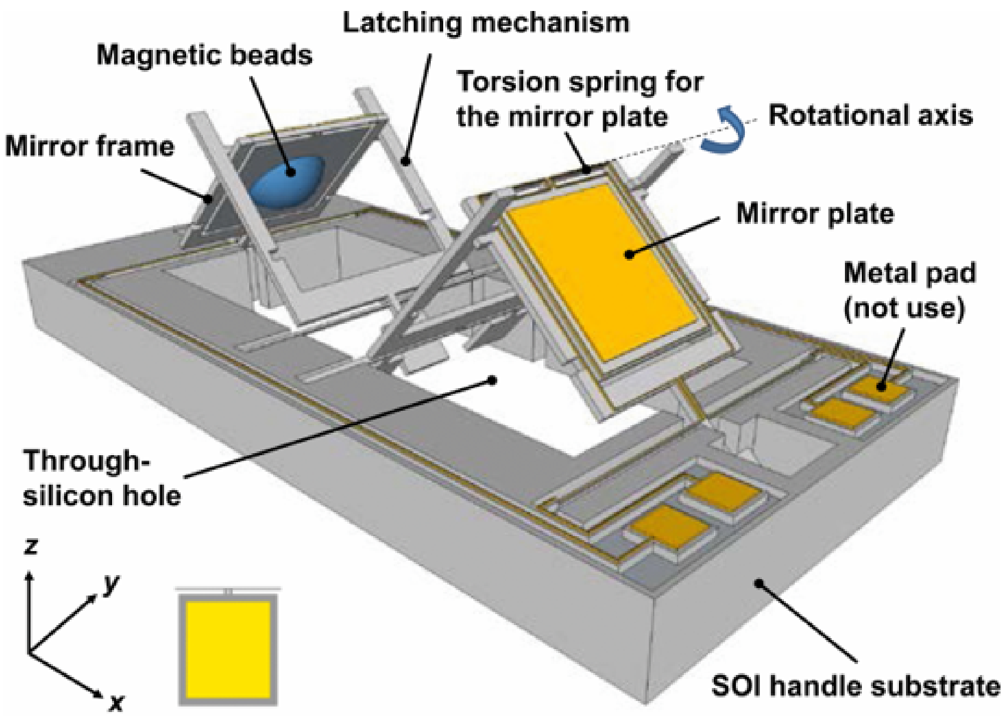

Figure 2.7 Example of an electromagnetic MEMS mirrors device with a moving magnetic material and actuated with an external permanent magnet or with an electromagnet coil [7].

2.1.1.3 Piezoelectric

The piezoelectric actuation is a less commonly used method. It utilizes piezoelectric materials in the design of the device, where the most common material used for actuation is PZT (lead zirconate titanate)[8, 49, 77, 9, 66], due to the higher electromechanical coefficients [78]. The use of these materials can make the fabrication non-CMOS compatible due to contamination of the tools use in the process, damaging any following procedure in the same tool. A complicated approach can be done to avoid contamination with a resolution of 200 µm by 200 µm [53].

The piezoelectric material can expand or contract with a differential voltage across the material. This is because the material contains small unorganized dipoles that can be oriented with an electric field. The change in orientation of the dipoles will cause an expansion/contraction in the material, generating a large force but a small displacement (see **Figure** 2.8).

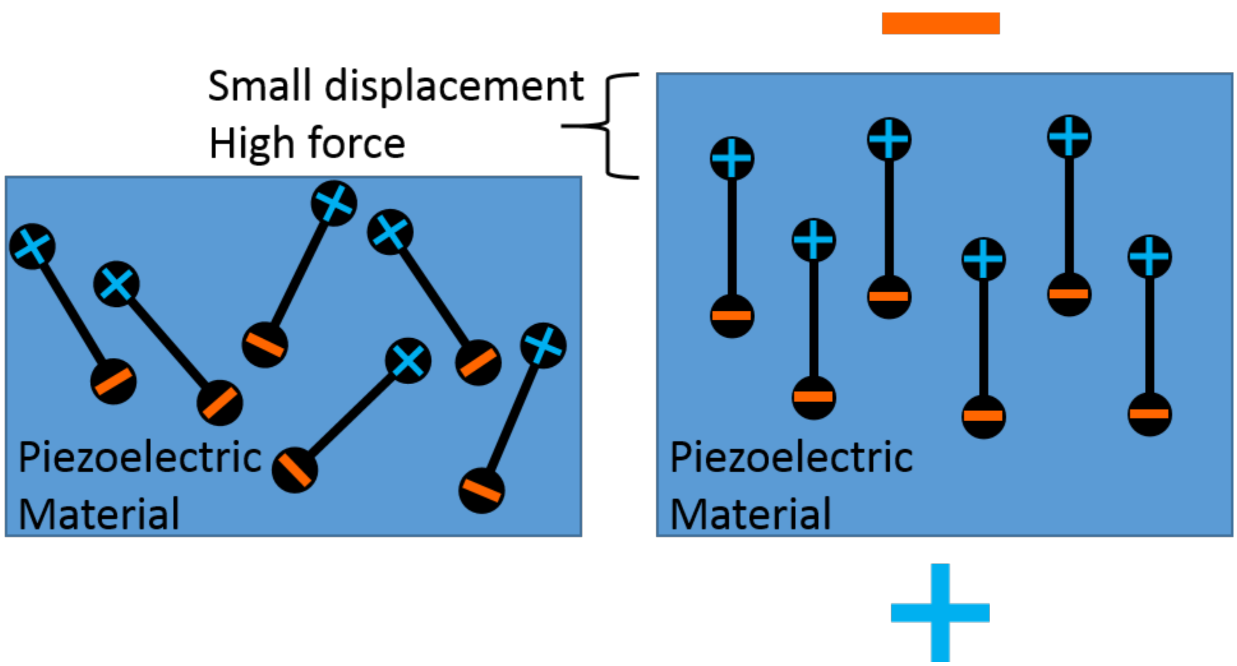

Figure 2.8 Piezoelectric material with internal dipoles, where a differential voltage across the material align the internal dipoles resulting in a expansion of the material.

An example of the mechanical design of this method is shown in **Figure** 2.9a, where two cantilever with piezoelectric material are connected to each other with a torsion bar in the middle, the torsion bar is the mechanical connection to the mirror. Each piezoelectric will work opposite to each other by applying an opposite voltage to each one, making a one material expand while the other will contract, generating stress in the torsion bar and creating a tilting angle on the mirror [8]. This process can be very fast and can generate high forces. However, the total displacement caused by the material alone is very small [2]. To compensate for this, the designs make use of the resonant frequency of the structure in combination with an indirect drive design, where a mechanical coupling increases the amplitude of the deflection. An example of this is shown in **Figure** 2.9b, where the coupling between the bigger and the smaller frame help to increase the amplitude of the tilting angle with a maximum value of 38.5° [9].

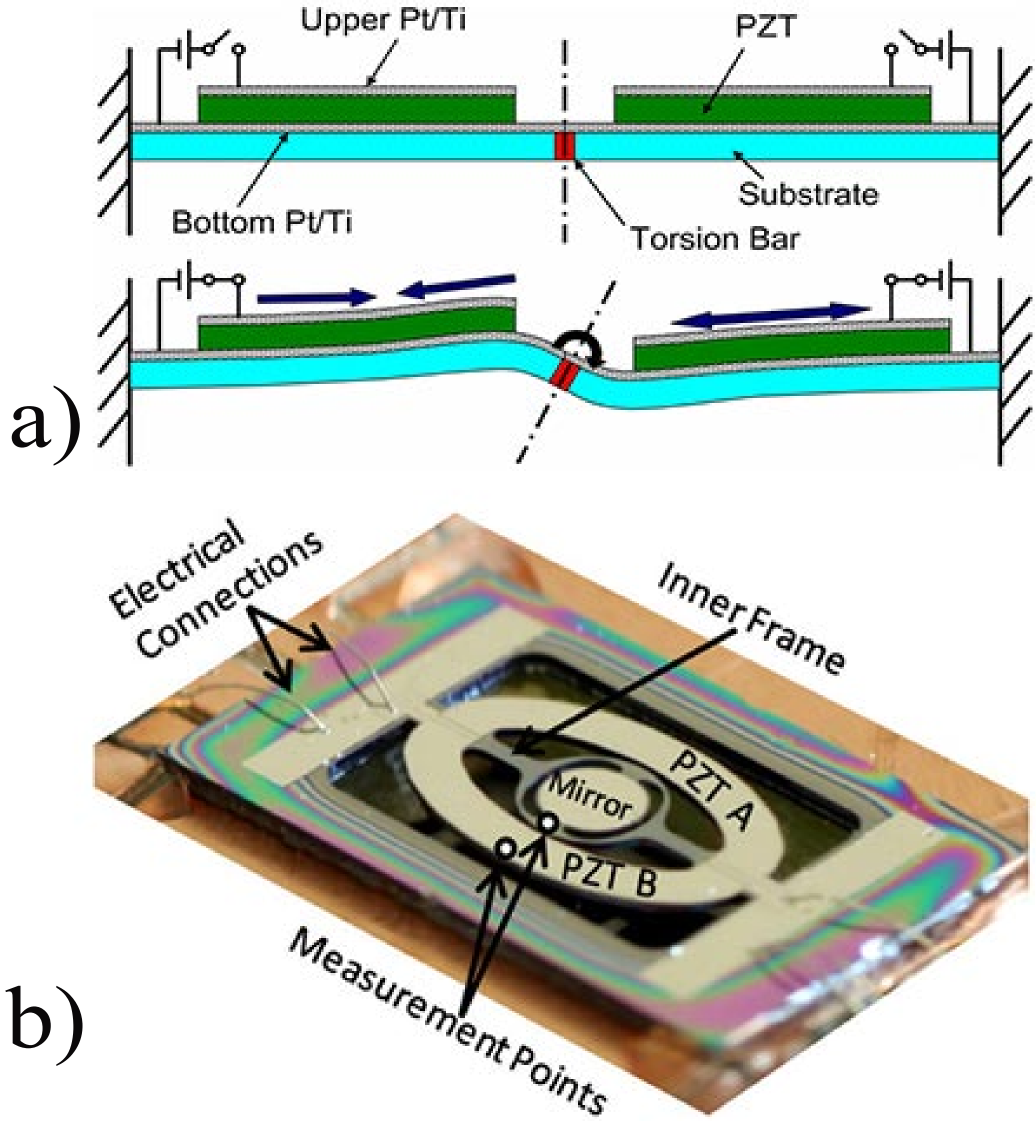

Figure 2.9 Piezoelectric actuation examples: a) the use of piezoelectric material to generate a torque [8], b) piezoelectric MEMS mirror with a mechanical coupling (indirect drive) is used to amplify the tilting angle with a sinusoidal actuation voltage with an amplitude of 24 V as the input [9].

2.1.1.4 Electrothermal

The conventional electrothermal actuation method is based in the thermal expansion of materials, the most common configuration for this mechanism is a bimorph structure formed by two materials (thin films) with different TEC [45, 46, 67, 79, 11, 51, 10, 3, 57, 62]. As the temperature increases, one material will expand more than the other, creating stress in the structure that generates mechanical actuation [45]. In a linear dimension the expansion of the material can be expressed as:

$$\frac{\Delta L}{L_0} = \alpha \Delta T$$

where ΔL is the change in the length of the structure, L_0 is the initial length, α is the TEC and ΔT is the change in temperature (see **Figure** 2.10).

The speeds of previous mechanisms are not constrained by the actuation mechanism because they can be actuated as fast as the input stimuli can change, where the limit of the speed will be held by the mechanical displacement or the mechanical design. For the electrothermal actuation method, the speed will depend on the thermal dynamics of the system, making it the slowest mechanism of all for devices of similar size and thermal mass. The gradient in temperature needed for the actuation of the MEMS mirror device is created by Joule heating with reported values for full actuation reaching up to $\sim 300\,^{\circ}\mathrm{C}$ [10]. The power consumed in this mechanism can be lower than the EM, but higher than the ES and PE, since the temperature increase depends on the amplitude of the applied current, which can be as high as 252 mA (for maximum displacement) resulting in a input power of 301 mW [62]. Additionally, this mechanism can be integrated into very compact devices [11, 10, 3, 57, 62]. Finally, the fabrication process for this mechanism is compatible with the CMOS process. Since the actuation method depends solemnly depend on the used of two common material with different TEC values, this combination can be done with any metal and a glass layer such as aluminum (Al) and silicon dioxide (SiO_2).

2.1.2 Tip-Tilt-Piston Mirror

Among the different MEMS mirror models, a tip-tilt-piston (TTP) mirror has the capability of 2D displacement and a piston movement to change its elevation (see **Figure** 2.2), which can be useful for biomedical applications and optical phase array [10, 36]. One example of this

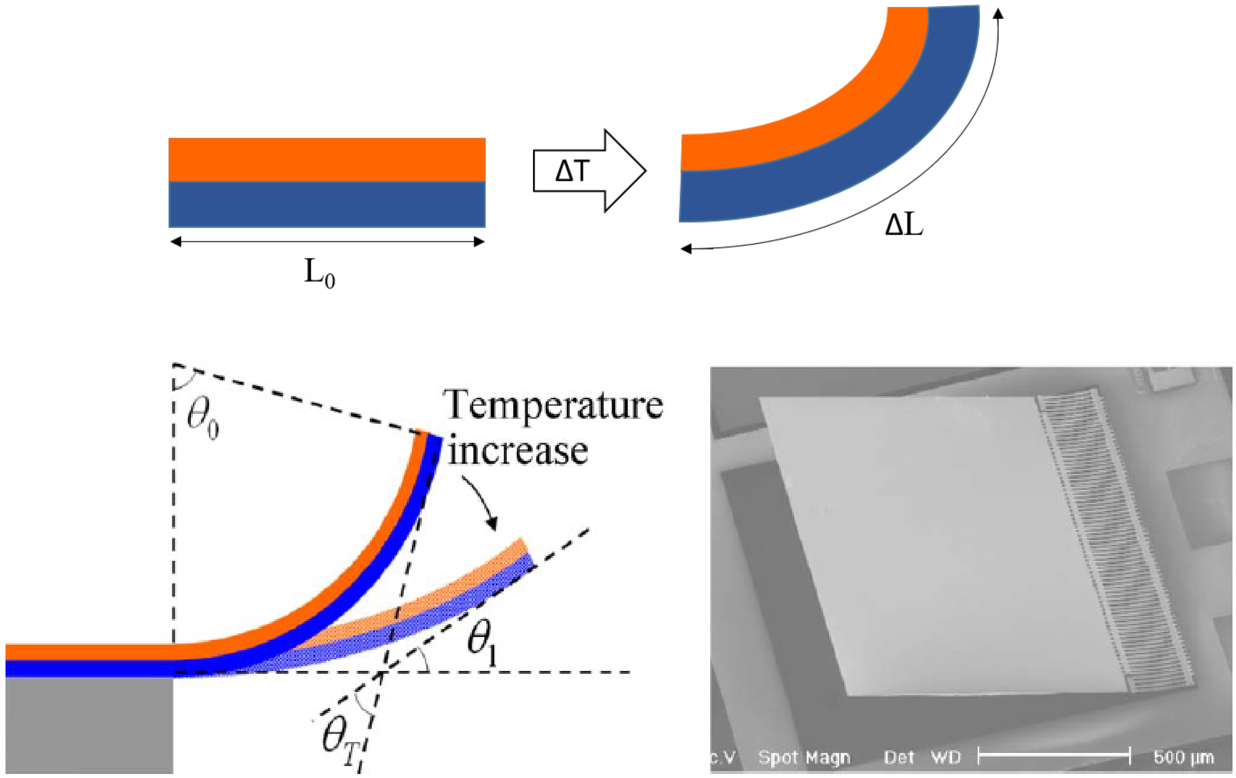

Figure 2.10 Electrothermal actuation example, where the blue layer (bottom) has a larger TEC compare to the other layer [10].

kind of mirror device is presented in [10], where the electrothermal is actuation mechanism. The actuation results from the difference in the TEC between: Al and SiO_2 where the Al will expand more than the SiO_2 for a given temperature gradient (delta T). The temperature used to generate a maximum deflection of ~200 µm is ~350 °C from an input voltage range of 0 - 4.5 V. A downside of this model, is the high electrical power needed to generate this high temperature (i.e. 41 mW for one actuator were required to increase the temperature to ~350 °C in the device reported in [10]).

In this design, a squared mirror platform is suspended by 4 separate and individually-actuated legs (see **Figure** 2.11). Each leg consists of different sections with two different thickness: a thin section with the two materials with the different TEC (bimorph) and a much thicker section (frame) that will provide a rigid frame that serves as a mechanical support to increase the total displacement (indirect drive), as shown in **Figure** 2.12. Each

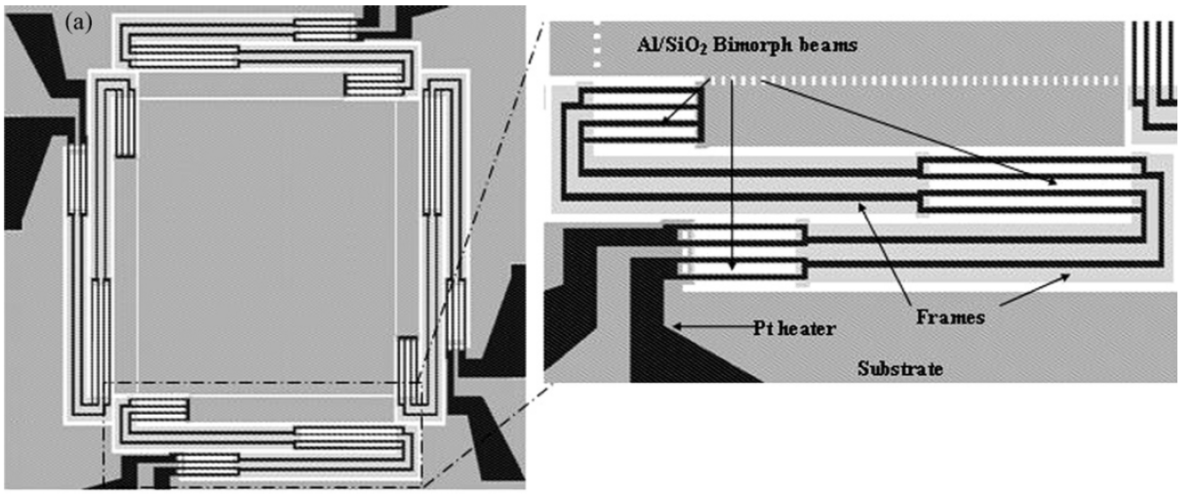

Figure 2.11 TTP actuator design [11].

mechanical leg also has an integrated resistive heater with independent connections, allowing the freedom of moving each leg independently.

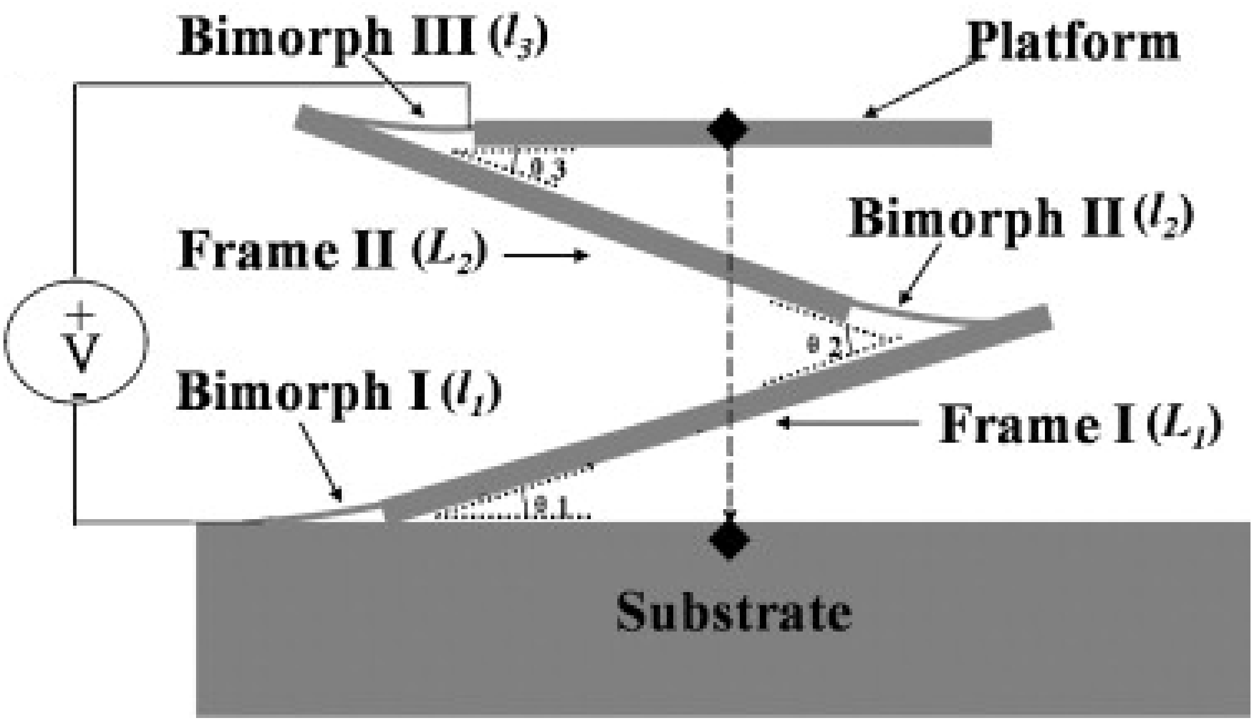

Figure 2.12 Mechanical legs (actuator) showing the bimorph and the frame of the structure[11].

The details of the TTP mirrors are presented in [10, 80, 11] and are explained here. The schematic of the leg actuator is shown in **Figure** 2.12, where the design parameters are the lengths of the frames (L_1, L_2) and bimorphs (l_1, l_2, l_3). To be able to change the elevation of the mirror without any tilting angle , i.e., parallel with the substrate, the following relationship needs to be true:

$$\theta_2 = \theta_1 + \theta_3, \tag{2.1}$$

where θ_1, θ_2 and θ_3 are the arc angles of each bimorphs. According to thermal bimorph actuation, the arc angles are proportional to the length of the bimorphs: $l_2 = l_1 + l_3$ [46]. In order to maintain a flat platform, l_1 and l_3 were chosen to be half of the l_2.

$$l_1 = l_3 = \frac{l_2}{2}, \tag{2.2}$$

which implies that:

$$\theta_1 = \theta_3 = \frac{\theta_2}{2} \tag{2.3}$$

Another undesired displacement during the elevation motion is the lateral shift of the center platform mirror. This is caused by movement of 5 different components shown in **Figure** 2.13: Actuator1, Frame1, Actuator2, Frame2 and Actuator3. The lateral shift (LS) of each component can be describe with the following equations:

$$LS_{actuator1} = l_1 - \frac{l_1 cos\theta_1}{\theta_1} \tag{2.4}$$

$$LS_{frame1} = L_1 - L_1 cos\theta_1 \tag{2.5}$$

$$LS_{actuator2} = l_2 - \frac{l_2 cos\theta_1}{\theta_2} \tag{2.6}$$

$$LS_{frame1} = L_2 - L_2 cos\theta_1 \tag{2.7}$$

$$LS_{actuator3} = l_3 - \frac{l_3 cos\theta_3}{\theta_3} \tag{2.8}$$

The total lateral shifts can be calculated by combining equations (2.2 - 2.3) into equations (2.4 - 2.8) and taking in account that lateral shift from Actuator1, Actuator3 and Frame1 are opposite to the lateral shifts from Actuator2 and Frame2, which gives the following equation for the total lateral shift (as defined in **Figure** 2.13):

$$LS = (L_1 - L_2)(1 - cos\theta_1) \tag{2.9}$$

In summary, to eliminate any lateral shift or tilting in the vertical displacement, the following relationship between the lengths of the bimorph (l_1, l_2, l_3) and the frames (L_1, L_2, L_3) must be satisfied:

$$l_1 = l_3 = \frac{l_2}{2} \tag{2.10}$$

$$L_1 = L_2 \tag{2.11}$$

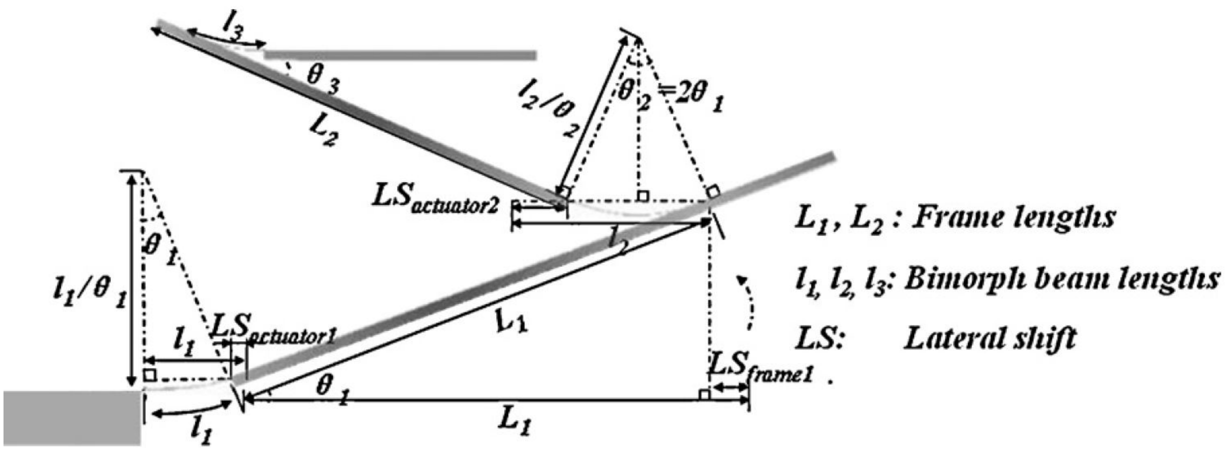

Figure 2.13 A mechanical leg of TTP design with all the parameters used to describe the lateral shift of the platform [11].

2.2 Vanadium Dioxide

Vanadium dioxide is a smart material that has a solid-to-solid phase change transition, which can be induced by an increase in temperature with a transition temperature (T_T) of around 68 °C. This was first observed by [81], where they reported a hysteretic reversible change in the electrical properties of the material with an increase of temperature. During the transition two correlated mechanisms occurred: a crystallographic structure change or [structure phase transition (SPT)] from a monoclinic (M_1) structure at low temperatures (T < T_T) to a rutile tetragonal (R) structure at high temperatures (T > T_T) [82, 83]; and an electrical transition from high resistance to low resistance also known as the insulator to metal transition (IMT) [81, 19].

VO_2 is the only stable state of the vanadium oxides with a (T_T) near room temperature, where V_6O_{13} [84] and V_2O_3 [85] have a T_T of -123°C; and V_2O_5 [86] has a T_T of 280 °C. The T_T of the VO_2 can be shifted to different temperatures by inducing defects in the VO_2 lattice either by substituting vanadium ions (V^{5+} for V^{4+}), or by adding impurities in the systems such as, W, F, Ti, Cr, among others [87, 88, 89, 90, 91]. The VO_2 transition can also be induced by different mechanism including: ultra-fast optical radiation [92], electric-field [93], temperature [81], pressure [94] and extrinsic stress [95, 96, 97]. The method to induce the transition on the proposed devices is by increasing the temperature using Joule heating. The resistance heater are integrated into the device making the device compact and monolithic.

Over the years various methods have been developed for the deposition VO_2 thin films such as: chemical vapor deposition (CVP) [98, 99], sol-gel synthesis [100, 101, 102][103], atomic layer deposition (ALD) [103, 104] and physical vapor deposition (PVD) including pulsed laser deposition (PLD)[103, 105, 106, 107], and sputtering [108, 109]. This work used the PLD technique to deposit the VO_2 thin films on the proposed MEMS mirror. The used of amorphous glass, silicon, quartz, and sapphire (in any crystal orientation) as a substrate, produce highly oriented VO_2 films with the monoclinic $(011)_M$ planes parallel to the substrate surface [24].

During the transition of VO_2 between the two different states (M_1 and R) the optical [20, 110], electrical [82] and mechanical [21, 111] properties change drastically, this has been used to create different applications such as: variable optical attenuators (VOA) [112], mechanical memories [17], controlled resistances [113], actuators [21, 22, 23, 25, 26, 27, 15, 17, 28, 29, 1, 16, 30], resonators [24] and re-configurable antennas [114].

2.2.1 IMT and SPT

Although it is known that two correlated mechanisms occurred during the VO_2 transition (SPT and IMT), the reason is still cause for debate in the VO_2 research community. In [115], the physics behavior of the VO_2 transition is described as a Mott-Peierls transition. In the tetragonal (R) configuration of VO_2, each of the vanadium (V) atoms are surrounded by an octahedron configuration of oxygen (O) atoms. In this configuration the ionic charges of the V are placed in the d energy level, then divided into higher e_g and lower t_{2g} states [12]. The latter is then divided between the $d_{||}$ states along the c axis and π^* states, which are located near the Fermi energy level, causing the low resistance at high temperatures. In the low temperature state (M_1), the V atoms moves in a zigzag-type configuration increasing the energy of the π^* band. At the same time pairs of V atoms are created within the vanadium chain parallel to the rutile c axis, this splits the $d_{||}$ band into filled bonding and empty antibonding states. As a result, a band gap of 0.7 eV is created, which explains the insulator or high resistance phase of the VO_2. This behavior can be seen in **Figure** 2.14.

The SPT (see **Figure** 2.15), responsible for the change in the mechanical properties of the VO_2, occurred after the IMT, since it needs more energy to change the structure from M_1 to R [83]. During the SPT from M_1 to R, the c_R axis lattice decreases by ≈1% while the a_R and b_R increase by ≈0.6 % and ≈0.1%, respectively [12]. VO_2 deposited by PLD technique, has the c axis parallel to the substrates of Si and SiO_2 [22]. The reduction of the area of in the c axis generates a stress on the substrate that has been used as an actuation

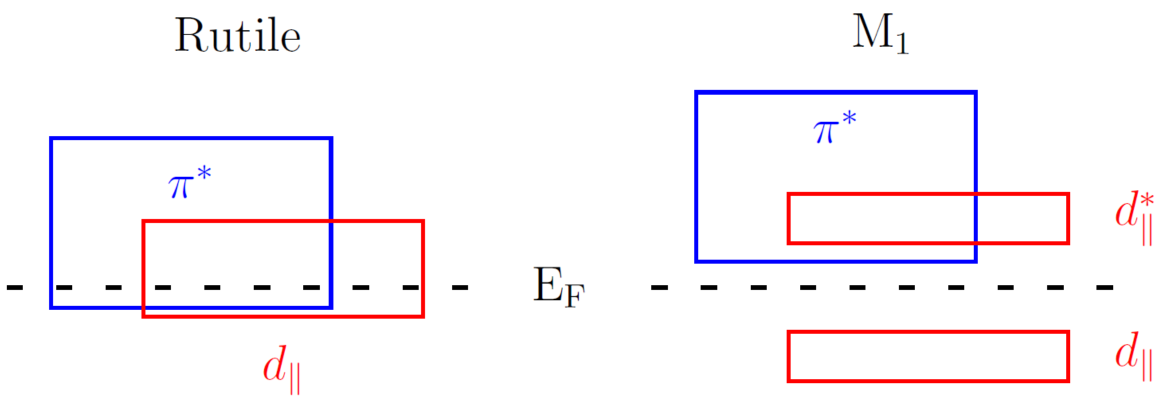

Figure 2.14 Band diagrams of VO_2 at different temperatures [12].

mechanism for micro cantilevers [14, 83]. Also during this process the young modulus of the VO_2 has a change from 156±7.5 GPa for M_1 and an estimated of 110 GPa for the R phase[26].

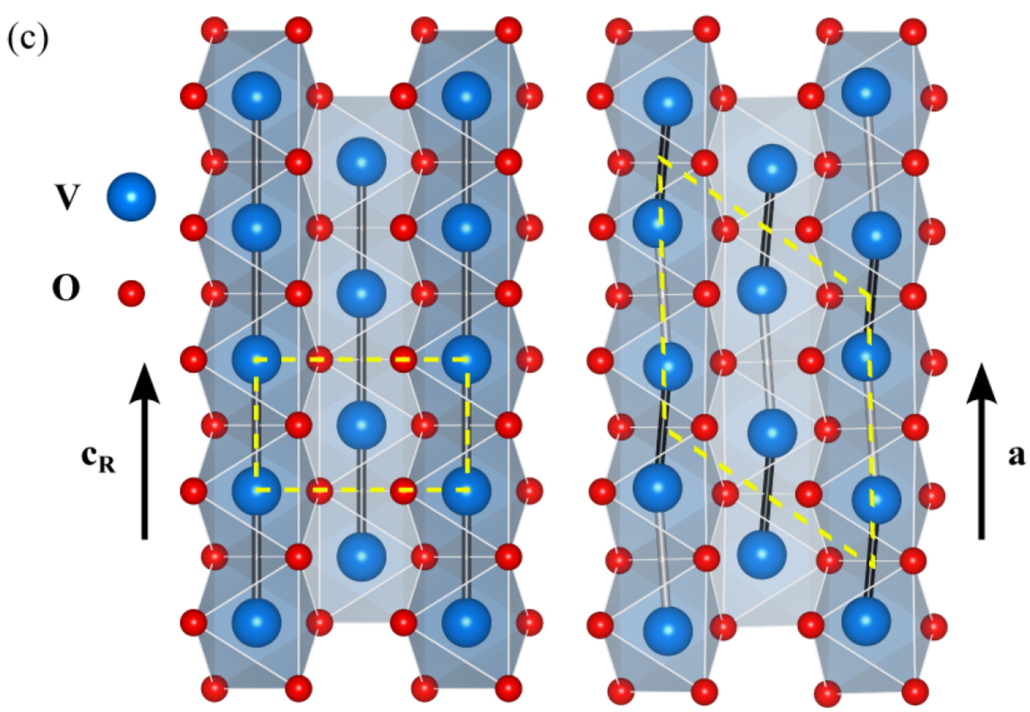

Figure 2.15 VO_2 structural change across the transition [13].

2.2.2 Vanadium Dioxide actuators

Due to the fact that the T_T of VO_2 is so close to room temperature ($\sim$ 68 °C), VO_2 has been increasingly studied as a mechanism for actuation for MEMS devices [21, 22, 23, 24, 25, 26, 27, 15, 17, 28, 29, 1, 16, 30]. The T_T is significantly lower than the temperature used in electrothermal actuators. This translates into much lower power consumption for full actuation of VO_2-based actuators, when compared to actuators that rely on thermal expansion difference mechanisms.

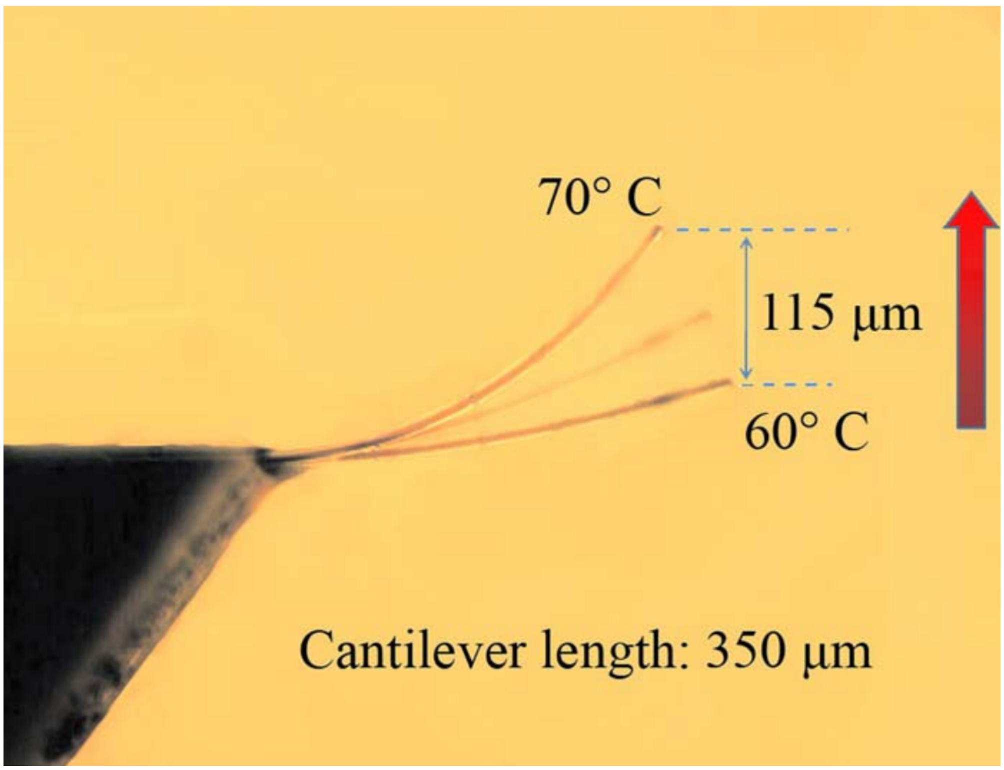

Figure 2.16 First MEMS actuated with VO_2 thin films due to the structural change across the transition [14].

The first publication to use VO_2 as a micro-mechanical actuator was able to measure a maximum curvature change of 2000 m^{-1} on a bimorph cantilever composed of polycrystalline VO_2 film deposited on single crystal Si (SCS), as shown in**Figure** 2.16 [14]. A single-crystal VO_2 (oriented in the c_R axis) microcantilevers coated with chromium (Cr) was studied in [22], where the cantilever was able to have a curvature change across the transition of around 20000 $m^{-1} K^{-1}$ with a curvature rate change of 4000 $m^{-1} K^{-1}$. In a different study a polycrystalline VO_2 deposited by PLD, and coated with Cr was able to have curvature change of around 22000 m^{-1} with a cut-off frequency of around 6 kHz, where the samples are free of fatigue and deterioration [27]. The strain and stress changes generated by the VO_2 films across the transition were up to -0.32% and -510 MPa,respectively. Furthermore, a comparative study was made between different actuation mechanisms comparing the strain energy density of each, where the VO_2 based microactuators had one of the highest strain energy densities with an energy density of 8.1 x 10^5 $J\,m^{-3}$ as shown in **Figure** 2.17 [15].

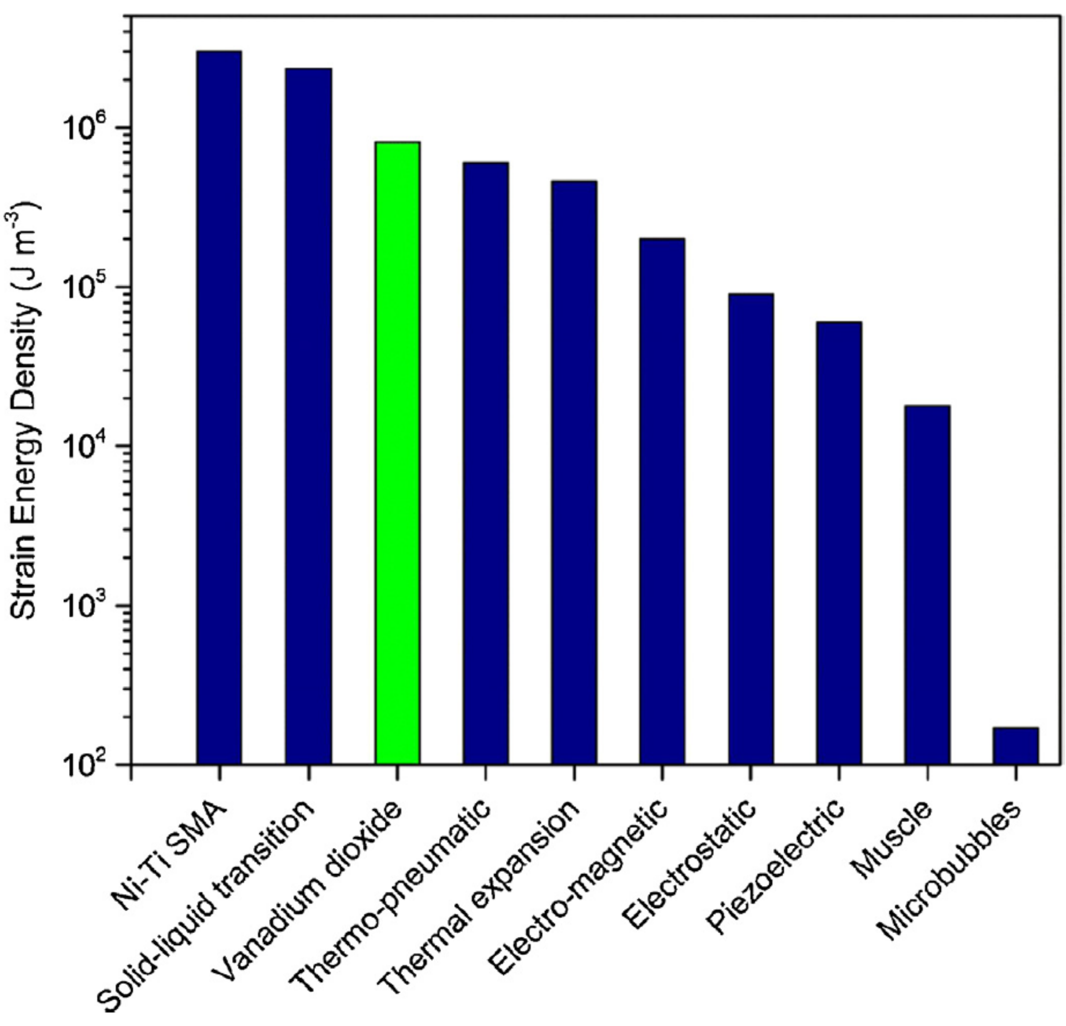

Figure 2.17 Comparison of strain energy density between different actuation mechanics (VO_2 in green) [15].

Since the VO_2 has hysteretic behavior, many studies have focused on the compensation of such phenomenon with different control algorithms. For example, to be able to capture the non-monotonic hysteresis behavior of the VO_2 deflection, a combination of a monotonic Preisach hysteresis operator and a quadratic operator was designed, where the largest tracking error and root-mean-square error were around 10% [28]. More over, an extended generalized Prandtl-Ishlinskii model was designed to model the VO_2 deflection, where a nonlinear memory-less function was introduced improving its modeling capability [116]. Recently, it has been shown that by incorporating singlewall carbon nanotubes (SWNT) in the VO_2 based cantilevers, it can increase the effectiveness to absorb light and reduce the photo-thermal energy required for actuation [16], while increasing the speed and responsivity of the device for photothermal actuation (see **Figure** 2.18).

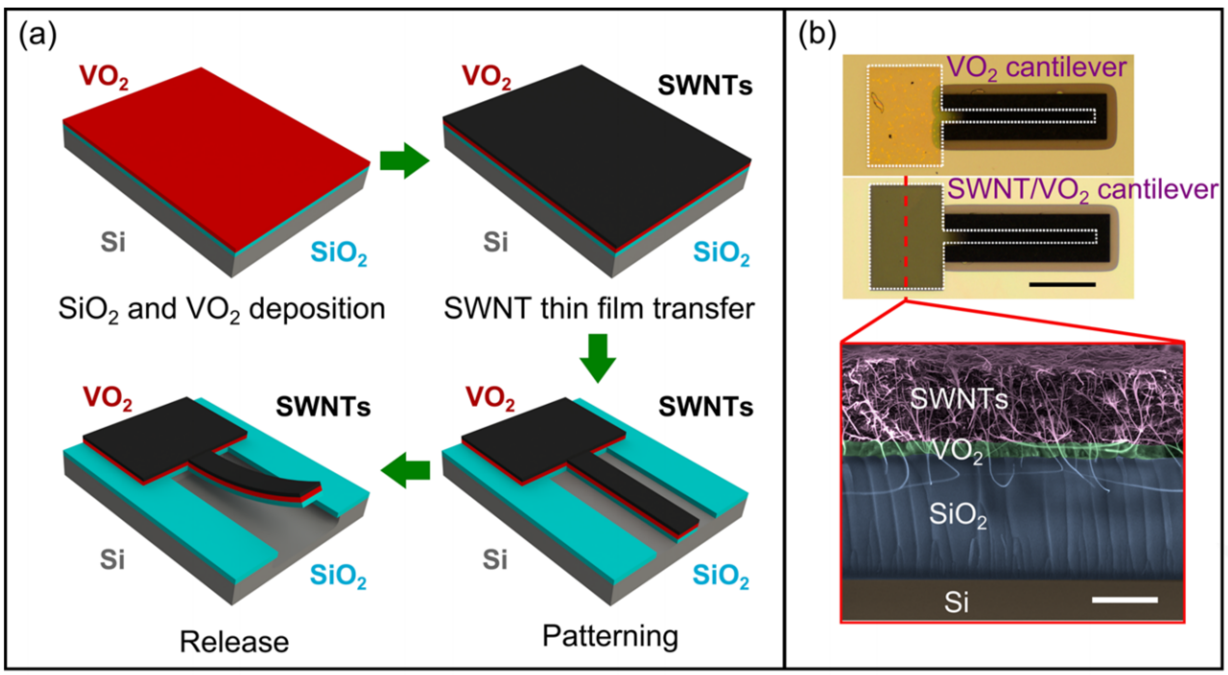

Figure 2.18 Integration of VO_2 with carbon nanotubes to increase the speed and responsivity of the device for photothermal actuation [16].

The VO_2 can also be used to create mechanical memories [17], where multiples mechanical state can be programmed using electrical (shown in **Figure** 2.19) [17] or optical [23] pulses. This is ideal for the development of MEMS mirrors because it will allow for the programing mechanical states of each individual actuator of the MEMS mirror, e.g. programming tilt angles.

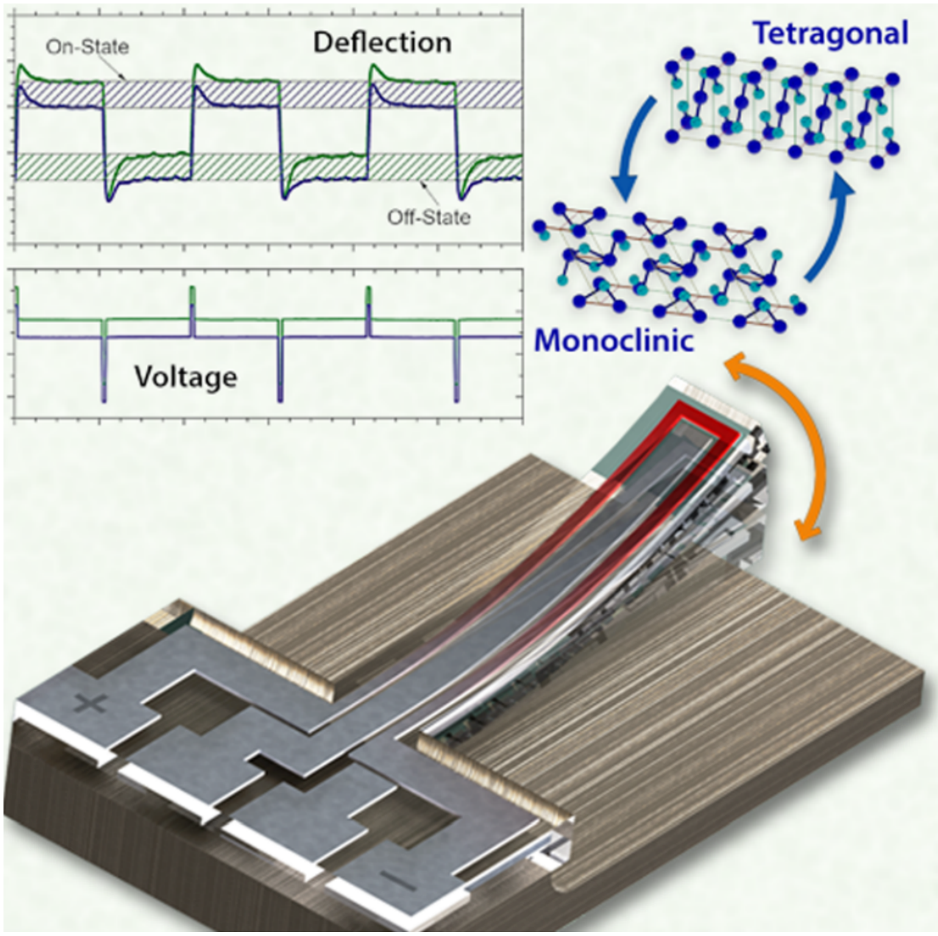

Figure 2.19 VO_2-based MEMS actuator programmed with input pulses [17].

2.3 Summary

In this chapter an extensive study in MEMS mirrors with the most common actuation methods was presented. A TTP design mirror was studied, which it can generate 2D images with the capability to change the elevation of the mirror. The actuation methods such as: electrostatic, electromagnetic, piezoelectric and electrothermal, are discussed with their advantages and disadvantages. Furthermore, VO_2 background was also presented from the transition mechanism (SPT and IMT) to applications as an actuation mechanism in MEMS structure.

CHAPTER 3

DESIGN AND FABRICATION OF VO_2-BASED MEMS MIRROR

The design of the VO_2-based MEMS mirror is based on an electro-thermal TTP MEMS mirror presented in [10, 80, 11], where the electrothermal actuation mechanism is based on the difference in TEC of materials in the bimorph regions. In the present work, the actuation mechanism can still be considered electrothermal in that it uses an electro-thermal process. However, instead of relying on thermal expansion differences between the thin films composing the bimorph regions, mechanical actuation is mainly due to the thermally-induced solid-solid phase transition of a smart material coating (VO_2). Before and after the transition of VO_2, the dominant actuation mechanism is the difference of TEC between the layer, while stress levels induced during the phase-change of VO_2 dominate during the transition. The integration of VO_2 with the MEMS mirror technology decreases the temperature required in the conventional electrothermal mechanism, from 300 °C to 90 °C for full actuation, which lowers the total power consumed by the device. Another advantage of using VO_2 as the actuation mechanism is the large strain energy density generated during the transition, with values higher than conventional actuation mechanisms such as thermal expansion, electrostatic, electromagnetic, and piezoelectric [15]. Furthermore, the intrinsic hysteretic behavior of VO_2 properties (including the mechanical stress that generates deflection in VO_2-based MEMS [14, 1]) across the phase transition has been exploited to design programmable MEMS actuators [17] and resonators [24], and can be used as well to program tilting angles in MEMS mirrors. However, all these advantages come at the cost of added nonlinear effects that make the modeling more complicated than other actuation mechanisms. The proposed device is shown in **Figure** 3.1, and the details of the mirror design are presented in Chapter 2.

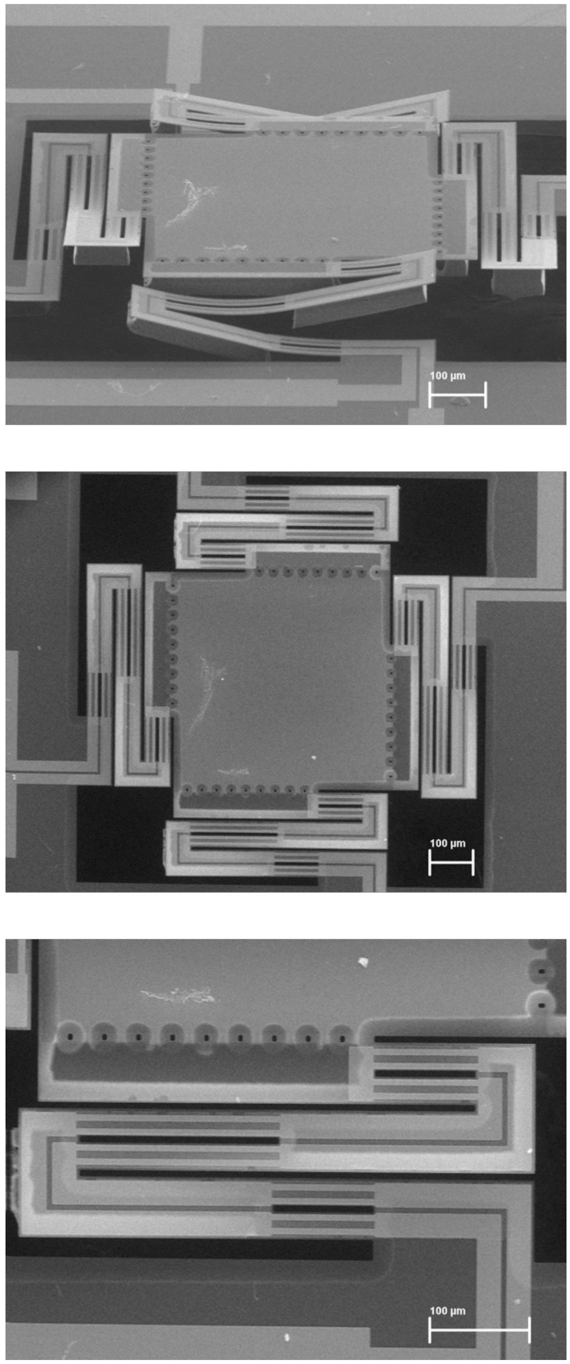

Figure 3.1 SEM image of the first generation VO_2-based MEMS mirror with side view and top view.

3.1 VO_2-based MEMS Mirror design

To be able to integrate VO_2 thin films as the actuation mechanism to the TTP MEMS mirror from [10], a finite element method (FEM) model is created in COMSOL Multiphysics. The FEM simulations are used to see the effect of VO_2 on the structure and optimize the displacement in the structure by varying lengths of the frame (L) and biomorph (l) (see **Figure** 3.2). The material properties used to run the simulation are summarized in Table 3.1 from [1]. To recreate the effect of the VO_2 thin films in the FEM model two simulations are run: the first is used to determine the stress induced by the VO_2 thin film after the transition; and the second simulation is performed to obtain the maximum displacement of the mirror. For the second simulation the stress value obtained from the first simulation is applied as the input to estimate the deflection of the desired mirror with different dimensions.

Table 3.1 Properties used in the FEM simulation for VO_2.

Young's Modulus (GPA)	140
Poissons's Ratio	0.33
Density ($\mathrm{kg\,m^{-3}}$)	4670
Stress (GPa)	1

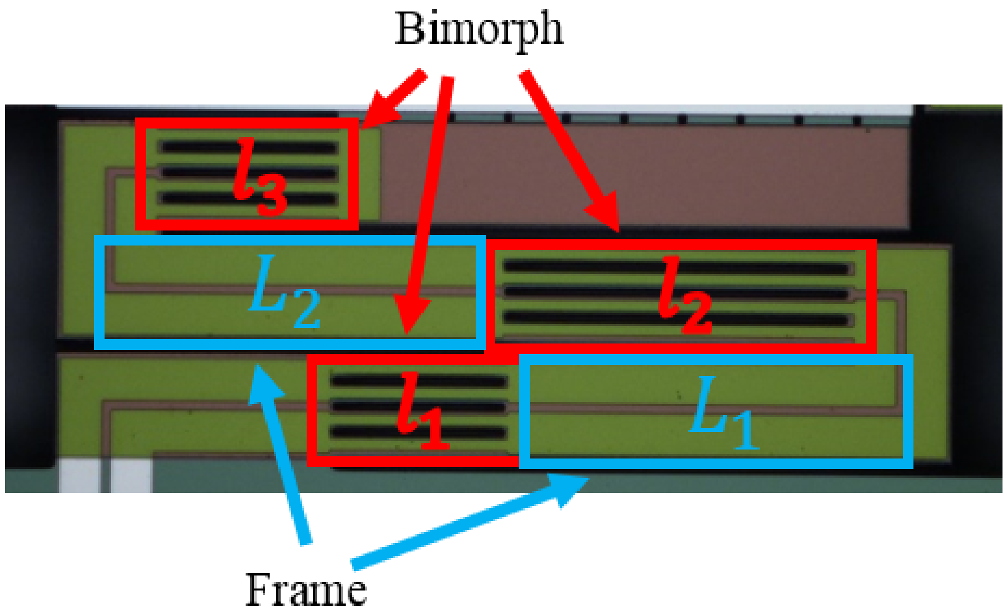

Figure 3.2 Mechanical leg with the frame (blue) and bimorph (red) length.

In the first simulation, experimental results are compared with simulation results to find the stress value after the transition of the VO_2. This stress value is directly related with the maximum displacement of the device. Experimental results are obtain by measuring the deflection of a VO_2 covered cantilever while the VO_2 is actuated by the electrothermal mechanisms described in [30]. The simulation model had same geometry of the experimental cantilever including the VO_2 layer. An external increasing stress is applied in the FEM simulation as the input until the same deflection as the experimental result is reached, resulting in a rough estimation of the stress value after the transition of the VO_2: $\sim 1\,\text{GPa}$. A second simulation is run using the geometry of the desired TTP Mirror and applying the stress value obtained in the first simulation as the input (see **Figure** 3.3). The values of l and L are varied to maximize the displacement in the vertical direction. The resulting values used to design the mirror are shown in Table 3.2.

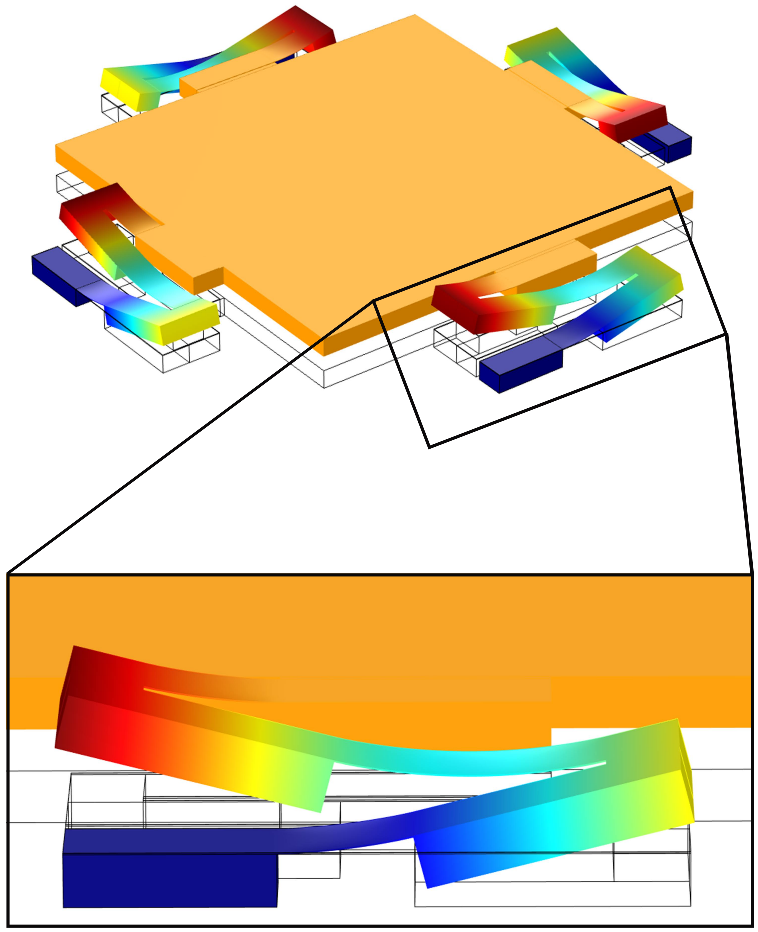

Figure 3.3 FEM Simulation using COMSOL Multiphysics where all the mechanical legs are excited for a piston-like movement.

Table 3.2 FEM simulation results used to fabricate the VO_2-based MEMS mirror

Thickness (µm)	Width (µm)	Bimorph l (µm)	Frame L (µm)	Elevation (µm)
40	42	100	200	94
40	62	150	300	174
40	62	150	500	316
40	62	200	400	315

3.2 VO_2 Deposition

The VO_2 thin films are deposited by PLD. The PLD system schematic is shown in **Figure** 3.4. The sample is mounted on a 2-inch wafer holder, then placed inside the vacuum chamber and aligned in front of the vanadium target. A very low power laser (a typical red laser pointer) is used to align the setup before starting the deposition.

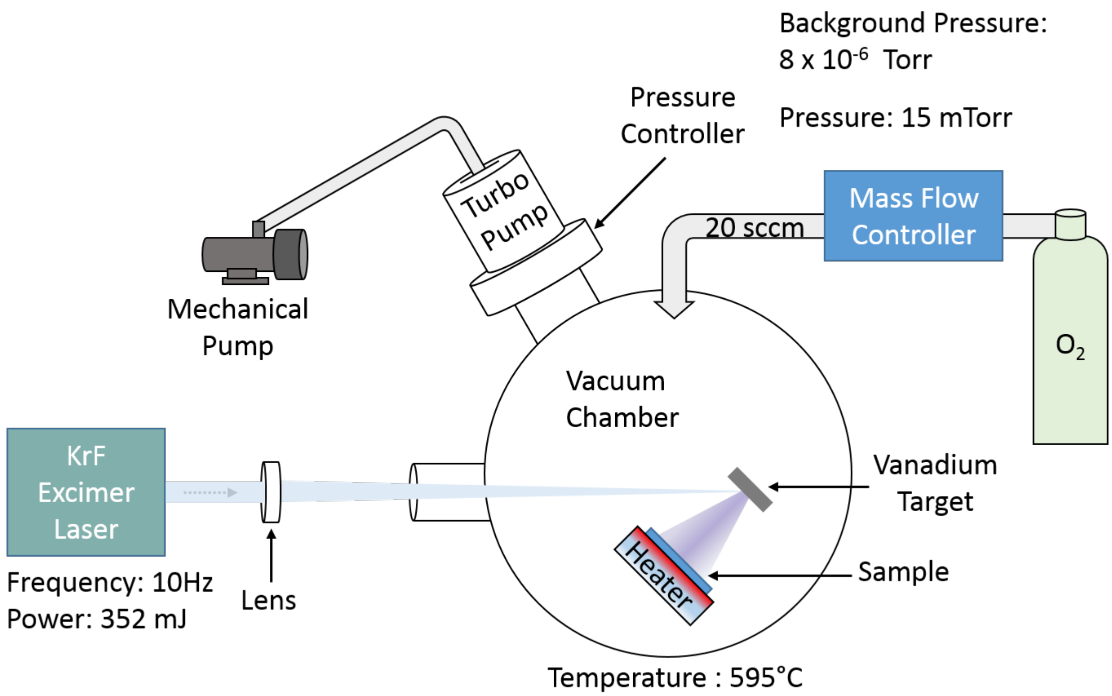

Figure 3.4 PLD schematic with deposition conditions for VO_2 thin films.

To start the deposition process, the vacuum chamber is taken to a background pressure of 8x10^{-6}Torr eliminating any gas impurities that could affect the VO_2 deposition. This is done by turning on the mechanical and then the turbo pump leaving the control valve open. At the same time the gas lines are "cleaned" from gas impurities by closing the gas tanks and opening the control valve of each gas line. To verify the pressure of the chamber, an ion gauge inside the chamber is used. Once the pressure is measured, the gauge is turned off to reduce any damage to it and increase its lifetime. A heater in close proximity to the back of the sample is set to 595 °C, which increased the temperature of the sample to an estimated

470 °C. The estimation are based on calibration curves. Once the temperature is set, the sample is rotated at a constant speed for an even distribution of heat. Rotation could not be performed before the temperature is set, due to the thermal expansion of the metal gears that rotate the sample's holders.

A flow of oxygen of 20 standard cubic centimeters per minute (sccm) is used to create the ambient conditions for the VO_2 deposition. The pressure inside the chamber is regulated using a control valve and maintained at 15 mTorr. A krypton fluoride (krF) excimer laser is operated to provide a train of pulses with frequency of 10 Hz and energy of approximately 350 mJ with a fluence of $\approx$2 J cm^{-2}. The laser ablated a metallic vanadium target inside the chamber for a total of 25 minutes. Upon completion of the deposition time, the laser is turned off and the sample went through a 30 minute annealing process under the same environmental conditions. This annealing step is found to improve the crystallinity of the VO_2 thin films. Afterward, the heater is turned off and once the heater temperature reached 200 °C the vacuum in the chamber is broken. After the sample cooled-down, it is taken out of the chamber.

The electrical properties of the VO_2 thin film can be used to characterize the quality of the VO_2, by measuring the resistance across the phase transition. The resistance of the VO_2 is measured through a temperature sweep from room temperature (30 °C) to 110 °C shown in **Figure** 3.5.

3.3 Fabrication

VO_2 thin films are not compatible with most standard microfabrication processes such as complementary metal-oxide semiconductor (CMOS) process. The CMOS process requires the use of very high temperature for different process such as SiO_2 deposition and ion diffusion. A high processing temperature will affect VO_2 thin films due to either film oxidation (i.e. change in materials stoichiometry) or possible diffusion of atoms from layers in contact

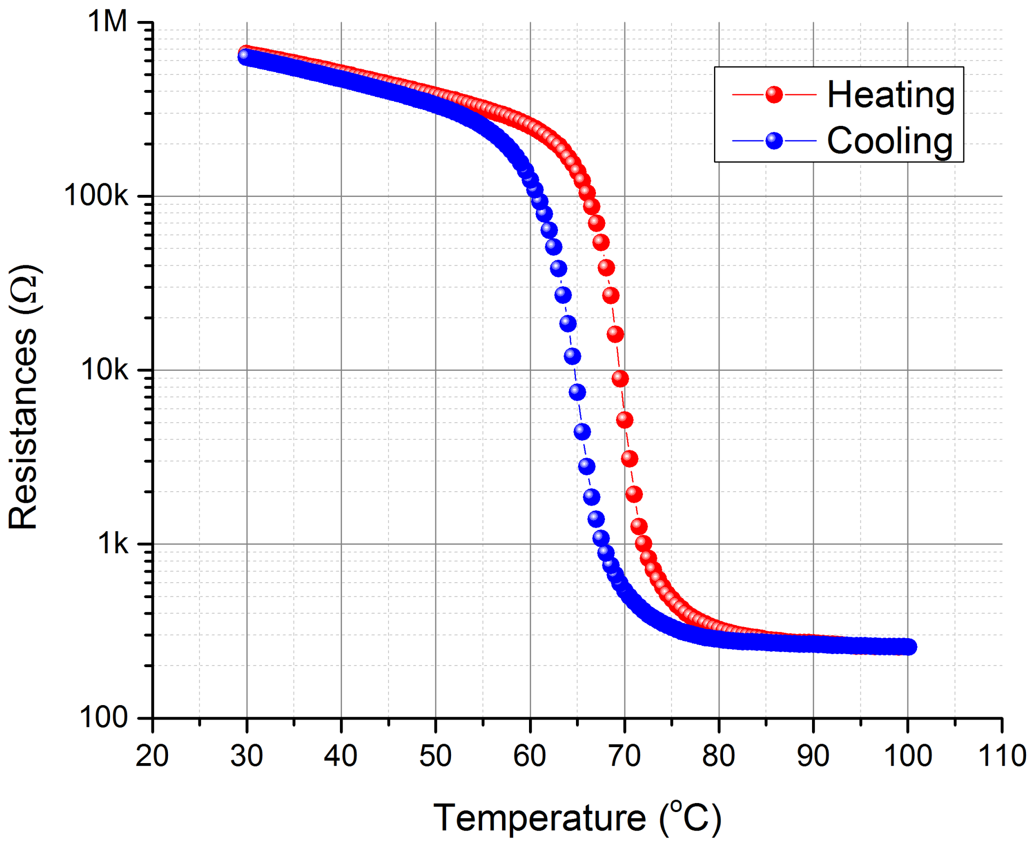

Figure 3.5 Resistance measurement of VO_2 film deposited over SiO_2 on a 2-inch wafer performed right after the VO_2 deposition by PLD.

with VO_2. Furthermore, CMOS devices that include aluminum as interconnect metals are sensitive to high processing temperatures. For example, a typical 0.25 µm CMOS technology cannot exceed temperatures higher than 475 °C for 30 minutes [117]; VO_2 films are deposited at a temperatures of ≈ 470 °C for 25 minutes and immediately followed by a 30 minutes annealing step. The material thin films also degrade rapidly when exposed to most etchants used in standard silicon MEMS processing, including some bases, such as concentrated AZ developers. This is why in the previously reported VO_2-based MEMS actuators, the deposition of the VO_2 film is done as the last step in the fabrication process [15, 30, 17, 24, 1, 29]. Although this approach can be done for relatively simple MEMS devices, it does not represent a viable solution for rather complicated structures, such as MEMS mirrors.

Integrating VO_2 thin films at an early stage of a fabrication process requires the design of a fabrication process that does not involve high temperatures after the VO_2 is deposited; characterization studies of VO_2 thin films in the presence of unavoidable chemicals during lithography (e.g. photoresists and developers); and additional steps that protect the film during necessary wet-etching steps. From preliminary experiments, it is found that after VO_2 thin films are brought to room temperature after the annealing step (VO_2 deposition process as explained in the previous section), they begin to degrade when exposed to temperatures above 275 °C in oxygen environment. It is also found that diluted developer solutions (i.e. 5:1 ; H_2O:Microposit 351) could be used to pattern photoresist layers on VO_2; and that any photoresist from the Microposit S1800 family and MicroChem SF-11 PMGI photoresist (with soft-baking of only 250 °C) will not attack VO_2 thin films.

The chip design included a device that allowed for measuring the resistance of the VO_2 thin film after the fabrication process is complete (see **Figure** 3.7). **Figure** 3.5 shows the resistance drop of the VO_2 thin film right after the film is deposited, and **Figure** 3.6b after the fabrication process is completed. It can be noticed that both resistance drops show the characteristic drop in resistance (at similar temperature regions) and hysteretic behavior for a heating-cooling cycle across the phase transition of the material, which suggests that the composition of the VO_2 and its stoichiometry is not significantly affected during the process. The difference in the resistance values before and after the transition is most likely due to the fact that the resistance drop shown in **Figure** 3.5 is measured on a continuous VO_2 film, whereas **Figure** 3.6 is measured on a patterned VO_2 patch (700 µm wide and 2.55 mm long) through the metal traces on the device (see **Figure** 3.6a).

The fabrication process flow diagram for the VO_2-based MEMS mirror is presented in **Figure** 3.8. A double-sided polished silicon wafer (2 inches in diameter and 300 µm thick) is used as a starting substrate which is needed to improve the backside processes. First, a 1 µm thick of SiO_2 layer is deposited by Plasma Enhanced Chemical Vapor Deposition (PECVD)

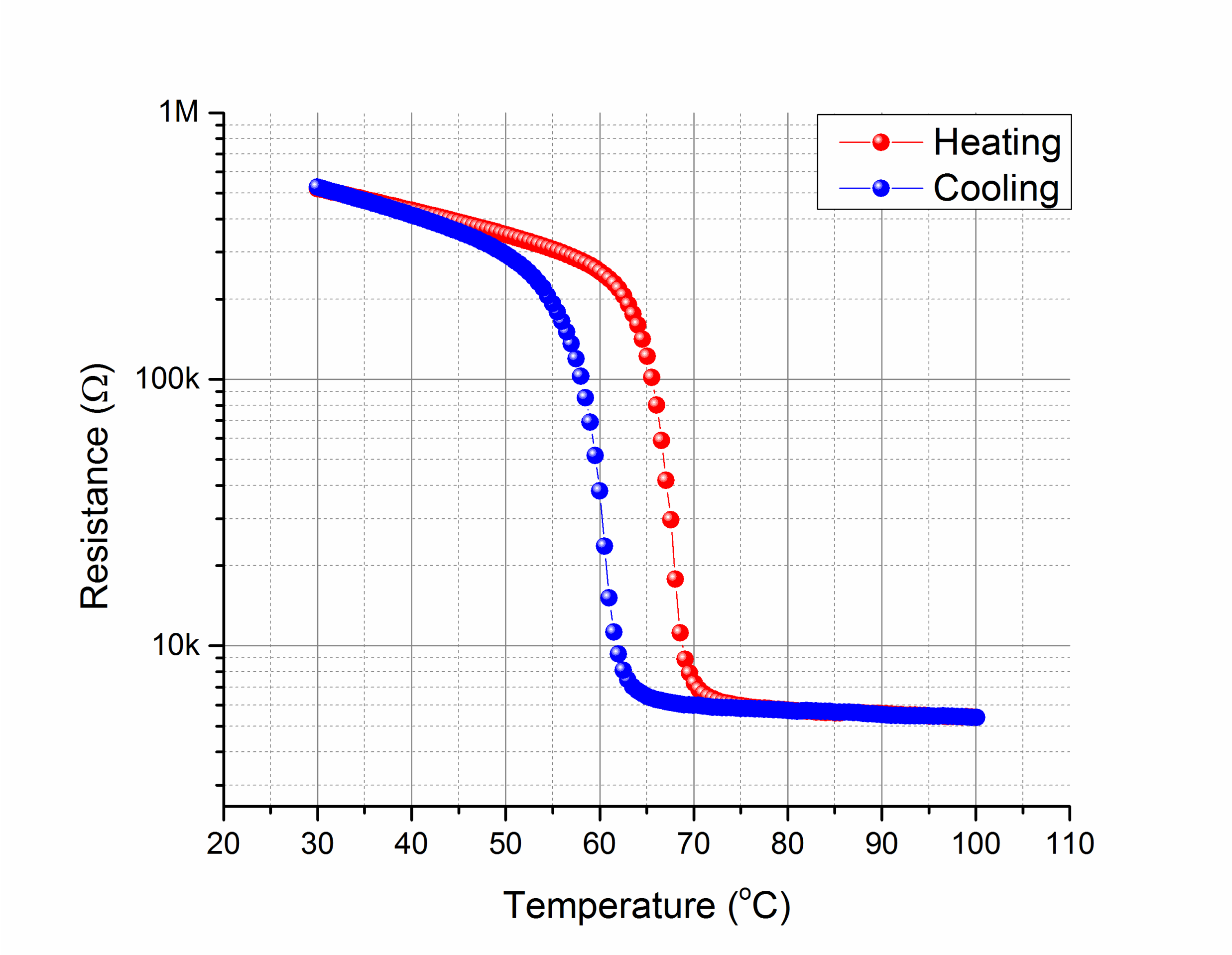

Figure 3.6 Resistance measurement of VO_2 film patch measured at the testing device in the chip after fabrication.

at 300 °C on both sides of the substrate. The SiO_2 layer is needed on one side (front side) for electrical insulation from the substrate and for growing polycrystalline strongly oriented VO_2 with the monoclinic $(011)_M$ planes parallel to the substrate surface [24], this will improve maximum mechanical actuation across the phase transition [17]. The SiO_2 on the back side of the wafer is used as a hard mask for the back side Si wafer etch. The next step is the deposition of the VO_2 film (250 nm thick), which is done by pulsed laser deposition. The VO_2 film is patterned using S1813 as a mask, and Reactive Ion Etching (RIE). Table 3.3 shows the conditions used in the deposition and patterning of the VO_2. A 50 nm SiO_2 layer is then deposited to electrically isolate the patterned VO_2 and the resistive heaters (metal

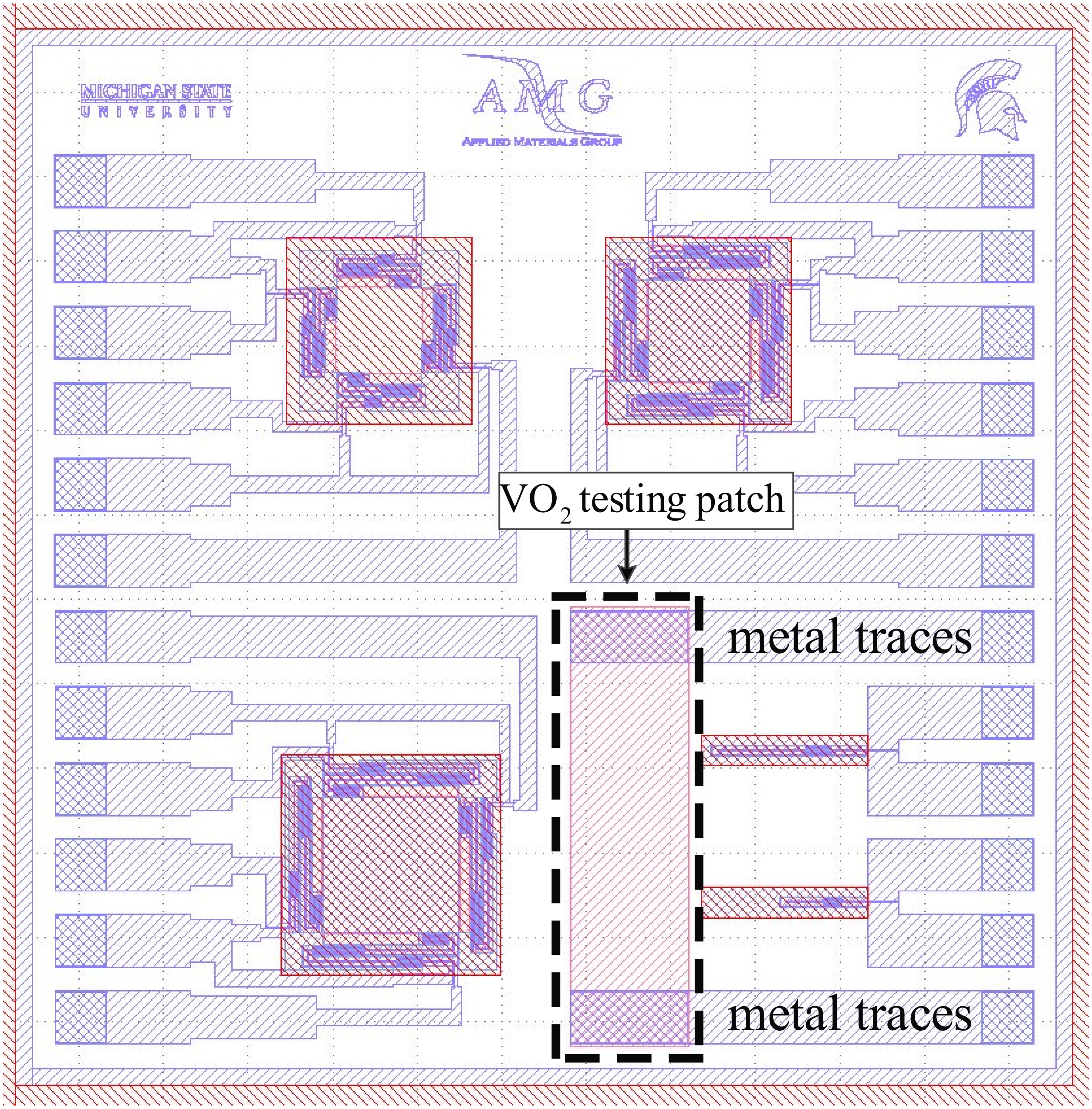

Figure 3.7 Masks layers used for the fabrication of the VO_2-based MEMS mirror with 3 mirror devices and 3 testing devices including a VO_2 patch.

traces). This 50 nm SiO_2 layer is deposited at 250 °C by PECVD, and in two consecutive steps (25 nm each deposition) to reduce voids in the film. It should be mentioned that the width of the VO_2 thin film is 2 µm smaller than the width of the bimorph lines. This is done to guarantee sidewall-protection of the VO_2 film by the SiO_2 layer (see step g of **Figure**

3.8).

Table 3.3 Conditions for RIE and deposition of VO_2

VO_2 RIE Etching		
	He	50
Gas Flow (sccm)	Ar	50
	SF_6	50
Power (W)		350
Pressure (mTorr)		20
VO_2 Deposition Conditions		
Gas Flow (sccm)	O_2	20
Temperature (°C)		470
Distance between sample and target (inches)		2
Pressure (mTorr)		15
Laser		
Energy (mJ)		350
Frequency (Hz)		10
Deposition Time (min)		25

The next step is the deposition and patterning of the metal traces, which is done by using lift-off technique. The metal traces are made of Titanium (Ti)/Platinum (Pt) (20 nm/110 nm), where the Ti layer is used for adhesion purposes. To avoid any problems during the lift-off process, the humidity in the cleanroom need to be lower than 40% (see **Figure** 3.9). The width of the metal traces on the frames of the legs are 24 µm with a separation of 6 µm between the traces. In the bimorph region, the metal lines consisted of two pairs of metal traces separated by 8 µm between the traces and 10 µm between the pair of traces. The width of each metal trace in the bimorph region is 6 µm (see the inset of **Figure** 3.10).

After the metallization, another SiO_2 layer (150 nm) is deposited at 250 °C to insulate the metal traces from the ambient (air); the deposition is divided into three steps of 50 nm each. This 150 nm SiO_2 layer is then patterned using dry etching to expose the metal contact pads and mirror platform. Another SiO_2 etch (1 µm) is performed to expose the silicon wafer for the release of the structure. The backside of SiO_2 is subsequently patterned by RIE (1 µm)

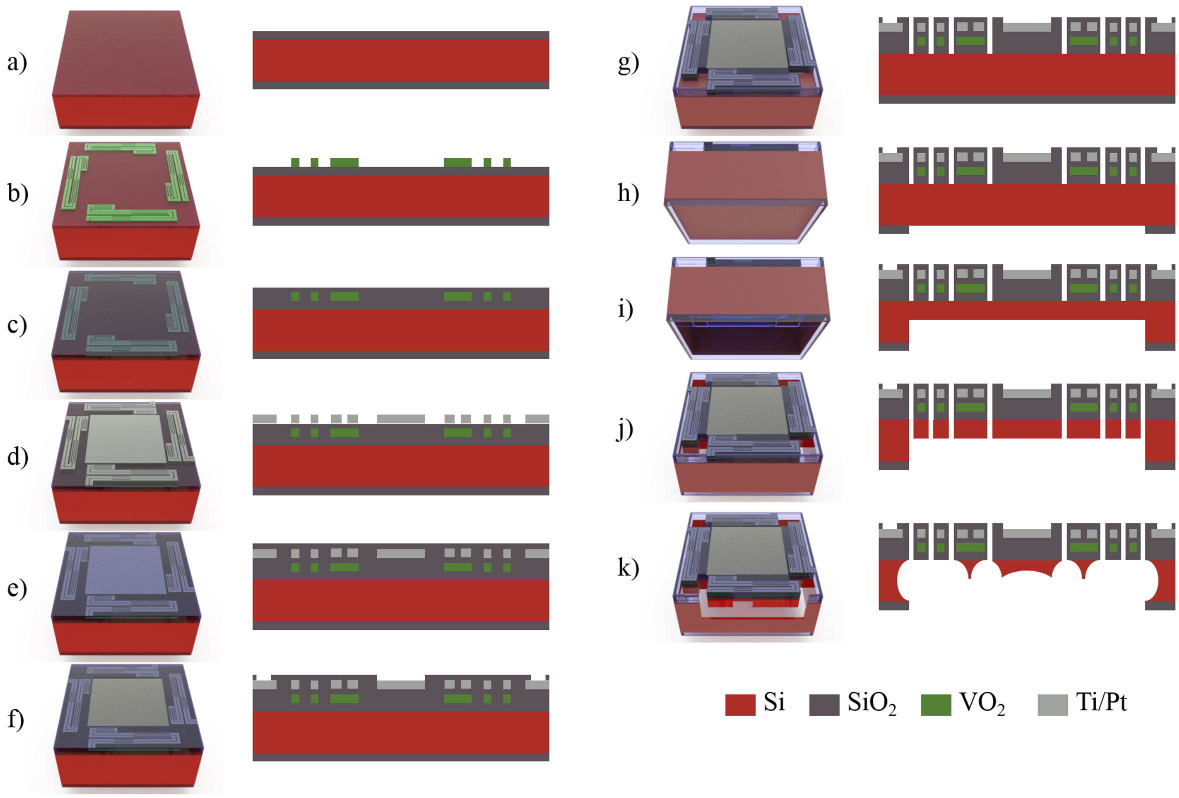

Figure 3.8 Fabrication Process flow. a) PECVD of SiO_2 ,b) VO_2 deposition by PLD, c) PECVD of SiO_2 d) Metallization lift-off Ti/Pt, e) PECVD of SiO_2 ,f) opening to the metal contact pads (SiO_2 etch by RIE), g) SiO_2 etch by RIE, h) backside etch of SiO_2 by RIE, i) backside etch of Si (DRIE), j) SiO_2 etch by RIE, and k) Si isotropic etch (XeF_2).

and used as a hard mask for the Deep Reactive Ion Etch (DRIE) on the silicon. During the backside etch, the top part of the wafer is protected with a double layer of PMGA (polymethylglutarimide) SF11. The PMGA SF11 is removed by submerging the sample in photoresist remover (Microposit Remover 1165) at 90 °C. The backside DRIE is timed to etch 250 µm of the silicon substrate, leaving approximately 50 µm of substrate, which is the thickness of the frame and platform in the final device. A second DRIE step is carried out on the top side of the wafer in order to complete etching through the wafer, leaving the entire MEMS mirror device suspended with a thickness of approximately 50 µm from the silicon substrate. Finally, to remove the 50 µm silicon under the bimorph sections, an isotropic Si etch is used (XeF_2 gas). An experimental study is performed to time the gas etched, where

Figure 3.9 Metallization where the humidity of the cleanroom was higher than 40%.

10 samples are etch with different process times for each one. The results are shown in Table 3.4, where the minimum time needed to remove the Si from beneath the bimorph is 120 s. The isotropic etch is timed to release the bimorph part of the legs, while not affecting

significantly the silicon under the frame and platform sections of the MEMS mirror. The different sections of the final device are labeled in **Figure** 3.10.

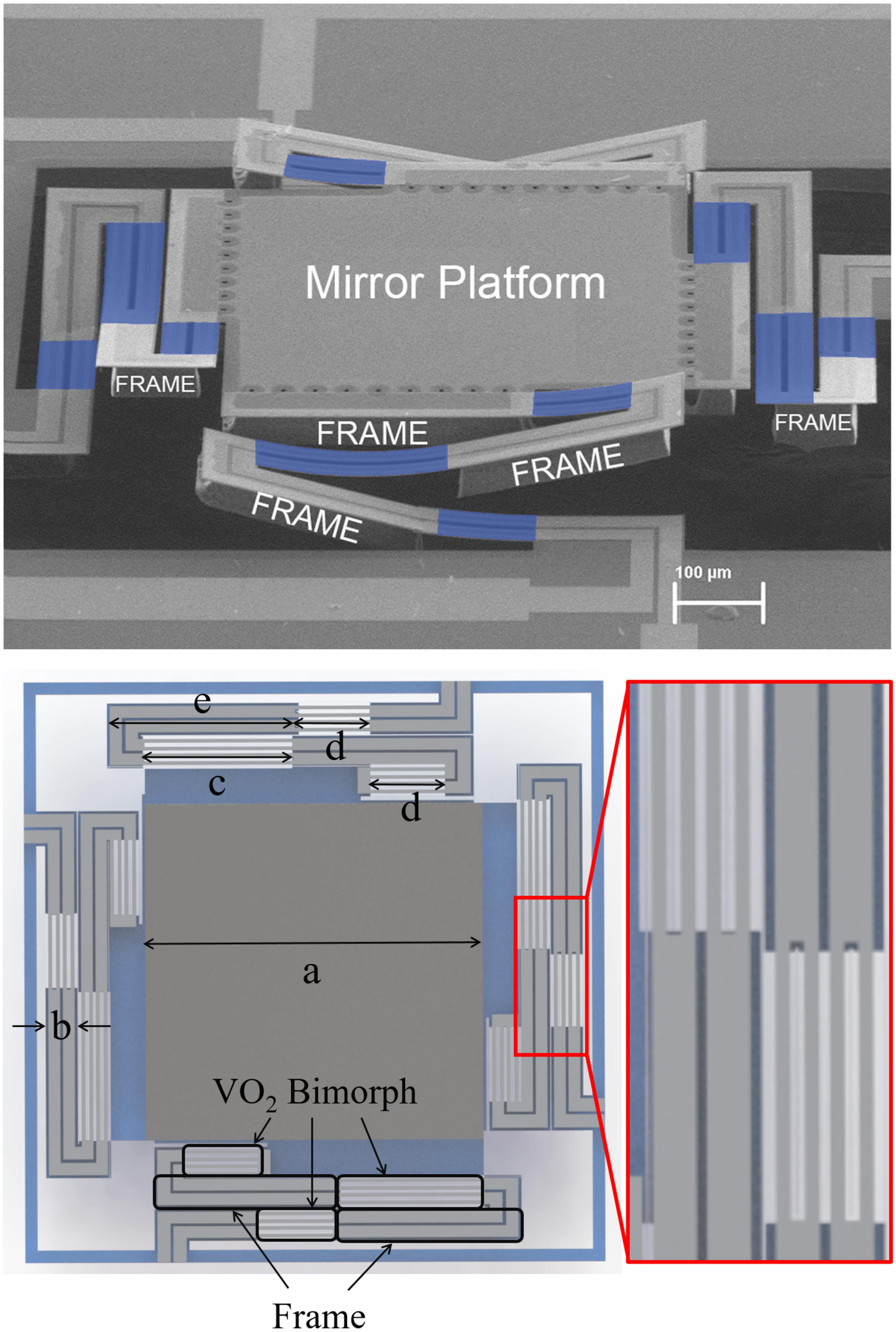

Figure 3.10 (left) SEM image of the first generation VO_2-based MEMS mirror where the bimorph are colored on each leg, (right) Top view of a schematic of the device (gray color represents the metal layer) with the following dimensions : a) 600 µm (platform), b) 62 µm (leg width), c) 300µm (bimorph), d) 150 µm (bimorph) and e) 360 µm (frame).

Table 3.4 Results from the XeF_2 gas etch study.

Sample Number	Time (s)	Bimorph Release?
1	20	no
2	40	no
3	60	no
4	80	no
5	100	no (almost)
6	120	yes
7	140	yes

3.3.1 Optimization of the fabrication process to increase the yield

There are different routes that could be used to fabricated the VO_2-based MEMS mirrors by changing the order of the fabrication steps. To determine the best route of fabrication with the highest yield, two versions of the mirror are fabricated. The first version of the VO_2-base MEMS mirror chip had four mirror devices with the same geometry selected from the simulation that are shown in Table 3.2 and the design is shown in **Figure** 3.11.

Due to various problems in the fabrication process, the first version of the VO_2 based MEMS mirrors did not produce a measurable device. The second version design is improved from the failures of the first design. One example of this are the testing devices added to the chip; where the resistance of the VO_2 film could be measured at any time during the fabrication and the addition of two cantilevers, with a bimoprh and a frame with different lengths, to test the mechanical displacement of the VO_2. The difficulties encountered during the fabrication of the first version of the device are addressed and are presented here. The improvements implemented in the second version resulted in fully functional devices.

On the first version of the VO_2-based MEMS mirrors, a single side polished wafer is used, this created a non-uniform backside DRIE, as shown in **Figure** 3.12. This is resolved by changing the substrate to a double side polished wafer. Both versions shared the same fabrication process steps but in a different order. One example of this is the backside

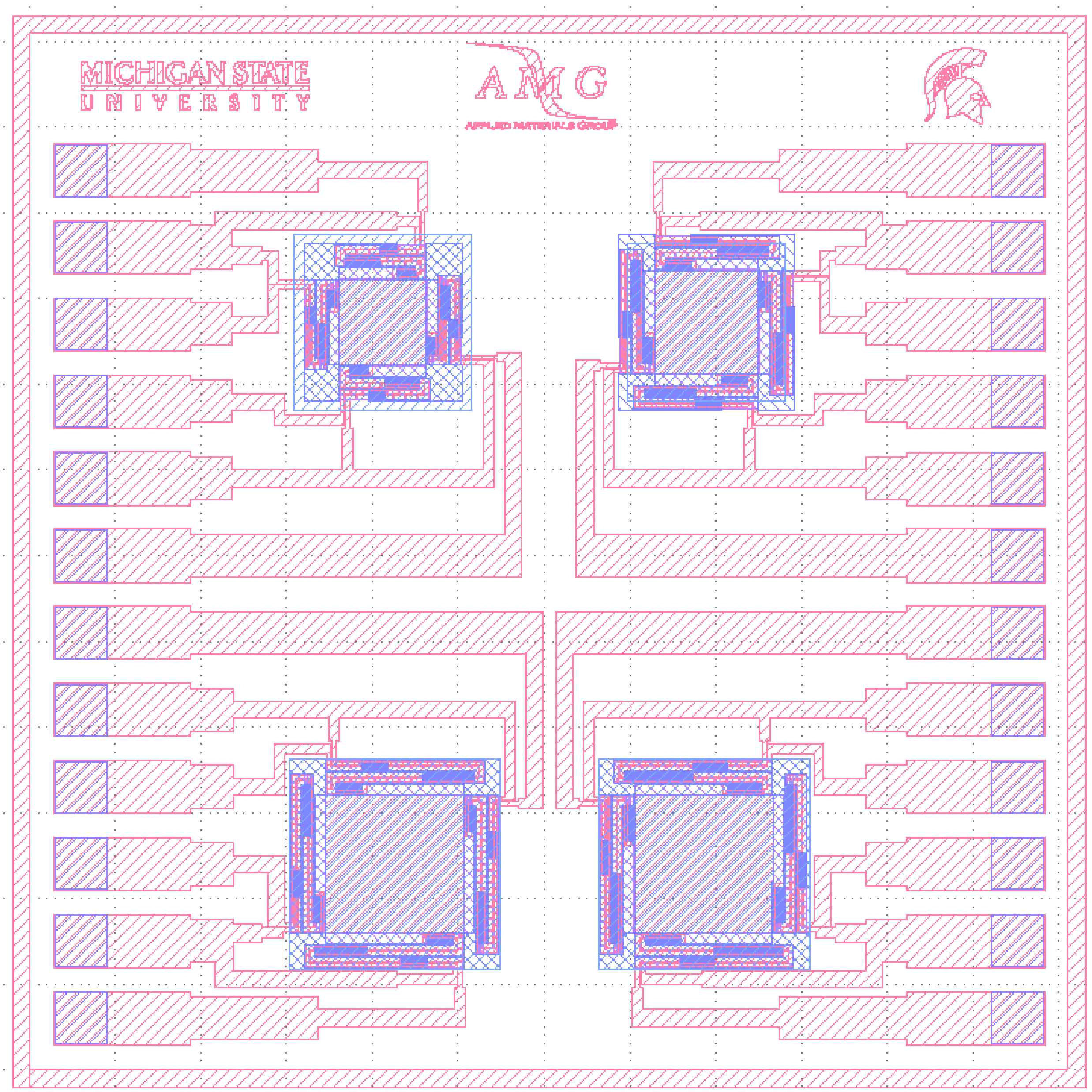

Figure 3.11 Masks layers used for the fabrication of the first version of VO_2-based MEMS mirror with 4 mirror devices.

deposition and patterning, where in the first version it is done after all the top patterning is done. To protect the top side of the wafer during the deposition of the SiO_2 at the backside of the wafer, a dummy wafer is placed on top of the processed wafer with PMGI: SF11. The PMGI is spun and soft baked before the dummy wafer is placed. After the deposition of SiO_2 is performed, the wafers are separated with hot (90 °C) 1165 solvent. Again to

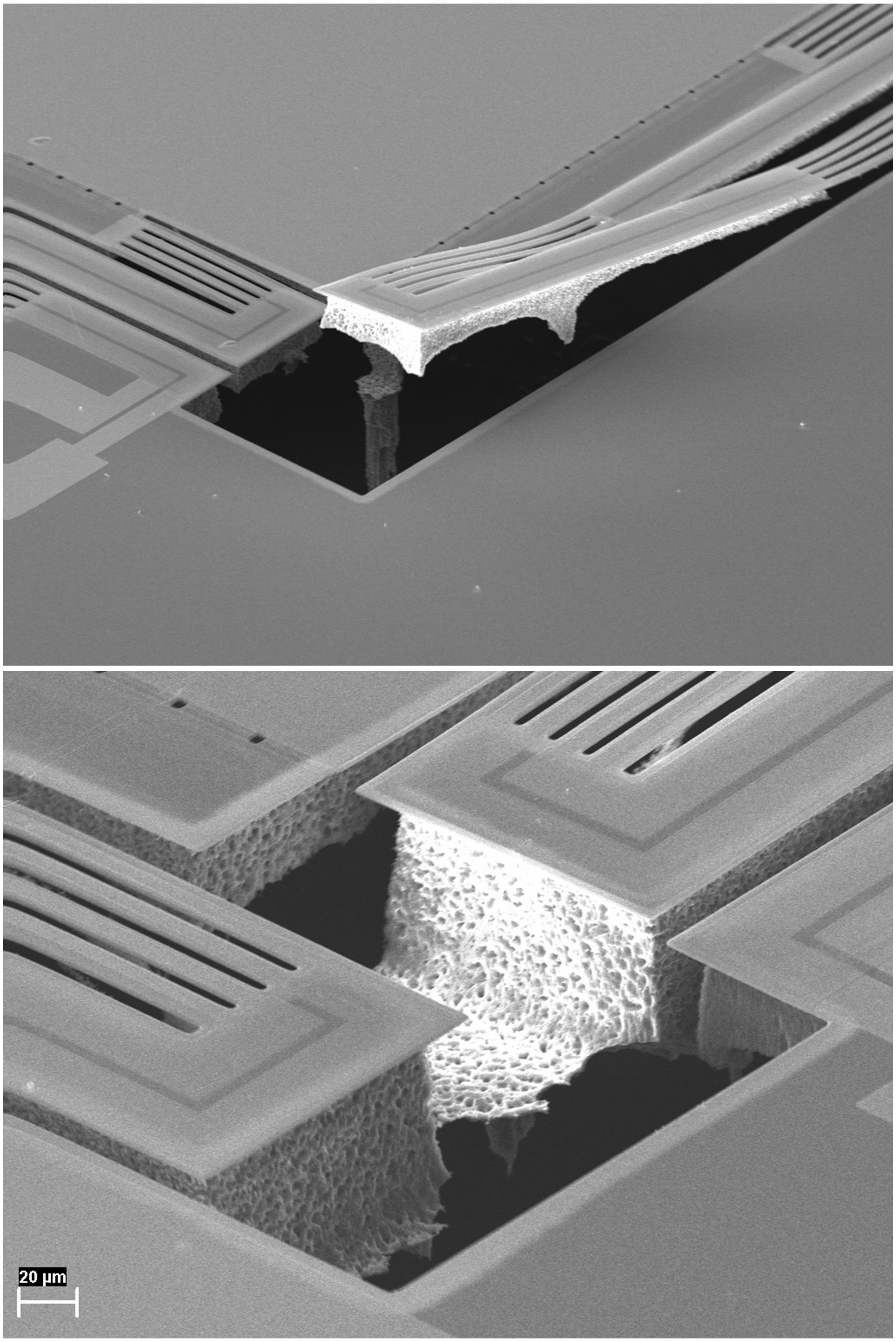

Figure 3.12 Non-uniform Si DRIE etch due to the used of one side polished wafer.

protect the top side of the processed wafer during the patterning of the backside, the top side is coated with PMGI: SF11 and clean with hot 1165 solvent after the SiO_2 etch. For the second device, the SiO_2 of both side of the wafer are deposited at the beginning of the process – this simplified the process.

Similar to previous VO_2-based MEMS devices fabricated in our lab [15, 30, 17, 24, 1, 29], the first version had the metal layer beneath the VO_2 film. The metals layers used on these device needed to sustain the high temperature used in the deposition of VO_2 film, for this reason Ti/Pt are chosen as the metal layer. This made the VO_2 film vulnerable to the DRIE and XeF_2 processes, in which the material would be attacked. An example of this is shown in **Figure** 3.13 where exposed VO_2 is etch after the XeF_2 process. Even though the VO_2 is protected with photoresist and a layer of SiO_2 the VO_2 is etched away. During the topside Si etch by DRIE, the photoresist and the SiO_2 layer are removed from the samples leaving the VO_2 exposed for the XeF_2 etch. The problem is addressed by moving the VO_2 layer beneath the metal and reducing the top side Si etch (by DRIE); since the SiO_2 and the metal layer protected the VO_2 layer from being etched.

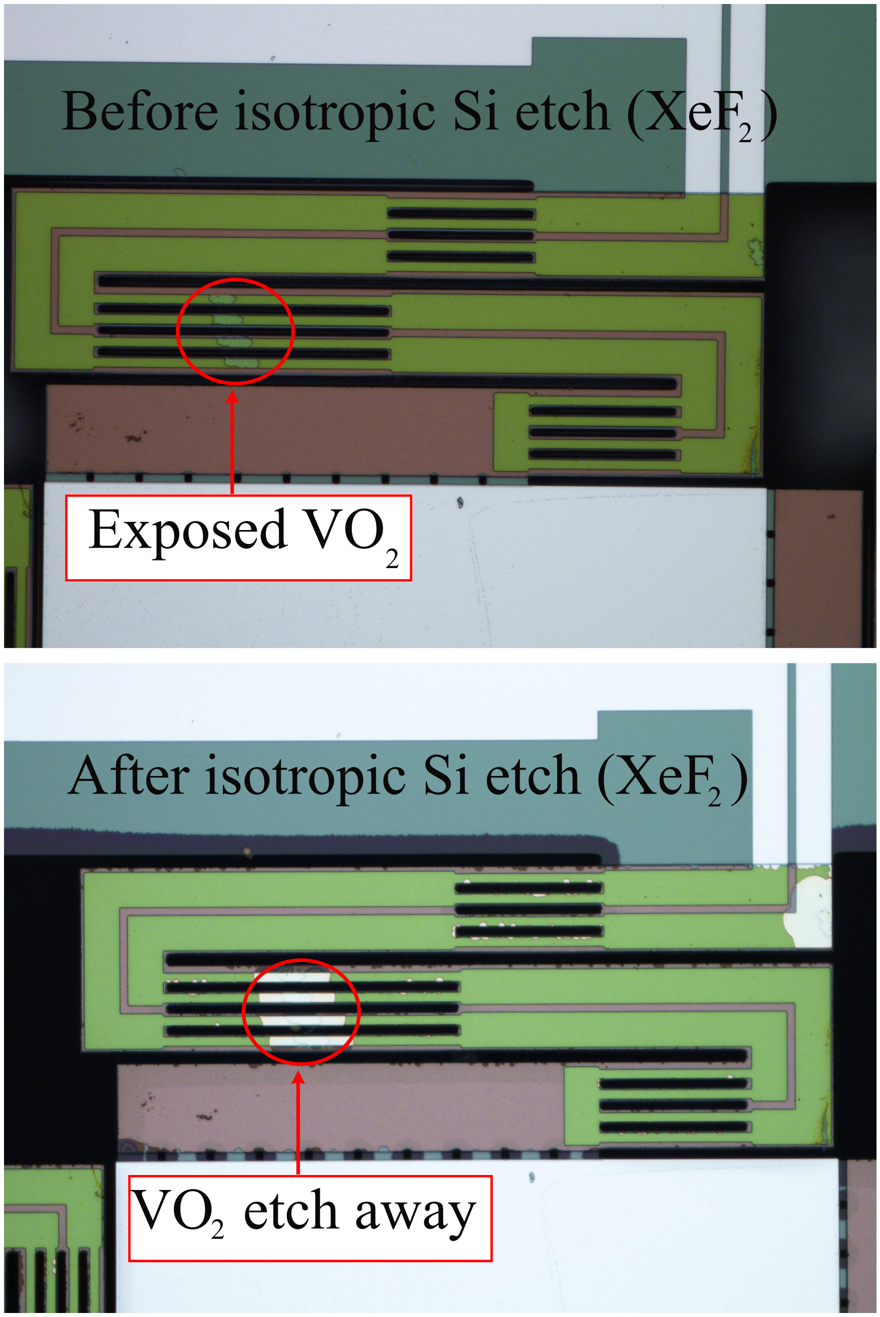

Figure 3.13 Example of VO_2 film being attacked by the isotropic Si etch (the XeF_2 process).

However, this created a different problem, as shown in **Figure** 3.14. The metal layer adhesion is affected and the metal is peeling off from the areas that had VO_2, reducing the final yield of the devices to 12.5%. One possible explanation for this can be the intrinsic stress of the evaporated Ti/Pt metal layer on SiO_2, which could be as high as 340 MPa (compressive stress) [118, 119]. In order to address the issue a second generation of devices are fabricated where the Ti/Pt layer is substituted with evaporated Chromium (Cr) / Gold (Au), which has lower intrinsic stress (250 MPa tensile stress)[120, 121]. This increased the yield to 75%.

Another problem observed during the first version was the “grass effect”, as shown in **Figure** 3.15, that came from the metal of the platform being sputtered during the DRIE top Si etch. The desired thickness of the frame was 50 µm, this was determined by the depth of the backside Si etch. The purpose of the top DRIE was to pattern and release the structure. To ensure the release of the device an over-etch of about 25 µm was performed on the top side, by increasing the time of the etch by 50%. This over-etching caused the sputtering of the metal layer and created the “grass effect”, and affected the VO_2 layer (as previously mentioned). To avoid this in the second version, the frame thickness range from 25 - 50 µm (depending on the thickness of the wafer) and the over-etch was performed on the bottom side of the device, thus eliminating the “grass effect”’.

3.4 Summary

In this chapter, the design and fabrication of the first VO_2-based MEMS mirror is presented, including the challenges and the optimization of the fabrication process. Furthermore, the studies included in this work are key for future device improvements and further development of this MEMS mirror actuation technology. Two generations of the device were successfully fabricated. The first generation used Ti/Pt as the metal layer, with a yield of 12.5%, while the second generation used Cr/Au as the metal layer with an increased yield of 75%.

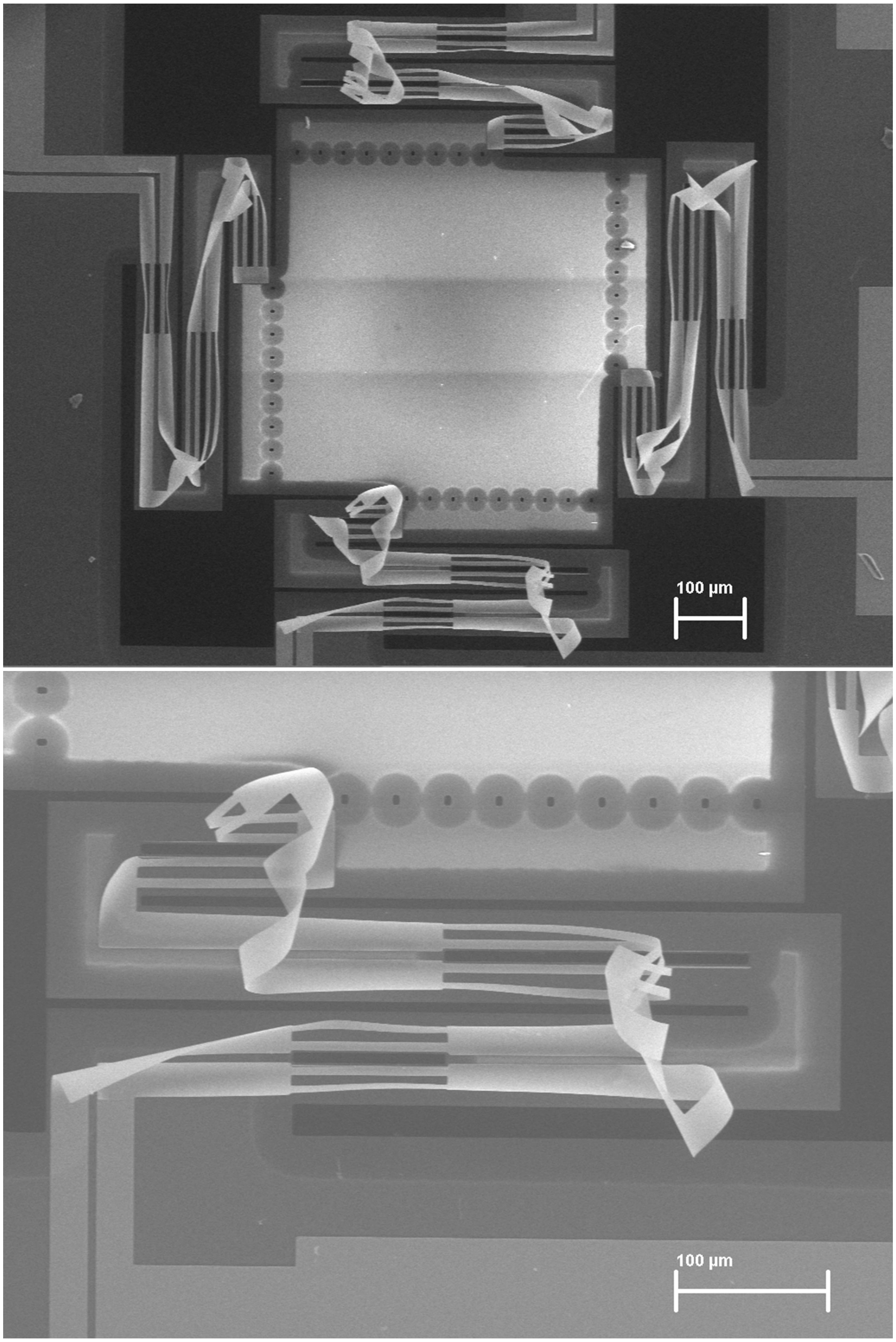

Figure 3.14 Peel-off of the metal (Ti/Pt) layer over the VO_2 layer.

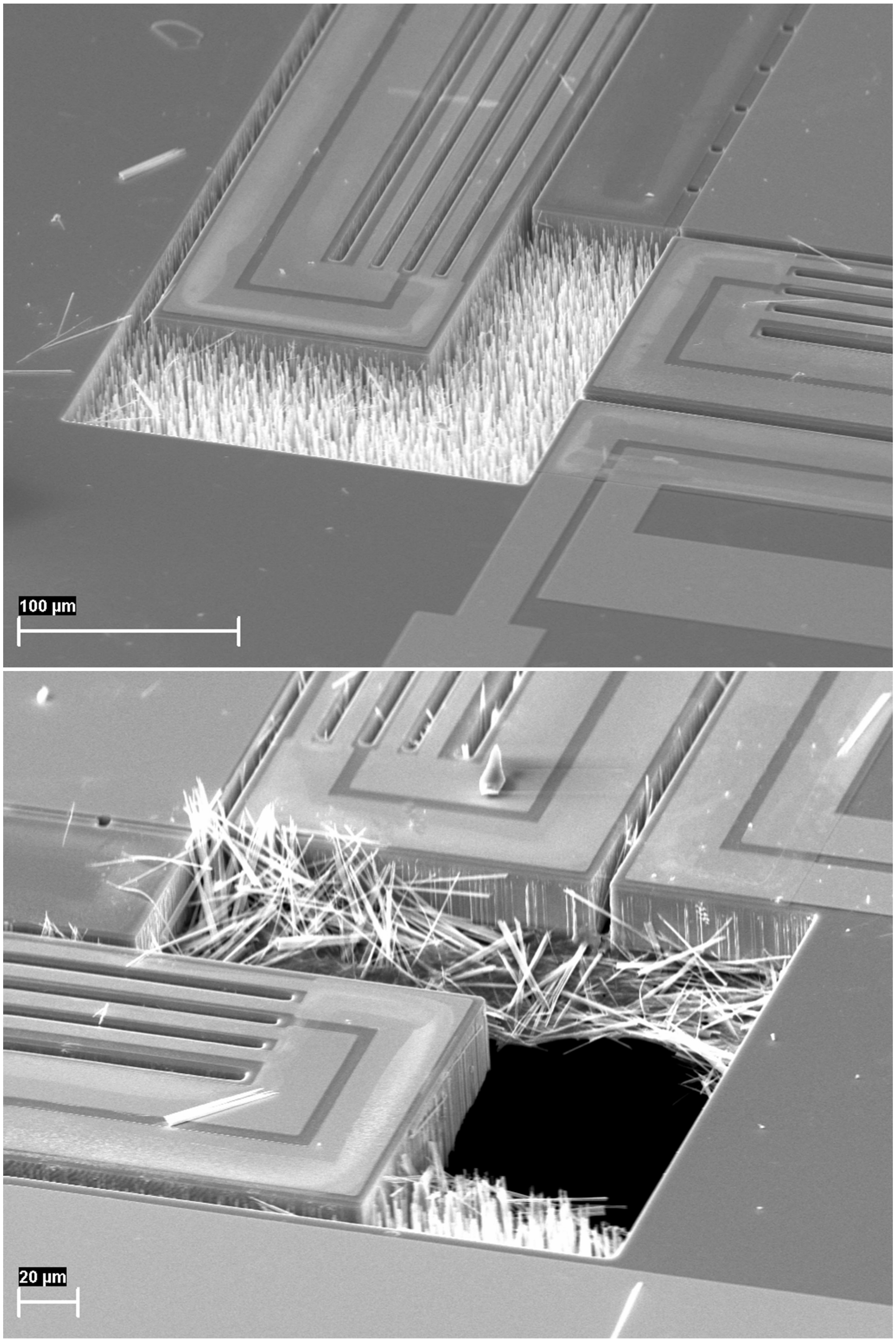

Figure 3.15 “Grass effect” observed after the Si etch of the topside by DRIE.

CHAPTER 4

CHARACTERIZATION OF THE FIRST GENERATION VO_2-BASED MEMS MIRROR

The first generation of VO_2-based MEMS mirror (as shown in **Figure**3.10) is characterized for tilting angle and piston like movement. The tilting angle is generated by individual actuation of the legs and piston like actuation is generated with a synchronous input sine wave to all of the legs. The experimental setup is shown in **Figure** 4.1. A commercially available digital camera (Nikon 1 J1) in combination with an objective lens (10X Mitutoyo Plan Apo Infinity Corrected Long WD Objective lens) is used to grab videos of the mirror's displacement. The camera is used with two different speeds: 29.97 and 1200 frames per second. The resolution of the recorded videos is dependent of the camera speed and the alignment between the optical lens, MEMS mirror and camera, with a resolution of 0.7574 µm/pixel for a speed of 29.97 frame/second and 5 µm/pixel for a speed of 1200 frames per second. Tracker Video Analysis and Modeling software tool (Version 4.91, Douglas Brown, physlet.org/tracker) is used to analyze these images and videos.

The device chip is wired bonded to a rectangular IC package and soldered to a PCB board creating the electrical connections between the metal contacts and the data acquisition system (DAQ). All the input and output is generated and read by a DAQ from National Instrument controlled through Labview. To be able to generate the current needed for each actuator, the electrical connection of each actuator is connected to a common collector circuit with the output of the DAQ being connected to the base of the BJT NPN transistor (2n3904), as shown in **Figure** 4.2. A resistance (R1) in series between the transistor and the actuator is used to limit the maximum current that passes through each actuator, thus eliminating any possible damage to the device.

In order to automate the displacement measurements, an infra-red (IR) laser (λ = 985

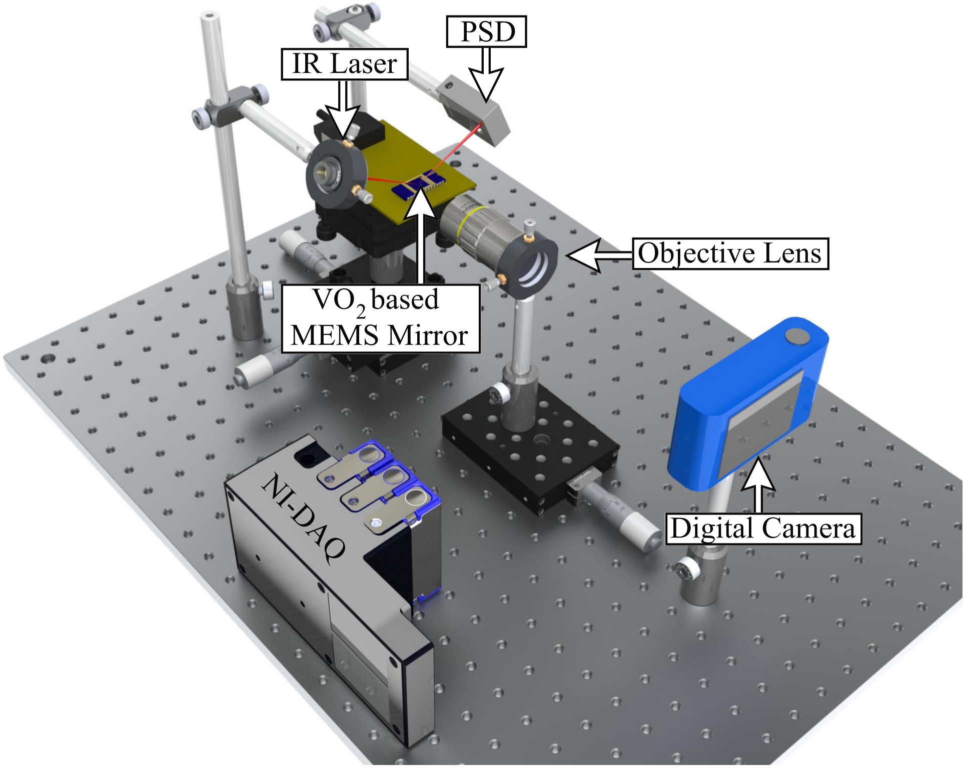

Figure 4.1 Measurement setup used for characterization of VO_2 MEMS mirror [18].

nm) and a 1-D position sensing detector (PSD) are used to track the movement of the MEMS mirror platform due to the actuation of each leg (see **Figure** 4.1). The PSD sensor had a voltage output which is connected to the DAQ. The laser is aligned and focused at the center of the platform of the mirror using a top view camera and had a power of 2.9 mW. To relate the output voltage to a real physical value, a video recording of the experimental actuation is analyzed using the Tracker Software. Afterward, both measurements are compared with the maximum and minimum displacements of the platform; i.e., Tracker software is used to calibrate the displacements measured by the PSD.

4.1 Results and Discussion

Different experiments are performed to characterize the performance of the presented MEMS mirror. The characterization included individual displacement of each leg (mirror tilting

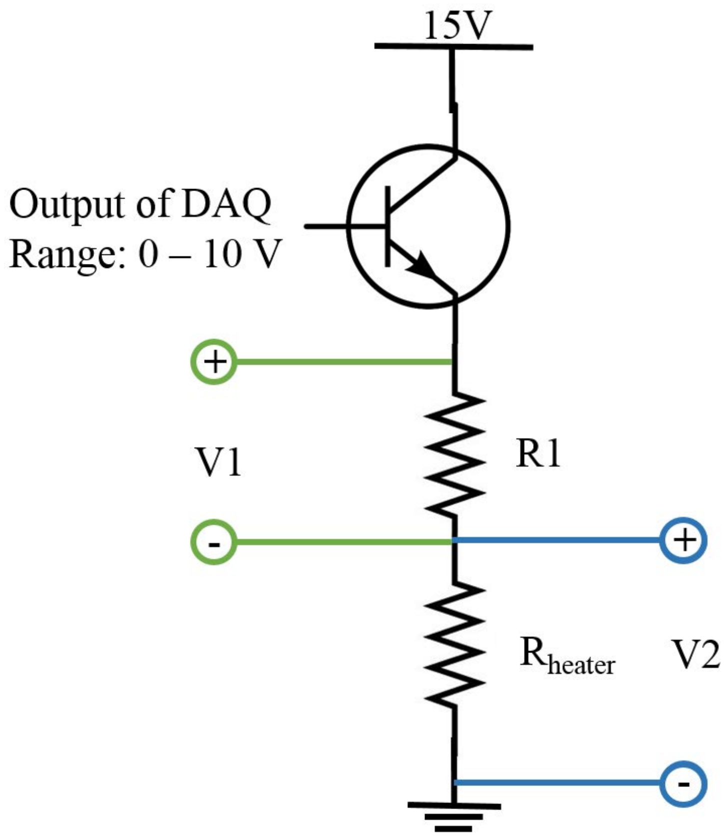

Figure 4.2 Circuit used to control the current across of an actuator. V1 and V2 are voltage measured with the DAQ, where V1 is used to calculated the current. R1 is a known resistance used to limit the maximum current that goes through the electrical connection of the actuator and R_{heater} is the resistance measure between the actuator and the metal traces.

angle), piston motion displacement and power consumption measurement.

4.1.1 Displacement and tilting angle measurements

First, the displacement of the platform generated by the actuation of individual legs is measured using the IR laser and PSD (with calibration from Tracker software), with a voltage input to the resistive heaters that followed a sine wave: $V = 0.72 \sin(2\pi ft) + 0.85$, where f is frequency (1 Hz), t is time, and 0.85 V represents an added offset voltage. The input signal is chosen to have the complete hysteresis loop with minimal distortion due to the frequency [29]. **Figure** 4.3 shows the displacement of the platform sides due to their corresponding leg. Every leg shows that the bending is in opposite directions for regions outside and inside the phase transition and this behavior is consistent with that of previously reported VO_2-based MEMS actuators. Furthermore, the hysteresis observed across the phase transition is not expected in systems where the dominant actuation mechanism is the difference in TEC of two materials.

The tilting angle is calculated from the measurement of the displacement of each platform side for the actuation of the corresponding leg, using the following equation:

$$\theta = \sin^{-1} \frac{(h_1 - h_2)}{d}, \tag{4.1}$$

where h_1 is the displacement of the platform side, h_2 is the displacement at the opposite side of the actuating leg (assumed to be 0 µm for no actuation), and d is the separation distance between h_1 and h_2, in this case the length of the platform mirror (600 µm) (see **Figure** 3.10).

Another observation from **Figure** 4.3 is that, although all the legs show similar displacement curves, their maximum/minimum displacement values are not the same, and they do not occur at the same voltage input. There are multiple possible reasons for this, but it has been verified that the most likely cause is related to the high sensitivity of VO_2-based actuators and the different temperature distributions in the heaters of each leg for the same current input. The hysteresis in the VO_2 film used for the present VO_2-based MEMS mirror spans only about 10 °C (see **Figure** 3.6). Using the maximum vertical displacement measured, sensitivity can be estimated to be approximately $7\,\mu m\,°C^{-1}$, or $169.95\,\mu m\,V^{-1}$. Given this sensitivity (which is significantly higher than that obtained with bimorph actuation [11]), any small difference between the structures of each leg (e.g., differences in structural thermal mass -due to underetching during release, or resistance of heaters -due to misalignment or lift-off process-) will result in different deflections for each leg for the same voltage input. To verify this hypothesis, the resistance of each heater is measured as a function of voltage. The result is shown in **Figure** 4.4, which shows the differences in resistance change with the same voltage input for the four heaters in each leg. The offset values between resistances are due to the different length of the metal traces between the legs. As the temperature increases

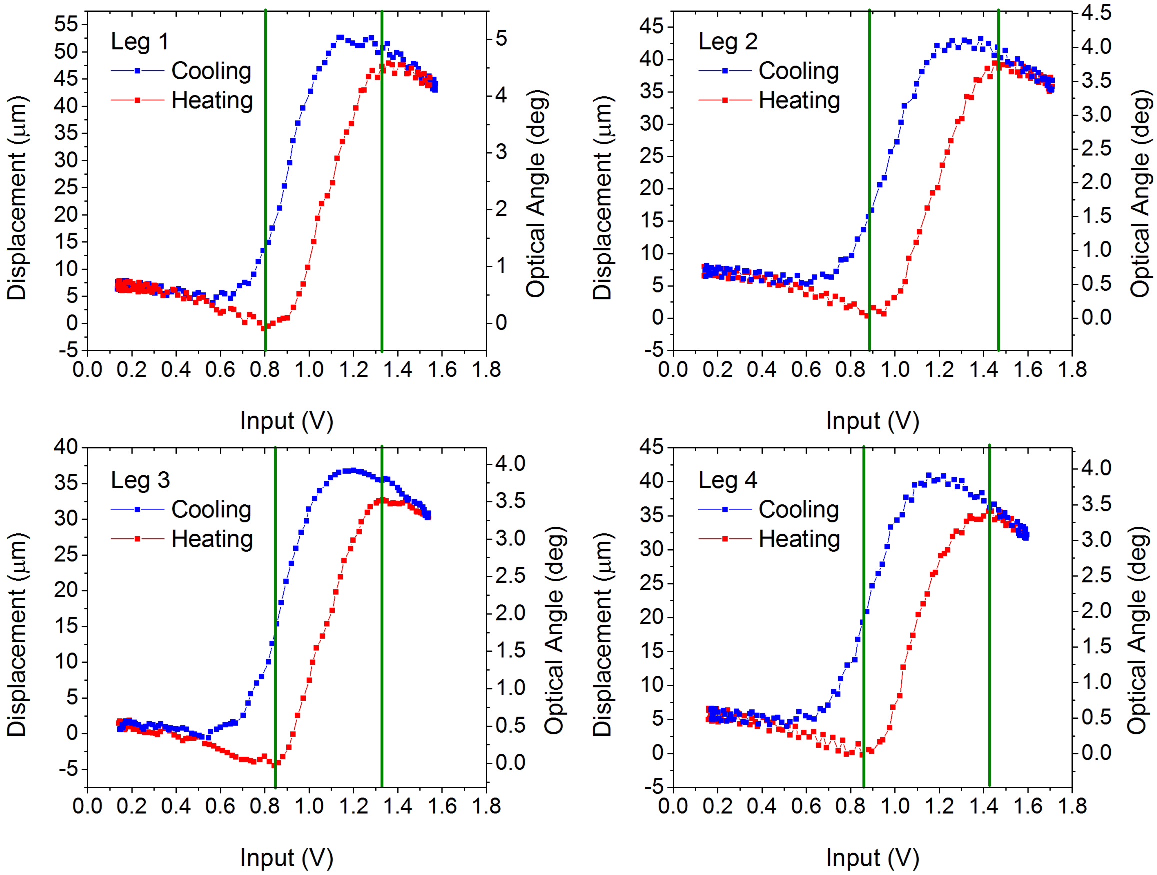

Figure 4.3 Displacement for each individual mirror leg. Transition region of VO_2 occurs between the vertical lines [18].

in the legs, the change in resistance between the legs should have the same behavior, given that the heating component of the legs are the same as shown in **Figure** 3.7. It should be noted that Leg 4 does not follow the same behavior as the other legs (see **Figure** 4.4). This could mean that the metallization for this leg is of poor quality. During the fabrication of the device, delamination of the metal traces is observed on these devices (see Chapter 3). This observation suggests that the responses of each leg could be synchronized by improving the quality of the metallization on the legs and ensuring the same current goes through all the legs.

To measure the total displacement of the VO_2-based MEMS mirror, all the mirror legs are

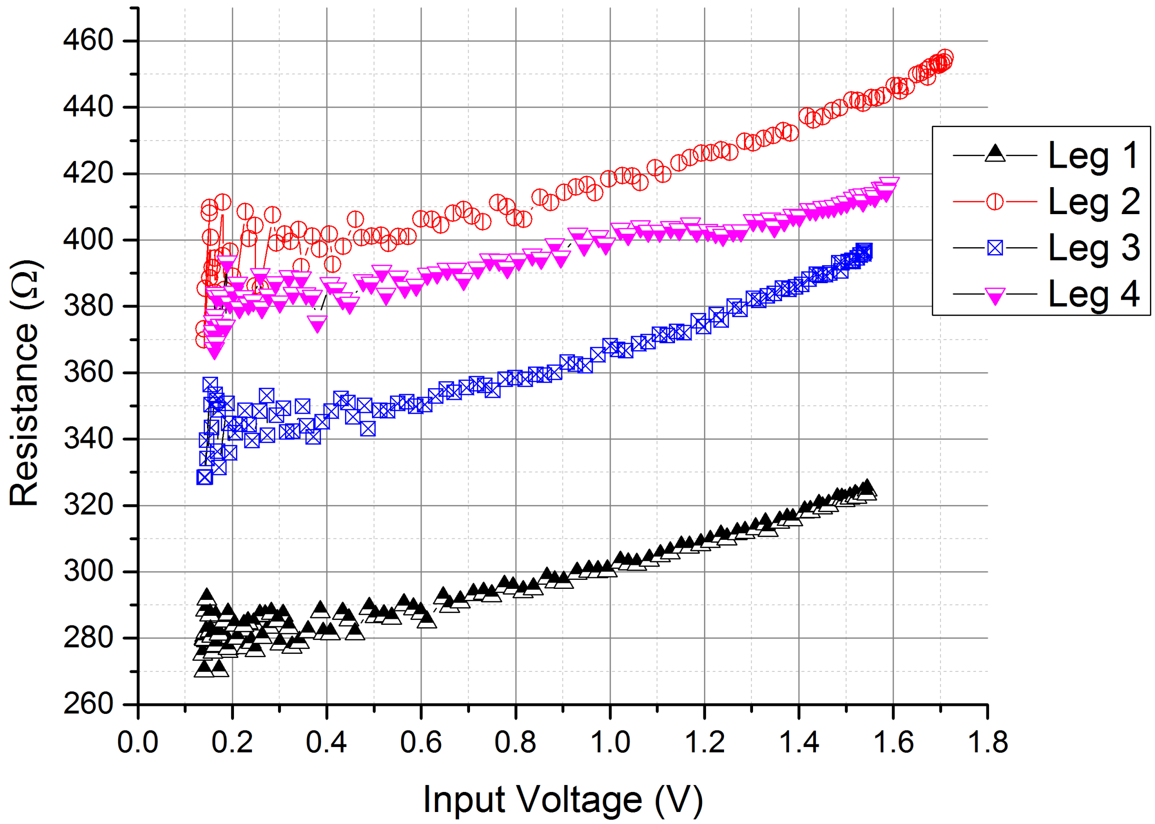

Figure 4.4 Resistance of each heater traces as a function of voltage [18].

actuated at the same time, creating a piston movement. Just like for the actuation of individual legs, the input for the piston movement is an oscillating voltage, $V = 0.83\sin(2\pi ft)+0.9$. This movement could not be measured using the 1-D PSD, since the reflected beam from the mirror platform did not follow a straight line; a voltage input value did not generate the same deflection in all mirror legs. Thus, the measurements for the piston movement had to be made using only the digital camera and the tracking software, and could not be automated. **Figure** 4.5 shows the vertical deflection of the mirror under piston movement. The largest vertical displacement is 75 µm, and it occurs when the voltage input to each leg is 1.1 V and within a change of input voltage of only 0.38 V. The correspondence between the voltage input and the mirror displacement is done by pairing the maximum of the voltage sine wave with the minimum in the mirror displacement after the phase transition is complete. This point occurs at approximately 1.25 s.

The difference in the input voltage needed to reach the maximum deflection between the individual (1.3-1.4V) and piston (1.1V) actuation can be caused by the difference in the extrinsic stress in the VO_2 thin films during actuation between both experiments. It is known that extrinsic stress can change the transition temperature of VO_2 [95, 96, 97]. During individual actuation, the lack of displacement from the other legs will restrain the movement of the actuated leg. Thus, when only one leg is actuated the net effect is an added stress to the VO_2 thin film. This added stress is lower when all the legs are actuated; notice that the larger maximum deflection measured for the piston movement (75 µm, shown in **Figure** 4.5) is larger than that obtained for individual actuation (ranging from 37 to 47 µm, shown in **Figure** 4.3). The non-monotonic behavior of each individual leg is reflected in the displacement curve for the piston actuation. Although the mirror platform is not expected to remain parallel during actuation since each leg does not show the same deflection for a given voltage input, this difference is not noticeable in the obtained videos.

4.1.2 Power Consumption

The maximum power consumption of the present VO_2-based device is calculated for the actuation of each individual leg across the entire phase transition, using the applied voltages shown in **Figure** 4.3, and the heater resistances shown in **Figure** 4.4. The average maximum power consumption of between the individual leg is 6.53 mW. The maximum power consumption for each leg is also estimated for actuation due to the phase transition only (i.e. from lowest deflection to largest deflections in the heating curves). The results are shown in Table 4.1, which also include the power consumption for piston--like actuation (i.e. actuation of the 4 MEMS mirror actuators).

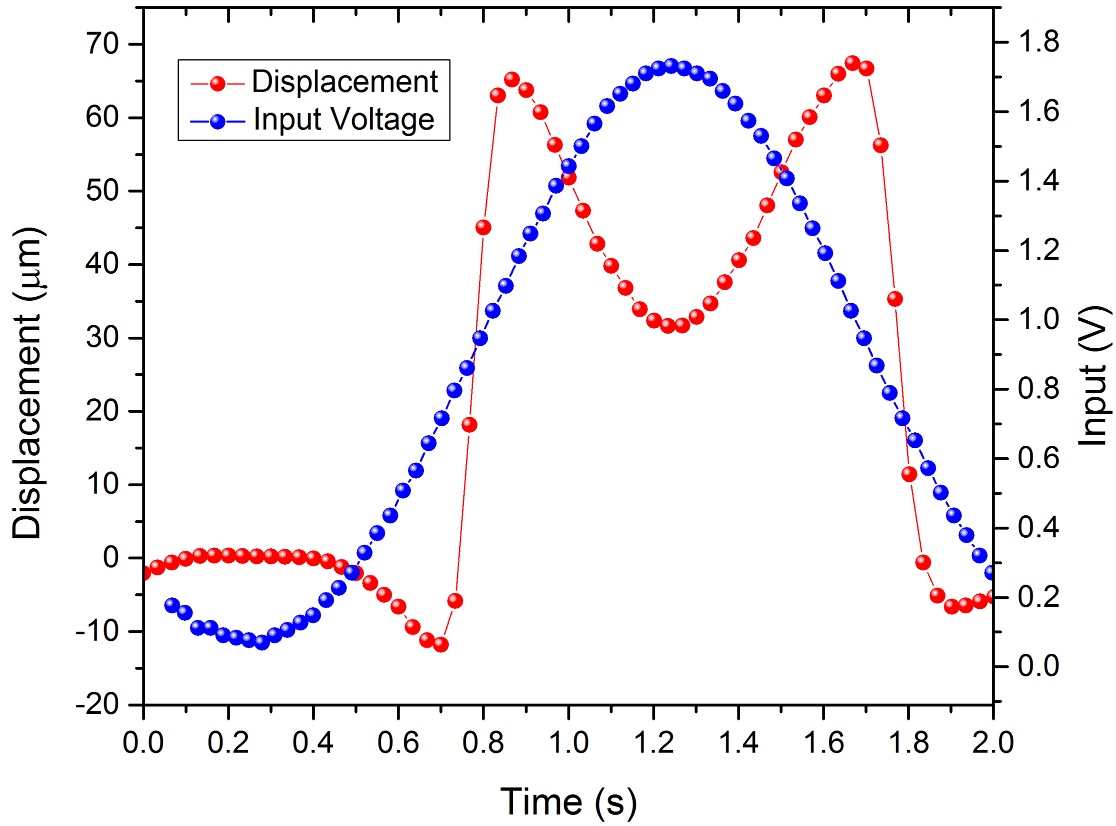

Figure 4.5 Piston movement displacement (red), by actuating all the legs with the same input voltage (blue) [18].

Table 4.1 Maximum Power Consumption for individual actuators for different input range.

Input Range	**Maximum Power Consumption (mW)**				
	Individual Actuation (Leg)				Piston Actuation
	1	2	3	4	
0 - 1.7 V	7.56	6.44	6.00	6.11	26.11
Across the phase transition	3.85	3.30	2.47	3.37	12.99

4.2 Summary

A MEMS mirror actuated by the phase change in VO_2 has been demonstrated for the first time. The deflection of the VO_2 -based MEMS mirror shows non-monotonic hysteretic behavior, characteristic of the mechanical actuation in MEMS induced by the solid--solid phase transition of VO_2. The device performance shows maximum vertical displacements and tilting angles of approximately 75 µm and 5.5°, respectively. The devices maximum displacement occurs within a change in voltage of only 0.38 V. Furthermore, the device have a high sensitivity across the transition for each actuator with estimated values of approximately 7 µm °C^{-1}, or 169.95 µm V^{-1}.

CHAPTER 5

CHARACTERIZATION & MODELING OF THE SECOND GENERATION VO_2-BASED MEMS MIRROR

The modeling of MEMS mirror is a necessity to better understand the behavior of the devices. Furthermore, the modeling enables the use of closed-loop control algorithm to precisely manipulate the movement of the device. A general dynamic equation (second-order differential equation) in terms of summation of torques has been used to describe the dynamic behavior of different MEMS mirrors [122, 123, 68]. The parameters of the equation are dependent on the mechanical structure and the actuation mechanism of the device. Different approaches have been employed to determine these values. In [122], an electrostatic MEMS mirror with sidewall and bottom electrode is characterized and modeled by deriving the theoretical model based on the mechanical properties of the device and the electrostatics forces. Similarly, an electromagnetic MEMS mirror with magnetic thin film is modeled in [123], where the external torque depends on the Lorentz forces between two magnetic fields from a bottom coil and the magnetic thin film. Another approach is presented in [68], where the parameters of the model for an electrothermal MEMS mirror are calculated from experimental results.

Different modeling methods have been proposed for the nonlinear behavior (hysteresis) of the VO_2-based MEMS devices. Nonlinear mathematical models such as the Prandtl-Ishlinskii model [124] and the Preisach model [28] have been adopted to capture and estimate the hysteresis behaviors. Unlike the identification of the Prandtl-Ishlinskii model, which requires solving a nonlinear optimization problem, the Preisach model identification problem can be reformulated as a linear least-squares problem and solved efficiently [28]. The Preisach model is thus adopted in this work. In order to control the systems with hysteresis, feedforward control can be realized by inverting the hysteresis nonlinearity [28], feedback control can be implemented as well, where the feedback signal can be obtained based on external sensors or with self-sensing methods [125]. In self-sensing, the correlation between the electrical and mechanical properties across the transition is utilized [30].

A mathematical model that describes the movement of a VO_2-based MEMS mirror based on the characterization of the device is presented. The modeling is focused on one of the four actuators of the device. First, the mechanical model of the system is derived, where the nonlinear behavior of the VO_2 is incorporated in the model as an external force applied to the system. A Preisach model is used to capture the hysteresis behavior of the VO_2. The parameters for the whole model are identified using simulation and experimental results. Finally, the hysteresis model is validated with a different set of experimental results including quasi-static and dynamic responses. The proposed model can be translated to other actuators of the MEMS mirror, and this work facilitates the control of the device.

5.1 Modeling

The device is characterized by actuating only one of the four actuators and measuring the tilting angle produced by the movement. Due to the symmetry of the device, the characterization of one leg can then be used to describe all the other actuators and derive the model for the entire device. The connection of each mirror leg to the mirror (as shown in **Figure** 5.1) is not symmetrical along a perpendicular axis crossing the platform's center, creating a 2-D motion. The 2D displacement comes as the result of not having identical contact areas for all the actuators symmetrical with respect to the center of the platform. This movement is captured by the 2D-PSD, and separated into two components: (i) pitch - rotation of the platform along the "Pitch Axis" (see **Figure** 5.2), and (ii) roll - rotation of the platform along the "Roll Axis" (see **Figure** 5.2). Both axes are perpendicular to each other, and thus, every planar (or 2D displacement) can be described by a combination of "Pitch" and "Roll" displacements. Therefore, the description and modeling of the system

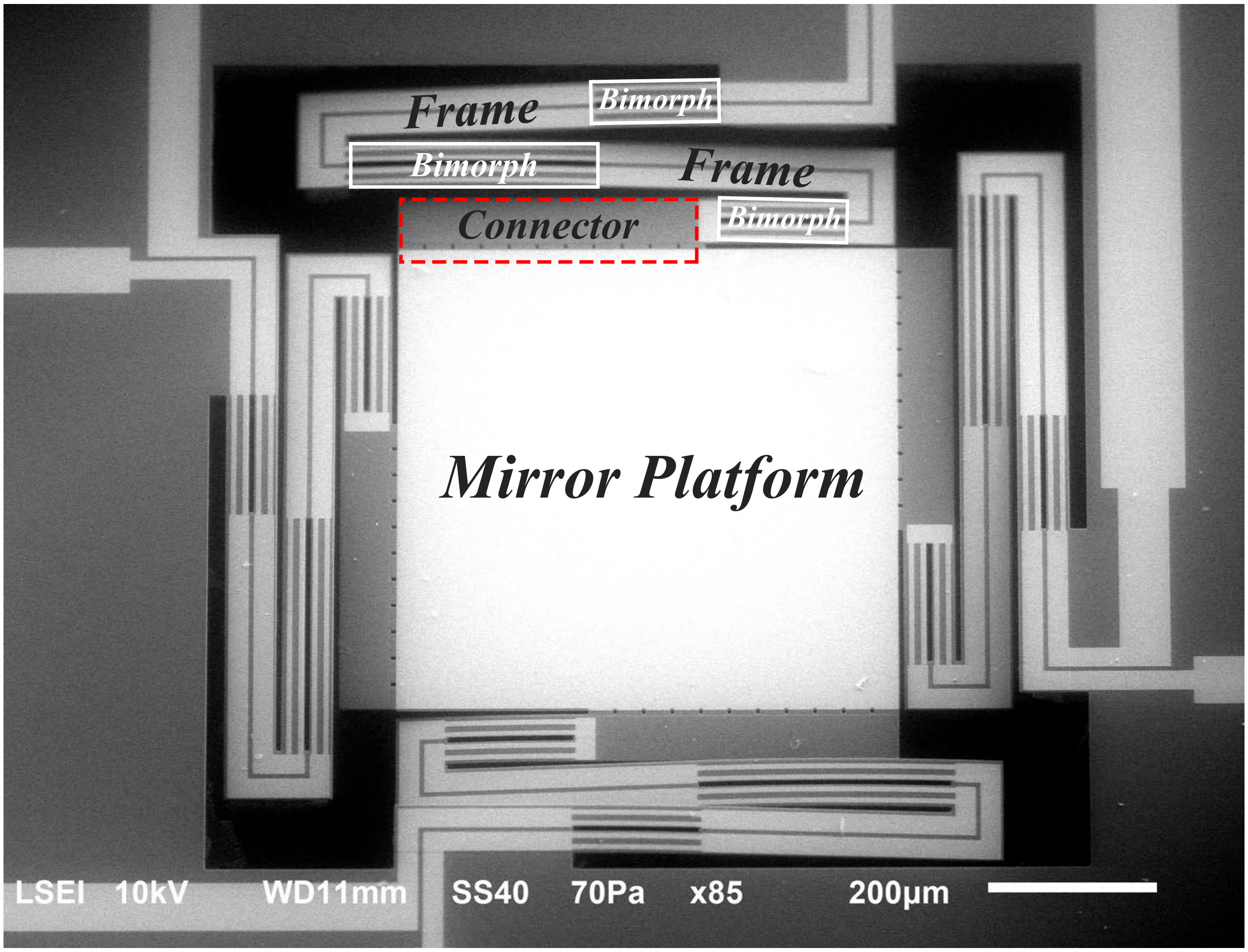

Figure 5.1 SEM image of a VO_2 -based MEMS mirror (top view), where the different parts of an actuator leg are label: frame, bimorph and the connector between the mirror platform and the actuator leg.

will involve movements along two perpendicular axes: pitch and roll. A set of two equations (one per degree of freedom: pitch and roll) is used to model the movement of the mirror. The inclusion of the VO_2 in the device adds a nonlinear term to the equations due the hysteretic behavior of the material. A non-monotonic Preisach model is developed to capture the hysteresis term. The effect of the VO_2 is included in the external force that generates actuation. The parameters for the linear part of the equation that describe the system's mechanical response are obtained from a combination of experimental measurements and finite element method (FEM) simulations (details in Section 5.1.1). The coefficients of the nonlinear part of the equation are calculated from a set of experiments (details in Section

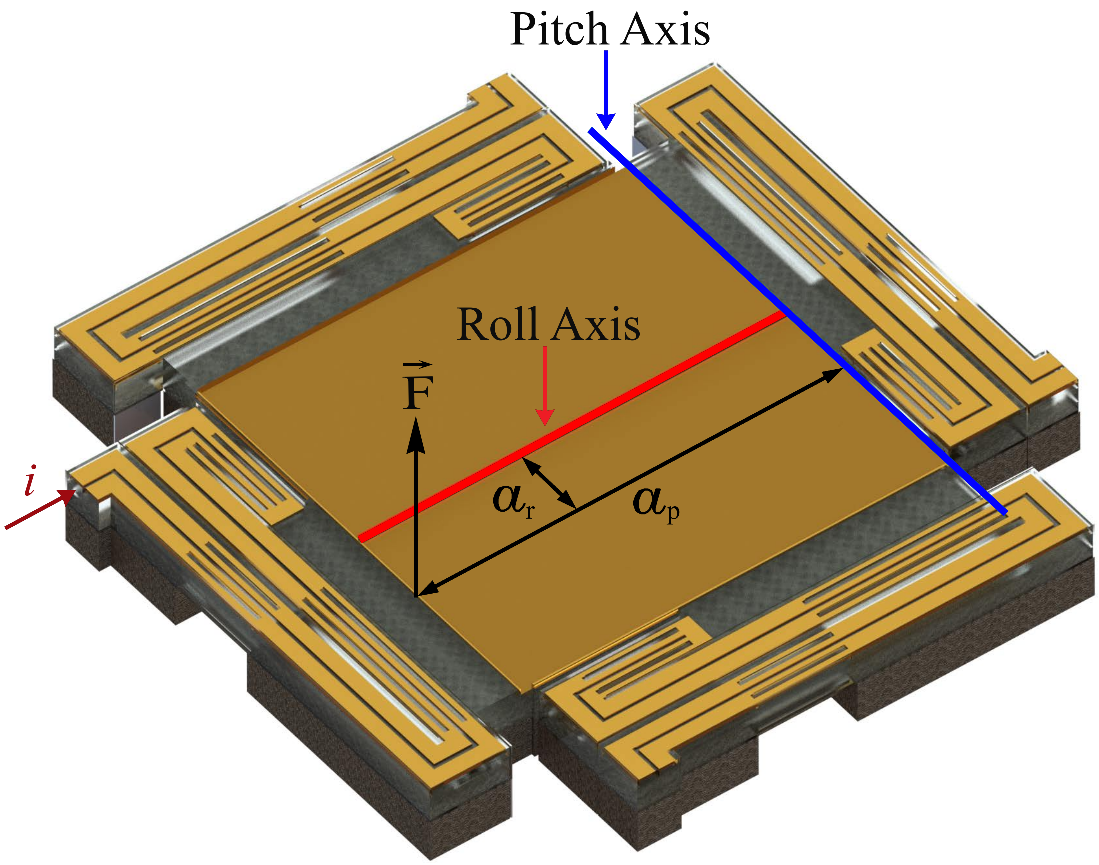

Figure 5.2 Schematic of the mirror platform showing the force ($\vec{F}$) applied by the actuated leg, and the axes of rotation for pitch and roll angles, where a_r (115 µm) and a_p (300 µm) are the distance between the force and each axis. In this case, the current i is applied to the bottom-left leg.

5.1.2).

5.1.1 Linear Model

The linear model characterizes the dynamic behavior of the system, which is approximated with a second-order differential equation

$$J\ddot{\theta} + G\dot{\theta} + k\theta = \vec{T}, \tag{5.1}$$

where J is the moment of inertia, G is the rotational damping coefficient, k is the rotational spring constant of the actuated leg, $\vec{T}$ is the external torque produced by the force $\vec{F}$, and θ is the angle of the mirror's platform generated during actuation. The characteristic equation of the system can be derived by applying the Laplace transformation to **Equation** (5.1) and rearranging the expression to get **Equation** (5.2):

$$s^2 + s\frac{G}{J} + \frac{k}{J}, \tag{5.2}$$

which is in the format of a second-order characteristic equation:

$$s^2 + s2\zeta\omega_n + {\omega_n}^2, \tag{5.3}$$

where ω_n is the resonant frequency and ζ is the damping ratio of the actuated leg. By combining **Equation** (5.2) and **Equation** (5.3), the moment of inertia and the rotational damping coefficient can be expressed in terms of resonant frequency and rotational spring constant:

$$J = \frac{k}{{\omega_n}^2}, \tag{5.4}$$

$$G = 2\zeta\frac{k}{\omega_n}. \tag{5.5}$$

The rotational spring constant (k) is calculated using FEM simulation of the mechanical structure, while ω_n and ζ are obtained from experimental results. The actuation force ($\vec{F}$) from VO_2 is represented in $\vec{T}$ via

$$\vec{T} = a \times \vec{F}, \tag{5.6}$$

where a is the distance between the force and the axis of rotation. The generated force (F) from the VO_2 can be expressed as:

$$F = \Gamma[T - T_0], \tag{5.7}$$

where T is the temperature of the leg, T_0 is the ambient temperature, and Γ is the hysteresis operator describing the relationship between the generated force and the temperature of the mirror leg. The thermal process (i.e., Joule heating) can be represented as follows [126],

$$\frac{dT(t)}{dt} = -d_1[T(t) - T_0] + d_2 i^2(t),$$
$$T' = T(t) - T_0,$$

where d_1 and d_2 are positive coefficients related to the properties of the materials, and i is the input current. Applying the Laplace transform to the previous equation results in,

$$sT' = -d_1 T' + d_2 i^2(s),$$
$$T' = \frac{d_2}{s + d_1} i^2,$$
$$T' = \frac{\frac{d_2}{d_1}}{\frac{s}{d_1} + 1} i^2 \Rightarrow \frac{A_T}{\tau_{th} s + 1} i^2;$$

where τ_{th} is the thermal time constant, A_T is the gain of the thermal transfer function. The external force can now be expressed as:

$$F = \Gamma[T'] = \Gamma[\frac{A_T}{\tau_{th} s + 1} i^2]. \tag{5.8}$$

The time constant and the gain A_T are found from experimental results. Finally, the torque generated by this force is expressed as:

$$\vec{T} = a\cos(\theta) \times \Gamma[\frac{A_T}{\tau_{th} s + 1} i^2], \tag{5.9}$$

which, since θ is close to zero and thus $\cos(\theta) \approx 1$, is simplified to

$$\vec{T} = a \times \Gamma[\frac{A_T}{\tau_{th} s + 1} i^2], \tag{5.10}$$

where the value a for the roll axis (a_r) is 115 µm and for the pitch axis (a_p) is 600 µm, as shown in **Figure** 5.2.

5.1.2 Nonlinear Model

The actuation force (F) is generated by two actuation mechanisms: one is the stress due to the thermal expansion difference of the materials forming the bimorph regions, and the other is the stress generated during the phase-change transition of the VO_2. Similar to [28], a non-monotonic hysteresis model is developed:

$$\Gamma[T'] = \Gamma_C[T'] + \Gamma_E(T'). \tag{5.11}$$

where $\Gamma_C[T']$ is the phase transition-induced force captured by a Preisach model, and $\Gamma_E(T')$ is the differential thermal expansion-induced force modeled as a linear term.

5.1.2.1 Phase transition-induced force

The relationship between the phase transition-induced force and the temperature is monotonically hysteretic, and a Preisach model [127] is employed:

$$\Gamma_C[T'](t) = \int_{\mathcal{P}_0} \mu(\beta,\alpha)\gamma_{\beta,\alpha}[T'(\cdot);\zeta_0](t)\mathrm{d}\beta\,\mathrm{d}\alpha + c_0, \tag{5.12}$$

where $\mathcal{P}_0$ is the Preisach plane $\mathcal{P}_0 \overset{\triangle}{=} \{(\beta,\alpha) : T_{\min} \leq \beta \leq \alpha \leq T_{\max}\}$, $[T_{\min}, T_{\max}]$ define the phase transition range, μ is the density function, $\gamma_{\beta,\alpha}$ denotes the basic hysteretic unit (hysteron), $T'(\cdot)$ is the temperature history, $T'(\eta)$, $0 \leq \eta \leq t$, and c_0 is a constant bias.

The hysteron is a memory-dependent operator. With the initial condition, $\zeta_0 \in \{-1, 1\}$, the output of the hysteron can be expressed as

$$\gamma_{\beta,\alpha}[T'(\cdot);\zeta_0] = \begin{cases} +1 & \text{if } T'(t) > \alpha \\ -1 & \text{if } T'(t) < \beta \\ \zeta_0 & \text{if } \beta \leq T'(t) \leq \alpha. \end{cases} \tag{5.13}$$

In practical usage, the integral expression of the Preisach model is typically approximated by discretizing the weight function μ to a finite number of parameters [127, 128]. The weight function is approximated as a piecewise constant function – the weight w_{ij} is constant within cell (i, j), $i = 1, 2, \cdots, N$; $j = 1, 2, \cdots, N - i + 1$, where N is called the discretization level and w_{ij} is the model parameter. At time n, the output of the discretized Preisach model is expressed as

$$\Gamma_C[T'(n)] = \sum_{i=1}^{N} \sum_{j=1}^{N+1-i} w_{ij} s_{ij}(n) + c_0, \tag{5.14}$$

where w_{ij} is the weight for the cell (i, j) that is non-negative, and $s_{ij}(n)$ is the signed area of the cell (i, j), which is determined by the history of the temperature values up to time n.

The model parameters consist of the weights $\{w_{ij}\}$ and the constant bias c_0. The model identification can be reformulated as a constrained linear least-squares problem and solved efficiently with the MATLAB command *lsqnonneg* [128, 28].

5.1.2.2 Differential thermal expansion-induced force

The differential thermal expansion-induced force is resulted from the thermal expansion difference of the VO_2 and SiO_2 layers. This component is modeled as a linear term and a quadratic term in previous studies [28, 125]. The following linear model is adopted in this work:

$$\Gamma_E(T') = -k_0 T', \tag{5.15}$$

where k_0 is a constant term related to thickness, modulus of elasticity, and thermal expansion coefficients of VO_2 layer and SiO_2 layer, and the negative term is introduced due to the fact that the thermal expansion-induced force has an opposite direction as the phase transition-induced force.

It is noted that the nonlinear model ((**Equation** (5.11)), (**Equation** (5.14)), and (**Equation** (5.15))) can be conveniently identified with the linear least-squares method [28]. It is shown in Section 4.3 that the proposed model can accurately capture and estimate the non-monotonic hysteresis behavior of the MEMS mirror.

Finally, combining all the terms, the equations describing the movement of the mirror can be expressed as:

$$J_p\ddot{\theta}_p + G_p\dot{\theta}_p + k_p\theta_p = \vec{T_p} = a \times \Gamma_p[\frac{A_T}{\tau_{th_p}s+1}i^2], \tag{5.16}$$

$$J_r\ddot{\theta}_r + G_r\dot{\theta}_r + k_r\theta_r = \vec{T_r} = a \times \Gamma_r[\frac{A_T}{\tau_{th_r}s+1}i^2]. \tag{5.17}$$

where the subscript p and r are references for the pitch and roll motions, the values for the linear parameters are presented in Table 5.3, Γ_p and Γ_r are the nonlinear models (**Equation** (5.11)).

5.2 Results and Discussion

5.2.1 Simulation Results

An FEM model is created in COMSOL to calculate the rotational spring constant of the leg. The parameters used for the materials on the simulation are shown in Table 5.1, and are taken from the COMSOL library and from [1]. The FEM model consisted of the entire MEMS mirror structure, including the four legs, the mirror platform, and all the material layers. A force sequence of increasing magnitude is applied as a point load at the top of the leg that connects to the mirror's platform. Four different simulations are run where

Table 5.1 Parameters of the materials used in FEM simulations, where the Si, SiO_2, and Au are obtained from the COMSOL library, while the VO_2 properties are reported in [1].

	Materials			
Properties	Si	SiO_2	Au	VO_2
Density $[Kg/m^3]$	2320	2200	19300	4670
Young's Modulus $[GPa]$	160	70	70	140
Poisson Ratio	0.22	0.17	0.44	0.33

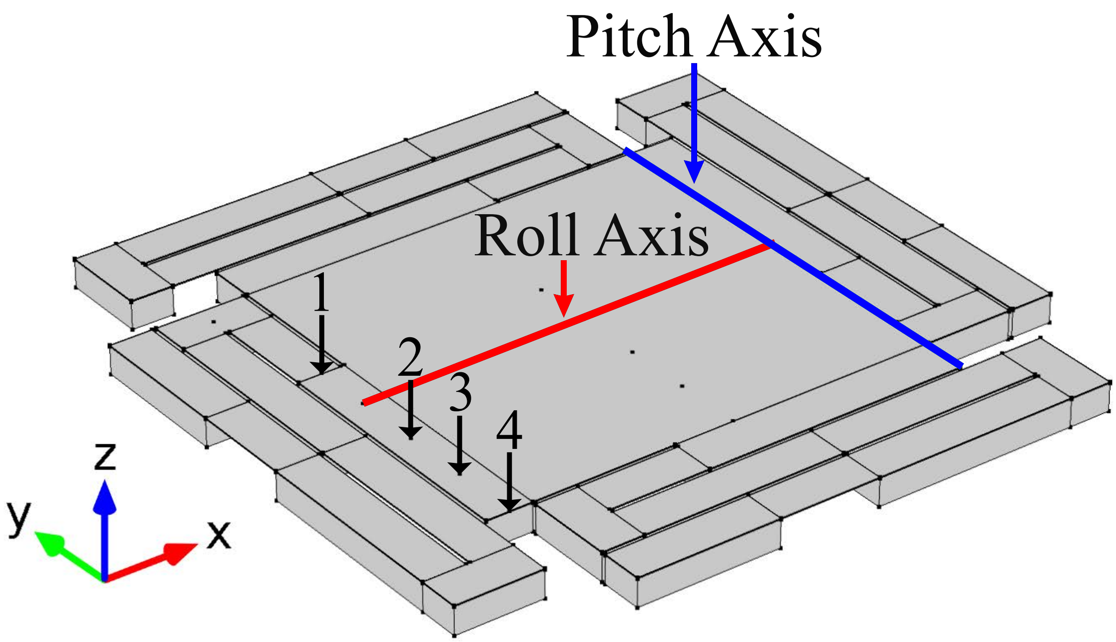

Figure 5.3 FEM model schematic of the VO_2-based MEMS mirror used to find the rotational spring constant by applying a sequence of increasing force as a point load. The force is applied at different locations (1,2,3 & 4) for each simulation.

the force is applied at different locations, as shown in **Figure** 5.3. The rotational spring constant at each location is extracted from the simulation results. To obtain the value of k, the displacement caused by the force is converted to an angle (θ_{sim}) with respect to each axis by using **Equation** 4.1 and is presented here again for simplicity,

$$\theta_{sim} = \sin^{-1} \frac{(h_1 - h_2)}{d}$$

where h_1 and h_2 are the displacements at the point load (caused by the force) and at the axis, and d is the distance between the point load and the axis. The torque is then calculated by using the distance between the point load location and the corresponding axis. Finally, the torque is divided by the angle resulting in the rotational spring constant of the leg. This is done for both angles (pitch and roll) and the results are shown in Table 5.2.

Table 5.2 Rotational spring constant from FEM simulation.

Point Load Location	Rotational Spring Constant	
	Pitch ($\times 10^{-9} \frac{N.m}{deg}$)	Roll($\times 10^{-9} \frac{N.m}{deg}$)
1	2.29	1.219
2	2.29	1.217
3	2.29	1.217
4	2.29	1.217

5.2.2 MEMS mirror mechanical model

A set of experiments are used to characterize the mechanical response of the structure and the nonlinear behavior of the VO_2, when actuating only one leg. The schematic of the experimental setup is shown in **Figure** 4.1, where the 2-D PSD is used instead of the 1-D PSD. The 2-D PSD facilitated the alignment of the setup and capture the 2-D movement of the device. The laser setup is aligned to match the X direction of the PSD with the pitch angle and the Y direction of the PSD with the roll angle. The resolution of the optical setup is 0.577 µm/pixel with a speed of 30 frames/second. Before each experiment, a pre-heating stage is performed to improve the stability and repeatability of the measurements, caused by the use of gold as the metal trace [129, 130]. A similar process is performed in [10], where a sine wave is applied as the input voltage to anneal the metal layers. For the VO_2-based MEMS mirrors in this work, the pre-heating stage consisted of applying a 12 mA to all of the actuators for a total of 10 min. An input sequence of increasing voltage steps is used to measure the thermal time response of the actuated leg. The input is applied to the base of the transistor and had increasing amplitude steps of 0.5 V, which corresponds to $\approx$ 0.7 mA (once the transistor is on). Each step is held for 1 second before the next step started. The thermal time response (τ_{th}) within steps is calculated from the rise time using the following equation:

$$\tau_{th} = \frac{t_{rise}}{2.2}, \tag{5.18}$$

where t_{rise} is the time taken for the structure to go from 10% to 90% of the output signal for one step. The results are shown in **Figure** 5.4. The thermal time response is calculated where the main dominant actuation mechanism is the thermal expansion difference of the materials forming the bimorph and not the transition of the VO_2, the values for the pitch and roll movements are 14 ms and 14.79 ms. During the transition of the VO_2, the system showed a pseudo-creep effect where each step took longer to reach steady state compared to outside the transition. This effect can be caused by the added stress from the legs that are not actuated. The added stress can move the transition temperature of the VO_2, which has been observed previously in VO_2 thin films [96, 97]. Even more relevant to the present case, this effect is also observed in VO_2-based MEMS mirrors [18], where it is found that individual leg actuation and piston-like actuation required different actuation voltages – note that during individual actuation, the remaining mirror legs add a stress that is not present during piston-like movement. The pseudo-creep is not included in the modeling of the device, in order to focus on the fundamental thermal and mechanical dynamics in the general case; and as verified in later experiments, the presented model (ignoring the creep effect) shows adequate capability in predicting the mirror dynamics.

A frequency response measurement is performed to observe the mechanical response of the system. A sine wave signal ($i = 1.4\sin(2\pi f t) + 0.00714$ mA) is applied as the input of one of the legs while the frequency is swept from 0.1 Hz to 2000 Hz. The magnitude of the displacement is measured across the whole range of frequency, then it is divided by the magnitude of the input current. Using the software Origin Pro9.0 the data is fitted using the magnitude of **Equation** (5.19), with a R^2 of 0.856 and 0.7797 for roll and pitch, respectively. **Equation** (5.19) is a linear approximation of the system, including the thermal and mechanical dynamics. Although the thermal response of the system in **Equation** (5.19) cannot capture the nonlinear behavior of the VO_2, it does capture the mechanical response

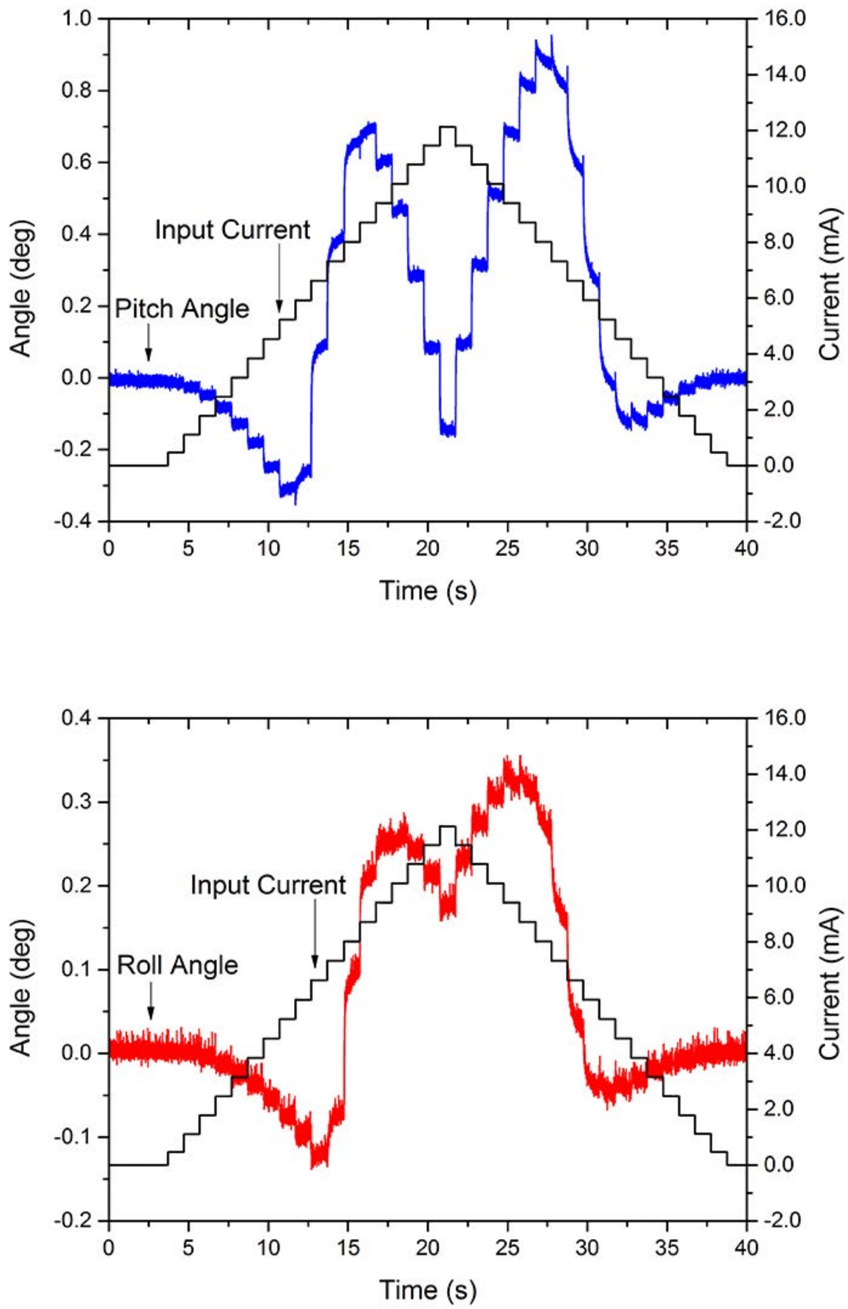

Figure 5.4 Time response measurements from actuating one leg for both variables: pitch (top) and roll (bottom) angles.

of the system. The values for the resonance frequency (ω_n) and the damping ratio (ζ) for each degree of freedom are found by a curve fit – fitting parameters are shown in **Figure**

5.5.

$$\frac{\theta}{i^2} = \frac{A_T}{\tau s + 1} \frac{{\omega_n}^2}{s^2 + 2(\omega_n)\zeta + {\omega_n}^2}. \tag{5.19}$$

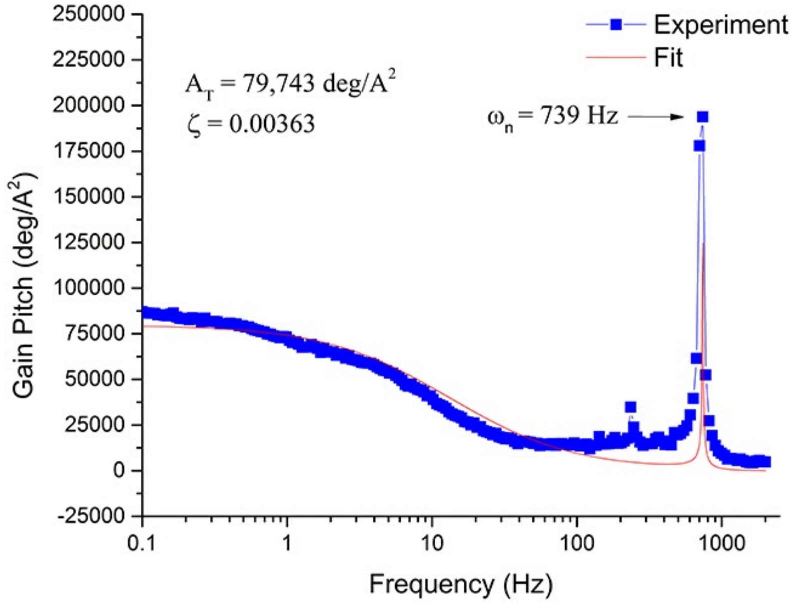

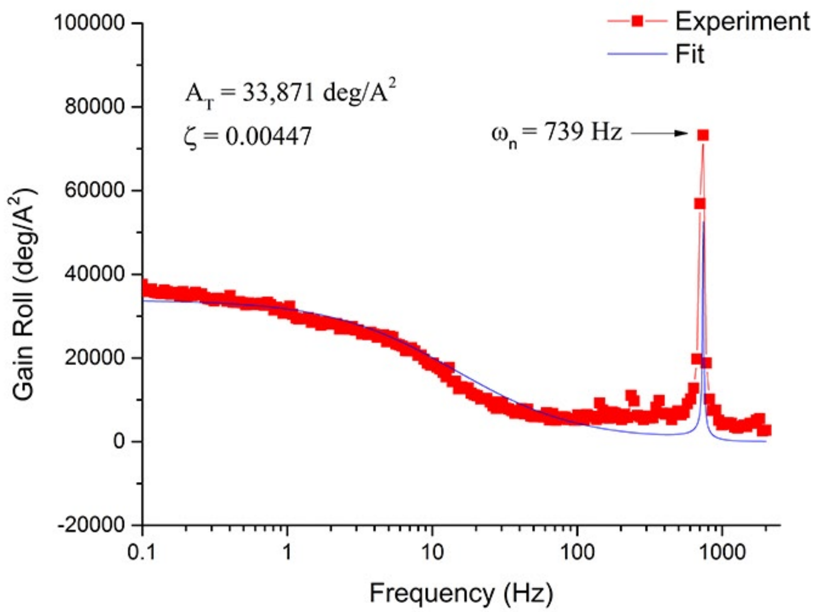

Figure 5.5 Frequency response for the actuation of one leg. A fitted curve is used to find the damping ratio (ζ) and the gain A_T. Both pitch (top) and roll (bottom) angles have the same resonant frequency with the value of 739 Hz.

5.2.3 Identification and Verification of VO_2 Hysteresis

5.2.3.1 Identification

A quasi-static measurement is performed to observe the static behavior of the leg across the phase transition. A series of current steps (each held for 550 ms) are applied to one of the legs with intervals of 0.1V. The steady-state values are obtained by averaging the last 50ms of the pitch and roll angles. This measurement will also be used to identify the unknown variables of the hysteresis model, since it contains the minor loops of the hysteresis. The plots are shown in **Figure** 5.6. It is shown that both of the hysteresis curves exhibit non-monotonic behavior.

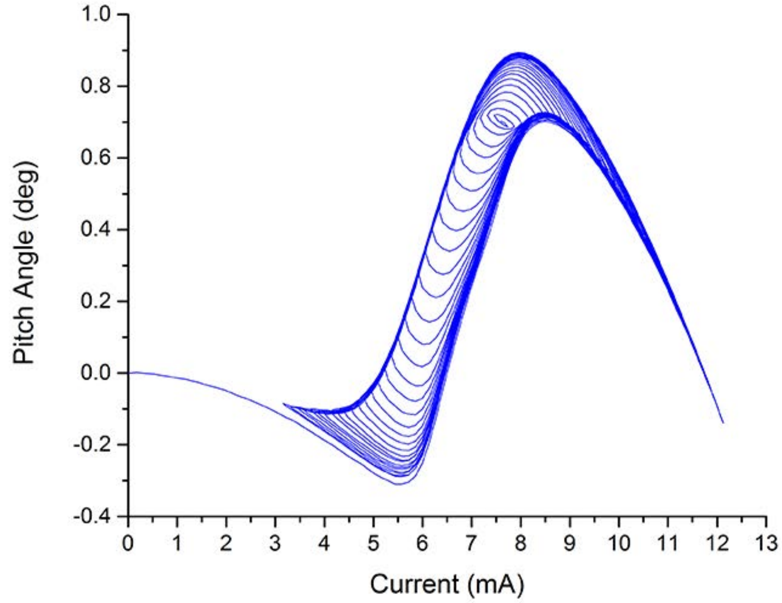

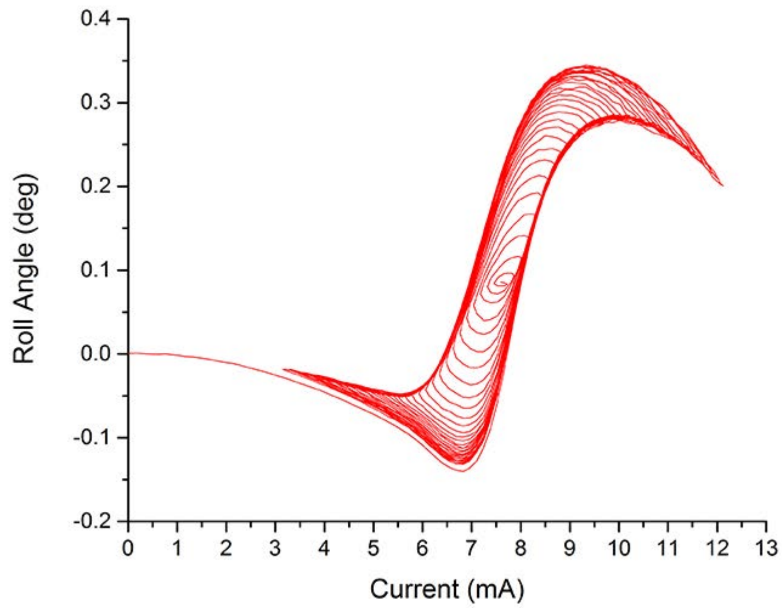

Figure 5.6 Identification plots of the pitch (top) and roll (bottom) angles, used to find the coefficients of the hysteresis model.

In order to identify the proposed model, the discretization level (N) of the Preisach model (Γ_C) is chosen to be 20. Further increasing the discretization level would increase the model complexity, but do not generate significant improvement in modeling accuracy. The root-mean-square error (RMSE) is chosen to quantify the accuracy of the model identification and verification results.

Figure 5.7(a) and **Figure** 5.7(b) show the identified weights of the Preisach models for the pitch and roll motions, respectively. **Figure** 5.7(c) shows the modeling performance for the hysteresis between the pitch angle and the current input, and **Figure** 5.7(d) shows the corresponding modeling error. The RMSE is 0.007 degree. Similarly, **Figure** 5.7(e)-(f) shows the modeling performance for the hysteresis between the roll angle and the current. The RMSE is 0.003 degree. It is shown that the proposed model can accurately capture the non-monotonic hysteresis of the MEMS mirror.

Table 5.3 Coefficient values of the model.

Constant	Name and units	Pitch (θ_p)	Roll (θ_r)
A_T	Gain $[deg/A^2]$	79,743	33,871
τ_{th}	Time response $[s]$	0.0014	0.001479
ω_n	Resonant Frequency $[rad/s]$	4643	4643
ζ	Damping ratio	0.00363	0.00447
J	Moment of Inertia $[Kg \cdot m^2]$	6.10×10^{-15}	3.23×10^{-15}
G	Rotational Damping coefficient$[N \cdot m \cdot s/rad]$	205.6×10^{-15}	134×10^{-15}
k	Rotational Spring coefficient $[N \cdot m/rad]$	132×10^{-9}	69.7×10^{-9}
a	Position of the force with respect to the axis [µm]	600	115
c_0	Constant bias of Preisach model [deg/µm]	0.99	0.38
k_0	Thermal expansion-induced force term [N/^{0}C]	1.4×10^4	3.8×10^3

5.2.3.2 Quasi-static verification

The model identification results show that the proposed model can effectively capture the hysteresis under the chosen current step input. To confirm that the model can reliably and robustly predict the pitch and roll angles under any reasonable step input, additional

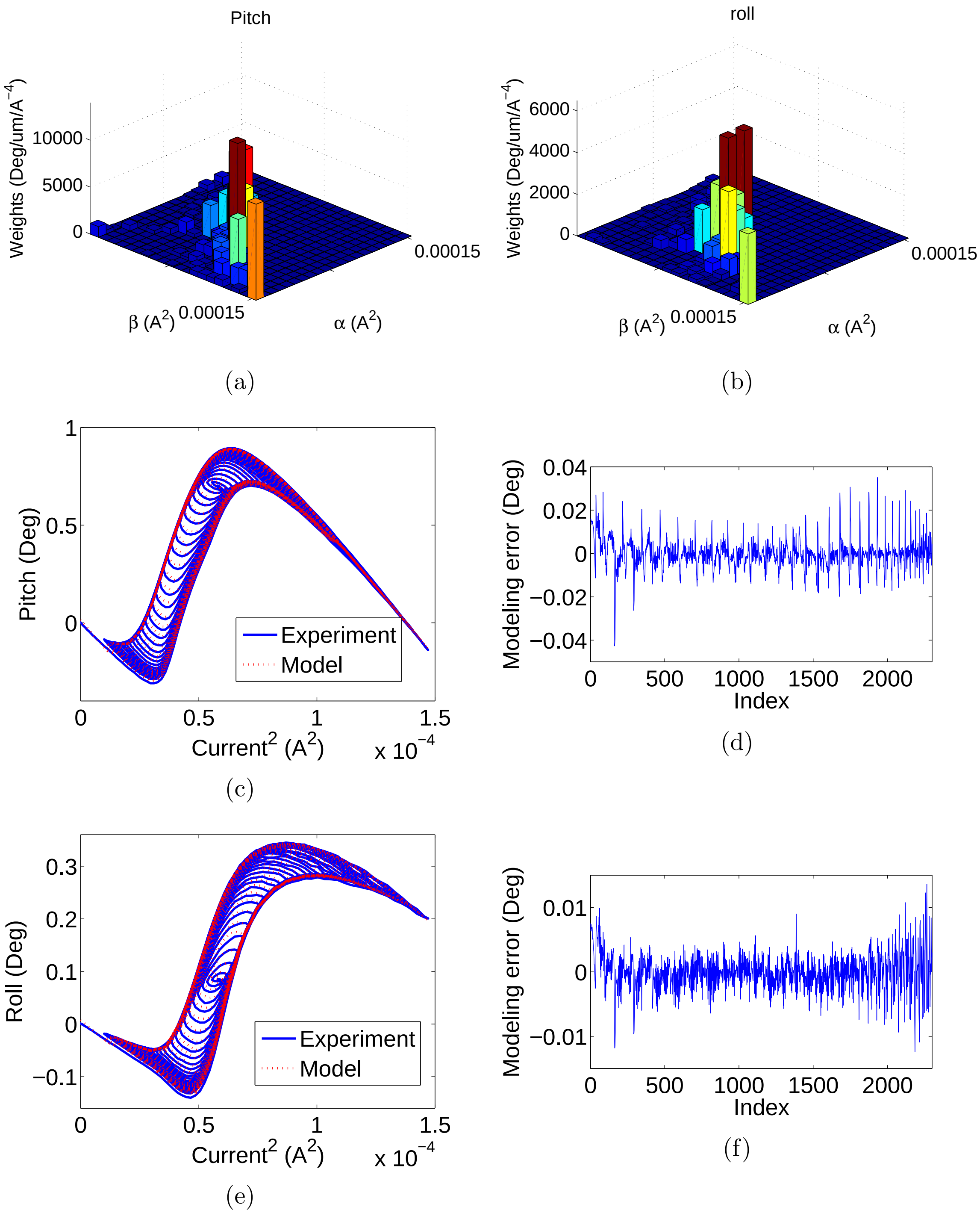

Figure 5.7 Parameters values (weights) used in the Preisach model for the (a) pitch and (b) roll. (c). The modeling performance, and (d) modeling error for the hysteresis between pitch angle and the current input. (e). The modeling performance, and (f) modeling error for the hysteresis between roll angle and the current input.

experiments utilizing random step inputs are conducted. A randomly-chosen current step input, as shown in **Figure** 5.8(a), is applied to the MEMS mirror. Each step is held for 1 second and the corresponding steady-state pitch angle and roll angle are recorded. **Figure** 5.8(b) shows the pitch estimation performance, and the RMSE is 0.027 degree. **Figure** 5.8(c) shows the roll estimation performance, and the RMSE is 0.013 degree. The effectiveness of the nonlinear model is confirmed.

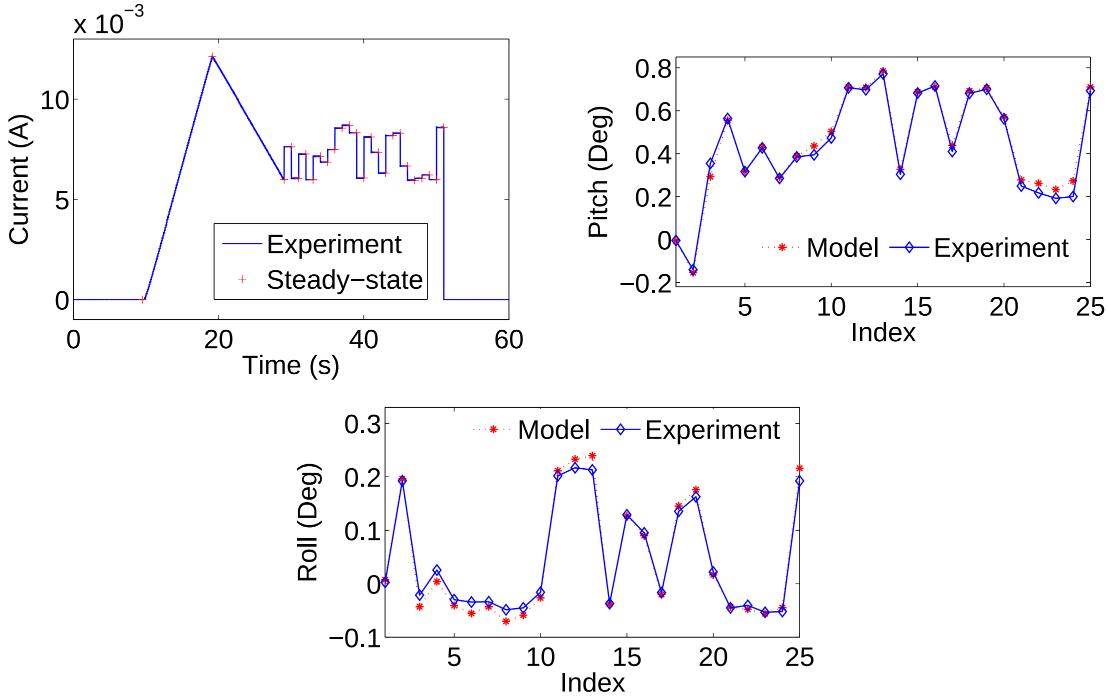

Figure 5.8 (a). A current step input for model verification. The measured and estimated steady-state (b) pitch angle, and (c) roll angle.

5.2.3.3 Frequency verification

In order to verify that the model can effectively predict the performance of the mirror under dynamic inputs, sinusoidal current inputs with different frequencies are applied to the mirror, and the corresponding pitch angle and roll angle are recorded (**Figure** 5.9). As can be seen, the hysteresis relationships between the pitch angle and the current, and between the roll angle and the current, change under different frequencies. On average, the RMSE pitch angle

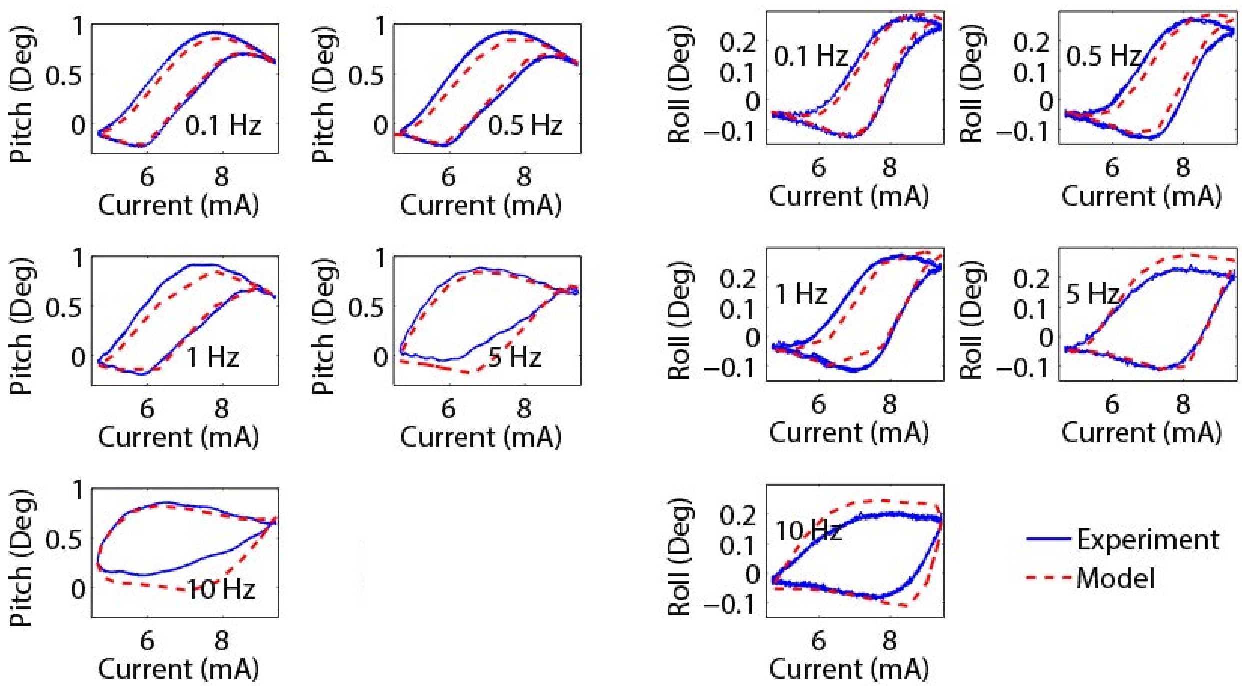

Figure 5.9 The pitch and roll angle verification performances for current inputs with different frequencies.

estimation error is 0.074 degree and the RMSE roll angle estimation error is 0.031 degree. The model can capture the dynamic mirror motions reasonably well. It is noted that the estimation error becomes larger under higher frequencies, which is likely due to the mild discrepancies between the actual and calculated time response values.

5.2.3.4 Multi-frequency verification

Furthermore, the model verification for multi-frequency inputs has been conducted. The current input ($1.35\sin(2\pi t) + 1.35\sin(10\pi t) + 1.35\sin(20\pi t) + 0.00705$ mA), as shown in **Figure** 5.10(a), is applied to the system. The model estimation performances for the pitch and roll angles are shown in **Figure** 5.10(b) and **Figure** 5.10(c), respectively. The RMSE pitch angle estimation error is 0.097 degree and the RMSE roll angle estimation error is 0.033 degree. The effectiveness of the proposed model for the MEMS mirror is thus further validated.

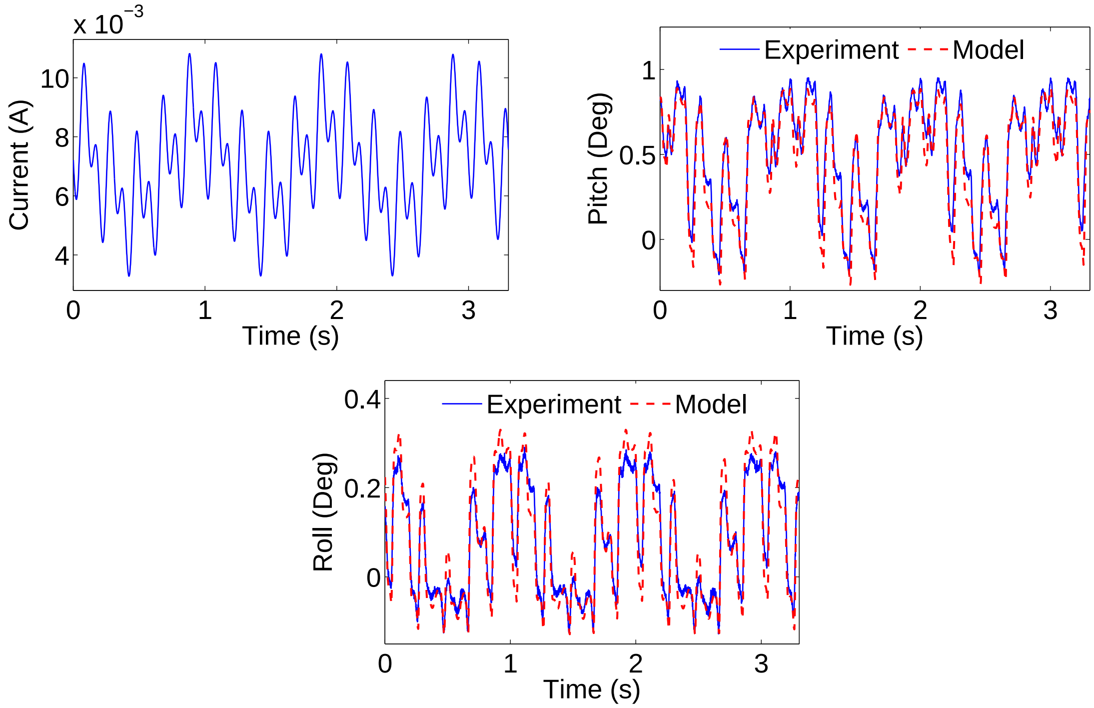

Figure 5.10 (a). A multi-frequency current input for model verification. The measured and estimated (b) pitch angle, and (c) roll angle.

5.3 Summary

In this chapter, the model for the VO_2-based MEMS mirror is derived and verified. The model included mechanical and thermal processes, and accounted for nonlinear behavior, typically found in most phase-change materials. The approach for the modeling involves a combination of theoretical and experimental results, resulting in a comprehensive hybrid analysis. Although the emphasis of the present work is on MEMS mirrors actuated by phase-change materials, particularly VO_2, the work can be extended to simpler designs and actuation methods. Therefore, the present work presents a platform that can be adapted for the design of a broad scope of MEMS mirrors.

CHAPTER 6

PROGRAMMING OF THE VO_2-BASED MEMS MIRROR

Programmable devices are those that are capable of storing a measurable variable for a period of time, creating different states. Basic examples of this are capacitors, where electrical energy is the stored variable [131, 132] creating a minimum of two states: charged and discharged. Similar to this, MEMS devices are capable of storing electrical or mechanical variables such as, voltage [133, 134, 135], resonant frequencies [24] or displacements [23, 17, 136]. In [135], MEMS and CMOS technologies are combined to create devices capable of storing voltage values in two different states, by charging/discharging a floating gate of a transistor with a mechanical switch. Programmed displacement values can be stored in an external circuitry, which works as the system's memory by saving the inputs signal for each desired state. An example of this is the digital mirror presented by Texas Instrument, Digital Micromirror Device (DMD)[35], where the device includes a CMOS memory circuit. Another approach is creating bi-stable MEMS devices, where 2 states are programmed and accessed using electrical or mechanical stimulus [137, 138]. The disadvantage of these approaches is that systems are limited to two states. To overcome this, a different approach for programming mechanical outputs has been implemented by exploiting the nonlinearity observed in certain MEMS devices. For example, in [23] the hysteresis caused by the VO_2 was used to created different programmable states in a cantilever beam, where each state is a different position of the cantilever. This technique was also implemented in VO_2-based resonators in [24], where the programmable variable is the resonant frequency. Recently in [136], an ES MEMS resonator used this technique to design a programmable resonator, where the amplitude of the resonant frequency is the programmable variable.

This chapter presents, the memory capability of the VO_2 in MEMS mirror, using the second generation of VO_2-based MEMS mirror. The hysteresis of VO_2 was exploited to program different displacements states. Two actuation modes are programmed: a tilting angle and a piston-like movement.

6.1 Results and Discussion

The programming of the VO_2-based MEMS mirror was performed for two actuation modes: tilt and piston-like movement. The tilt mode was done by actuating only one leg, which created a 2D movement: pitch and roll (as explain in Chapter 5). The measurement setup

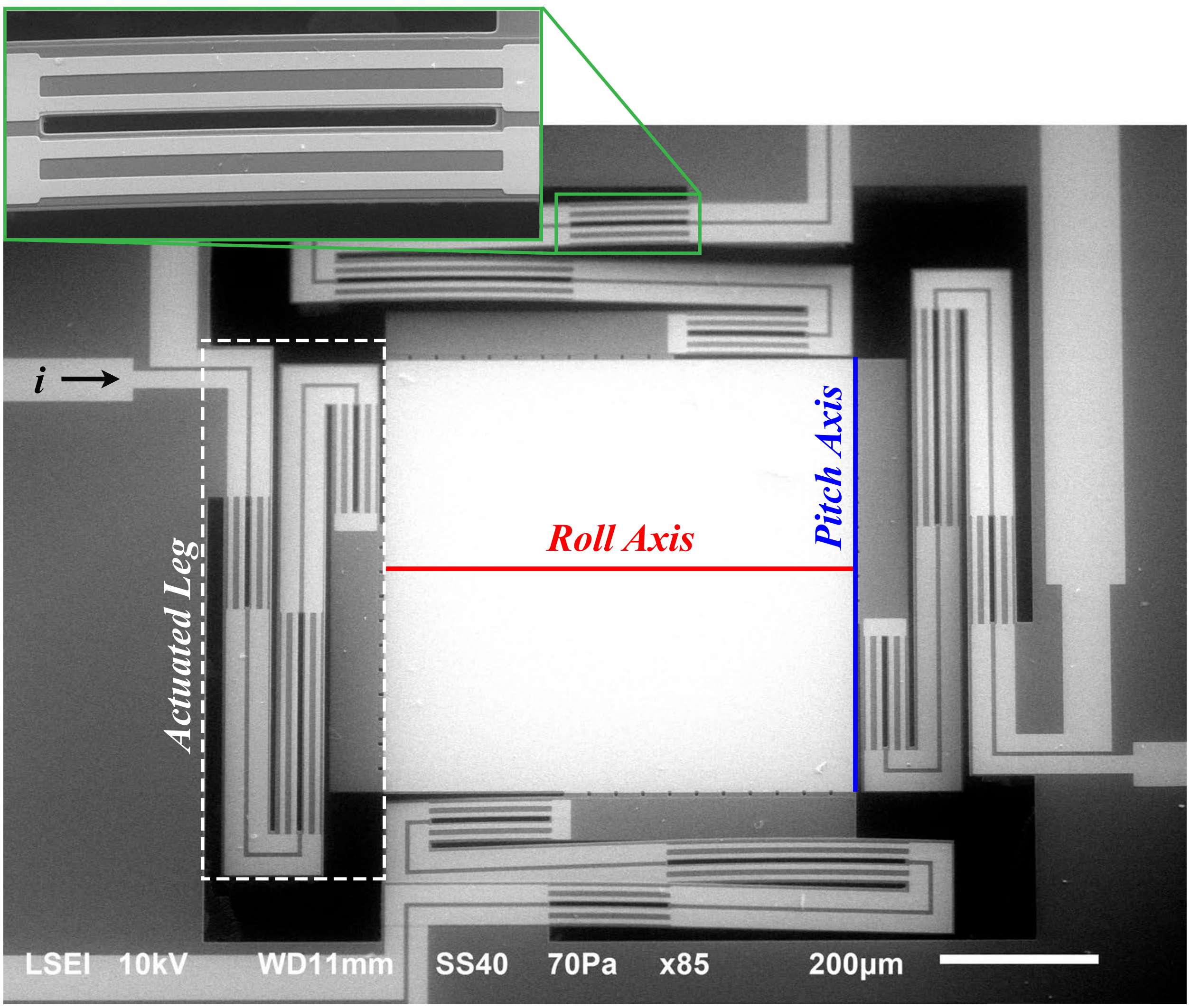

Figure 6.1 SEM images of the second genreation VO_2-based MEMS mirror with Cr/Au traces, where the rotational axes are labels for the actuated leg.

used for the presented experiments is describe in Chapter 5. The resolution of the optical setup depends on the alignment and position of the camera and the lens, and the recording speed of the camera, with values of 0.5 µm/pixel and 0.75 µm/pixel for 30 Hz and 60 Hz, respectively. The optical setup (without the laser scattering) was used to track the displacement of the piston mode (explain in later section). For the tilt-mode, the input current was controlled using a BJT NPN transistor (2n3904) in an emitter follower configuration.

The piston-mode is generated by actuating all the legs at the same time. During this mode, the synchronization of the legs is obtained by ensuring the same input current is applied across the resistive heaters of the legs. Due to the high quality of the metal patterning (as shown in the inset in **Figure** 6.1), the difference between resistive heaters are not considered. To ensure the same current is applied to all the legs, they are connected in series with a voltage amplifier (THORLABS HVA200), controlled by the NI-DAQ, connected in parallel to the legs. An additional resistance (98.3 Ω) is added in series to the legs to measure the voltage and calculate the current passing through the legs. Even though this configuration guarantees the same power to all the resistive heaters, there is still a very small rotational component measured by the 2D PSD, which is not noticeable in the recorded videos. This small rotational angle could be due to small differences in the hysteretic curves for the VO_2 between the actuators; or non-uniformities in the fabrication process flow -especially in the isotropic etch of Si using XeF_2. Since the field of view of the optical setup is limited to a single side of the platform, it is not possible to accurately map this small angle to a vertical displacement in piston-mode. Therefore, piston-mode displacement measurements are obtained using the optical view from the camera.

6.1.1 VO_2-hysteretic behavior

The hysteretic behavior of VO_2 enables the capability of creating different programmable states (both tilting angles for tilt-mode, and vertical displacements for piston-mode) for given current pulses. In order to clearly demonstrate the programming of these states, we first applied a DC current input that pre-heated the system to a state within approximately the midpoint of the hysteresis. Then, the current is monotonically increased to reach a "high state", and then monotonically decreased to reach a "low state". Although we present the programming of only two states, it is possible to program multiple states within the hysteresis of VO_2. The process can be repeated to move between states, as long as the variation of temperature (or applied current pulse) has the same amplitude. For accessing different states using the same pre-heated stage value, it is necessary to reach different points within the hysteresis, which would require programming pulses of different magnitude. An alternative approach for obtaining different states would be to change the initial state before applying programming pulses, which could be done by changing the pre-heating stage. If the pre-heated stages are different, the same input programming pulses would result in different programmed states. Depending on the pre-heated stage and the magnitude of the programming pulse, it is possible that the final state falls within the two major hysteretic loops that are defined for a monotonic heating-cooling cycle that crosses the entire phase transition region [110]. Programming states above the pre-heated state would require positive input pulses that first increase temperature and then decrease to the initial pre-heating temperature; while programming states below the pre-heated state would require input pulses that first decrease temperature and then increase to the initial pre-heating temperature. For the presented device, the temperature is controlled with the input current using Joule heating. A constant current is used as the pre-heating stage, positive and negative pulses (relative to the pre-heating stage) are applied to the current to move between the programmable states.

To measure the hysteresis, a triangular input sequence is applied. In order to measure the major hysteresis loop, the input is a monotonically increasing-decreasing loop that covered the entire phase transition of VO_2, shown in **Figure** 6.2. The results for both actuation mode shows a non-monotonic behavior caused by the combination of two actuation mechanisms: the difference in TECs between the layers of the bimorph and the transition of the VO_2. Before and after the phase transition of VO_2 the actuation of the device is dominated by the difference in the TEC, this is observed as the outputs signal decrease in values. Once the temperature reach the transition temperature, the transition of the VO_2 dominates as the actuation mechanism and this is confirmed by the direction of the movement, where in both actuation modes the output signal increased. Note that the required current values needed for full actuation for piston mode are smaller than that for the tilt mode. This is caused by the difference in extrinsic stress over the VO_2 film, between the actuation modes. In [18], it is observed that the mechanical coupling of the legs affected the transition of the VO_2. This is believed to be due to the extrinsic stress added by the non-actuated legs on the actuated leg. The non-actuated legs behave as static springs, creating an opposite force against the movement of the actuated leg. When all the legs are actuated (i.e. piston actuation), this extrinsic stress does not exist –or at least is significantly reduced. Given that an external stress can shift the VO_2 transition temperature[96, 97], the required current to actuate one leg (tilt-mode) is different from the current required to actuate all the legs (piston-mode).

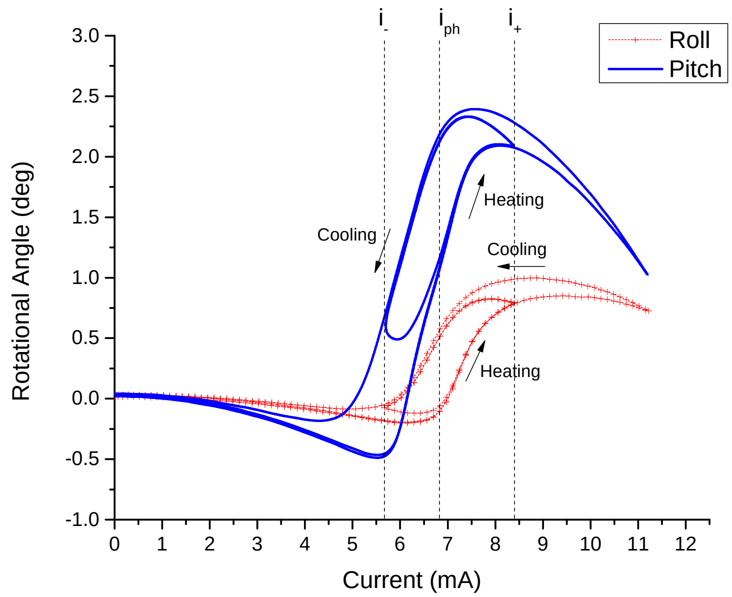

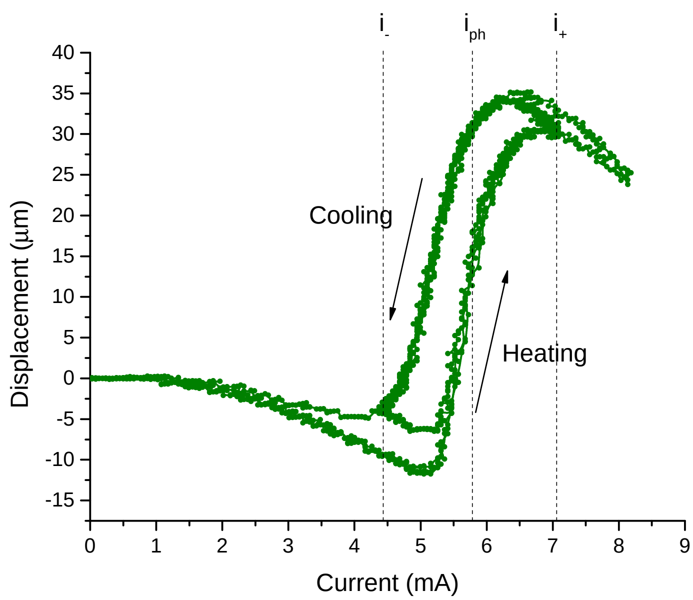

Figure 6.2 Hysteretic behavior caused by VO_2, when a triangular input is applied for the major loop, observed on both modes: top) rotational angle of the tilt-mode and, bottom) vertical displacement of the piston-mode. The minor loop are taken after the first input signal by applying another triangular input signal with a minimum and maximum values of of i_- and i_+.

Although it is possible to program any state enclosed by the major hysteretic loop, for purposes of simplicity of the proof-of-concept, we focused the experiment on two different states: one above, and one below a pre-heated state. The experiment required three different current references: a constant current (i_{ph}) –to remain inside the hysteresis; a high current value (i_{+}) –to reach the high state; and a low current value (i_{-}) –to reach the low state. It should be noted that a particular input programming sequence is applied for each mode. This generated programmed rotational angles for the tilt-mode, one for the pitch and another for the roll (see **Figure** 6.2-top), and a programmed vertical displacement for the piston-mode (see **Figure** 6.2-bottom).

6.1.2 Time Response

Time response experiments are performed to study the thermal time response of each actuation mode. The pulse width for the programming pulses can then be set larger than the thermal response time, so as to reliably and sufficiently heat-up the device. A sequence of current steps of increasing magnitude is applied as the input, while the outputs (rotational angle for the tilt-mode and vertical displacement for the piston-mode) are measured. Two actuation mechanisms can be seen from the output signals, where the decrease in output signal between steps is caused by the difference in TECs between the layers of the bimorph, while the increase in the output signal is due to the phase transition of VO_2. The results are shown in **Figure** 6.3 and summarized in Table 6.1. The time constants are calculated from the measure rise time (t_{rise}), using the following relationship between them: $\tau = t_{rise}/2.2$. The rise time of the signal is measured from the 10% to 90% of the output signal for each step outside the transition of the VO_2. Across the transition of the VO_2, the extrinsic stress (caused by the mechanical coupling between the legs) alters the transition temperature of the VO_2 [96, 97], but not the time constant of the VO_2 phase transition. It has been reported in [25, 139], that the VO_2 transition induced by a gradient of temperature is as fast as the temperature change. The extrinsic stress causes a pseudo-creep effect in the mechanical response of the device during the VO_2 transition, increasing the time needed to reach the steady-state. The thermodynamics of the system is independent of a mechanical stimuli, such as an extrinsic stress, because of this the thermal time response is obtained outside the transition of the VO_2, where the difference in the TEC between VO_2 and SiO_2 dominates the actuation.

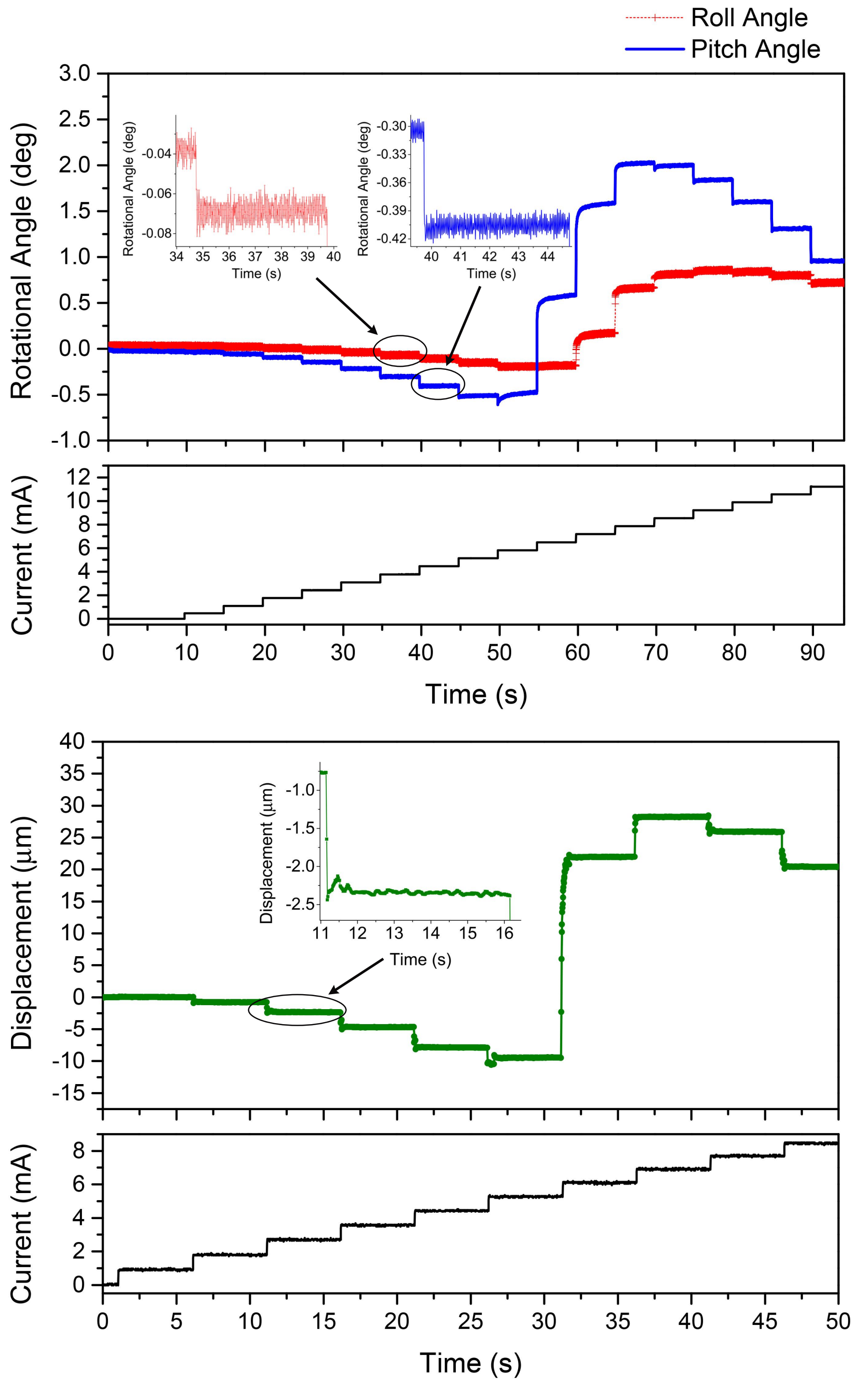

Figure 6.3 Step response measurements where the output and the input are shown for both modes: top) rotational Angle of the tilt mode and, bottom) vertical displacement of the piston mode.

Table 6.1 Thermal time response of each mode.

Mode		Current (mA) Thermal Time Constant (ms)
Tilt	Pitch	6.3
	Roll	10.7
Piston		11.3

6.1.3 Programming

The programming for both modes is performed by first applying an input current that increased the temperature up to the preheated stage (i_{ph}), followed by a sequence of pulses to move between states. A positive current pulse (i_+) is used to move to the higher state, while a negative pulse (i_-) is used to move to the lower state. With each input pulse, the temperature of the actuated part is increased (or decreased, depending on the pulse) momentarily. The values of the current references used for the programming of two states are demonstrated in **Figure** 6.2 and shown in Table 6.2. To ensure the temperature has reached a steady-state, the pulse width is chosen to be longer than the time response of the modes, with a value of 300 ms. The results are shown in **Figure** 6.4, where the 2 states between the pulses are clearly observed.

Table 6.2 Input current references used for the programming of 2 states for each mode.

	Current (mA)		
Mode	i_-	i_{ph}	i_+
Tilt	5.74	6.83	8.39
Piston	4.42	5.78	7.09

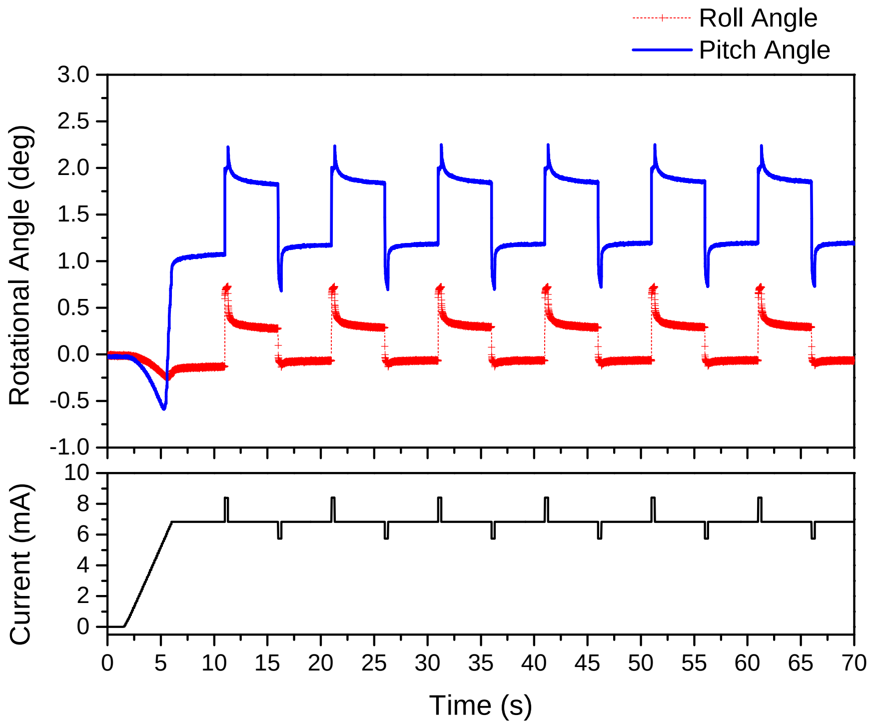

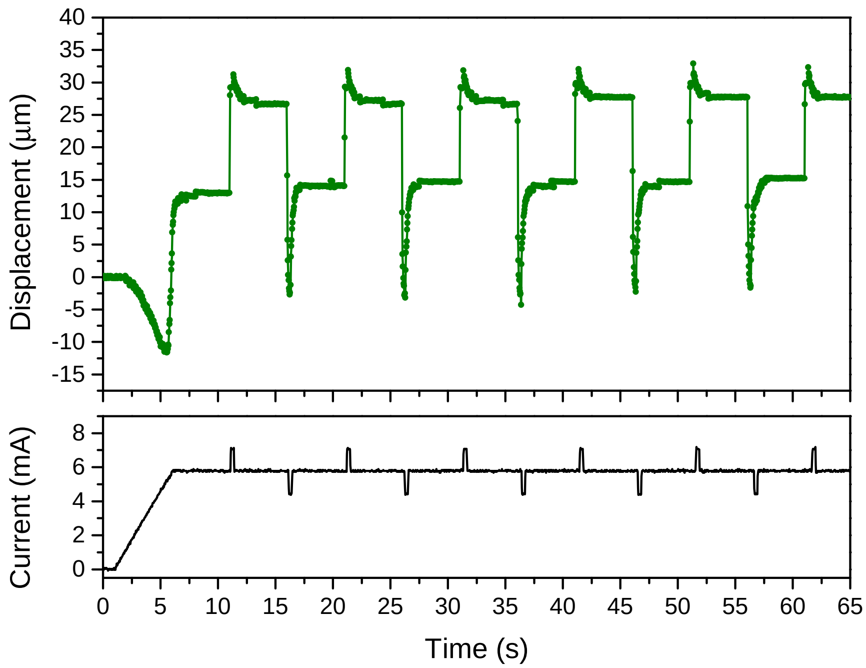

Figure 6.4 Programming of 2 states on the different modes: top) rotational Angle of the tilt mode and, bottom) vertical displacement of the piston mode.

The power consumption is measured for both modes and the results are shown in **Figure**

6.5. The maximum power for the tilt-mode is 7.70 mW with the positive pulses, while the piston-mode is 21.32 mW. It is appropriate to compare the power consumptions of tilt mode and piston mode since for both of the cases, the maximum of motions (pitch/roll angles and piston displacement) are realized under the chosen high current steps (**Figure** 6.5). The power shown for the piston-mode is for the 4 legs, while the tilt mode is for only one leg. Assuming that each leg had the same resistive heater elements, then the required power per leg for the piston-mode would be 5.33 mW. The difference in maximum power between modes, demonstrates the effect of the non-actuated legs that oppose the movement and add an extrinsic stress to the actuated leg, in this case increasing the input power needed to induce the transition of the VO_2. If the extrinsic stress did not affect the VO_2, the maximum total power consumed by the piston mode would be expected to be approximately 4 four times larger than that for a single actuator in tilt-mode.

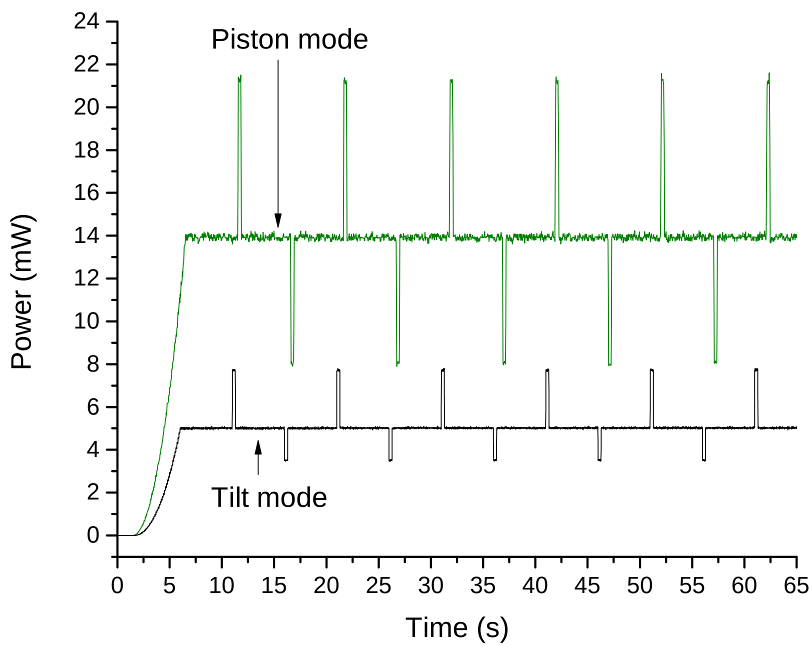

Figure 6.5 Consume power of the device for both mode (tilt and piston) during the programming of the 2-states.

Another experiment is conducted to demonstrate the repeatability of the programming action. By adding identical positive current pulses (i_+) to the pre-heating current i_{ph}, we are delivering programming pulses of the same power, which should result in the same programmed state at the end of each pulse. The results are shown in **Figure** 6.6. It should be noted, that the same state is reach with each pulse since the amplitude of the pulse produce an output that always goes into outer loop of the hysteresis. The results demonstrate that programming pulses of equal power will produce the same programmed state for both actuation mode: the tilt-mode at 0.408° ± 0.076° and 1.971° ± 0.075° for pitch and roll, respectively, and vertical displacement (piston-mode) at 29.885 µm ± 1.15 µm.

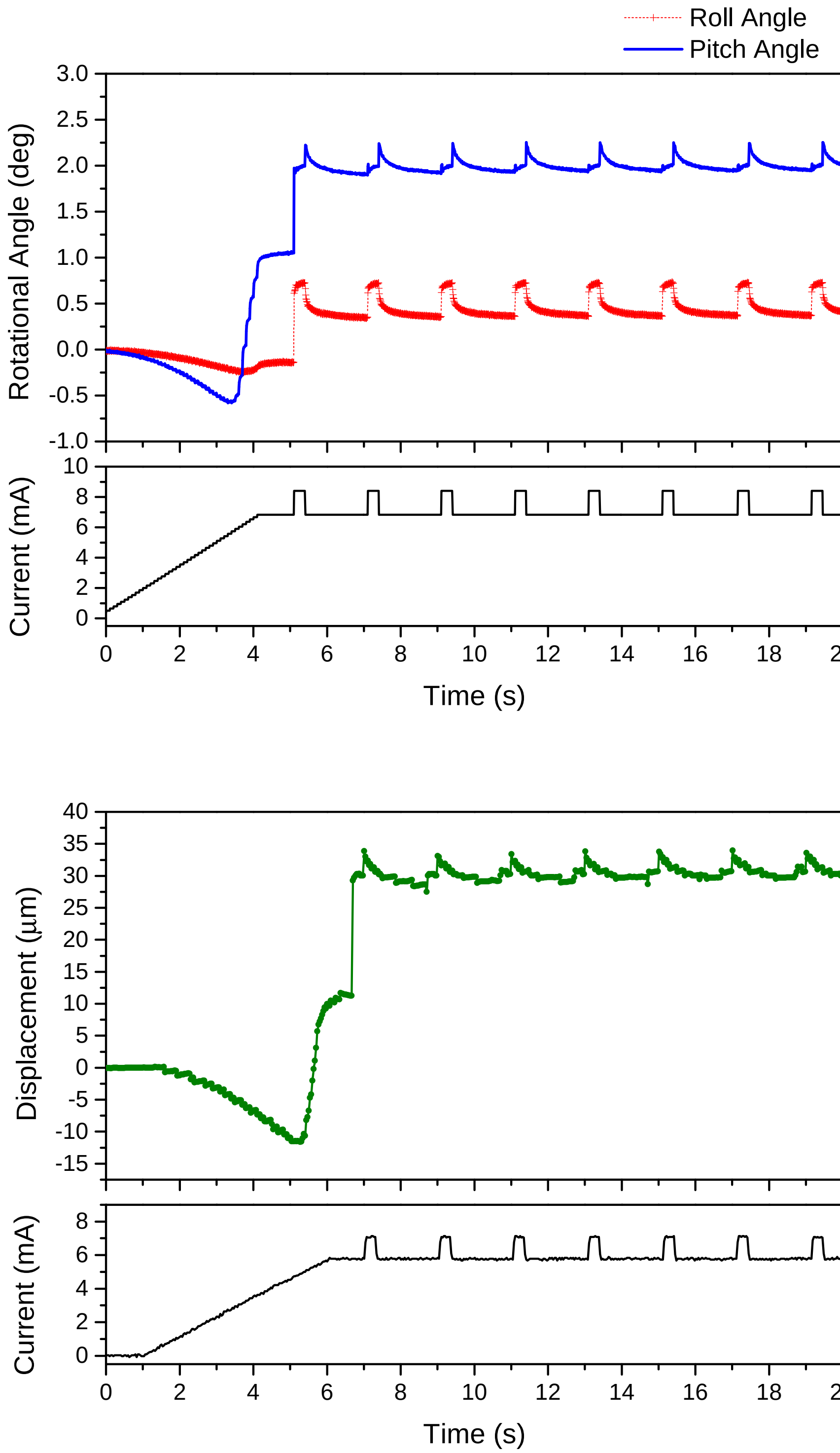

Figure 6.6 Programming of the high state by applying the same input pulse on the different modes: top) Rotational Angle of the tilt mode and, bottom) Vertical displacement of the piston mode.

The final experiment is aimed at demonstrating the capability to program different states from a single pre-heated state, for both actuation modes. For this, we applied programming current pulses of different magnitudes. The input is increased to the same pre-heated stage used for the other experiments (i_{ph}). Then, every 5 seconds a current pulse of different magnitudes is added to i_{ph}. Five different programmable states are obtained, including three resulting from positive pulses (i_+), followed by two from negative pulses (i_-). The results is shown in **Figure** 6.7. The number of programmed states can be increased by using different values of the pulse amplitude. These states are related to the pre-heated stage – different programmed states would have been obtained for a different pre-heated stage, even if applying the same programming pulses. This can be further exploited by achieving particular states using a model that describe the movement of the system, where a required current could be calculated to reach a desired state.

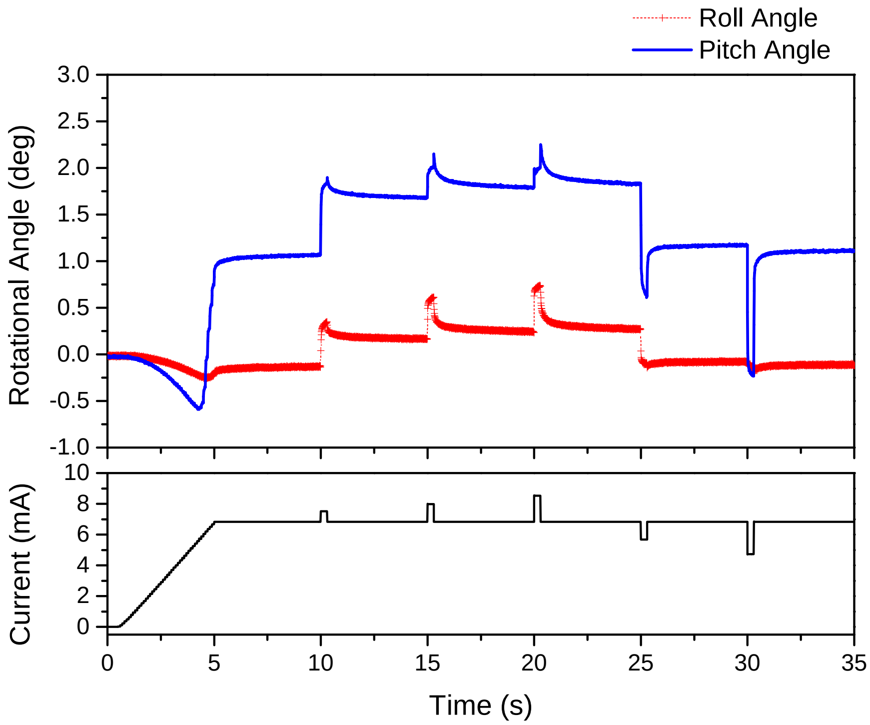

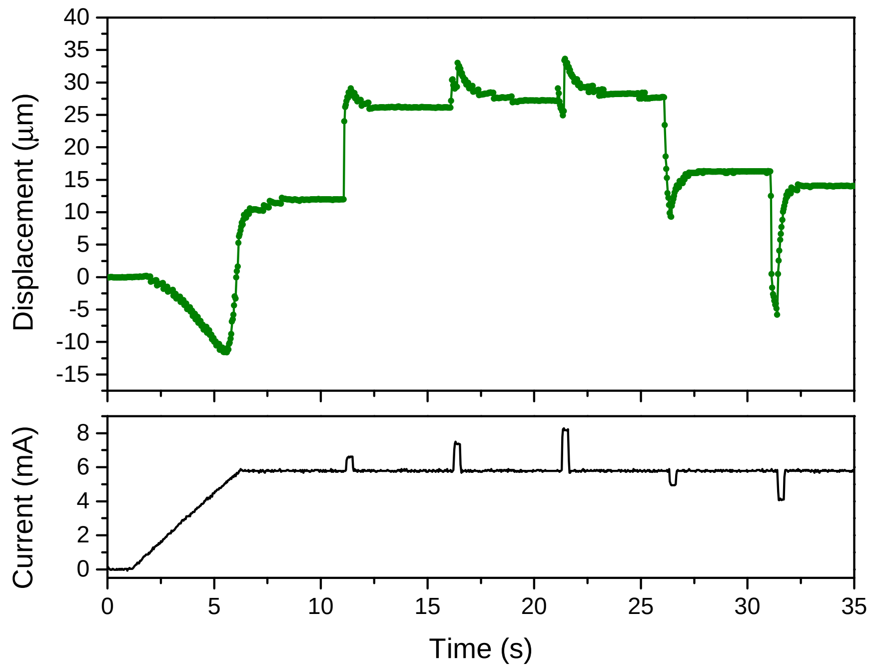

Figure 6.7 Programming of multiples states by applying different input pulse with different amplitudes on the different modes: top) Rotational Angle of the tilt mode and, bottom) vertical displacement of the piston mode.

6.2 Summary

A programmable MEMS mirror is presented in this work. The device is based on the solid-to-solid phase transition of VO_2, and has a lower actuation temperature than typical electrothermal MEMS mirrors based on thermal expansion coefficient mechanisms. Multiples mechanical states can be programmed in each of the two operating modes: tilt- and piston-mode. The tilt-mode consisted of two different angles: pitch and roll, while the piston-mode consisted of vertical displacements. Ideally, any tilting angle (for tilt-mode) or vertical displacement (for piston-mode) inside the major hysteretic loop of VO_2 can be programmed by using a specific programming pulse for a given pre-heated state.

CHAPTER 7

SUMMARY AND FUTURE WORK

7.1 Summary of Contributions

In this dissertation, the development of the first VO_2-based MEMS mirrors with integrated heaters is presented. A detailed set of studies that involved the characterization of VO_2-based devices in terms of total displacement and dynamic responses across the transition (for both, angular tilting rotation and vertical piston-like movement) were presented. A detailed design and fabrication process, which involved the use of FEM simulations, masks design, and clean-room fabrication, is presented. A mathematical model is derived from a series of simulations and experiments. From this, the lumped model of the system is extracted, such as the time response, the spring and the damping constant of the system. This model will not only enable future device control, but also develop a platform over which future devices can be designed. Finally, taking advantage of the intrinsic hysteretic behavior of the VO_2, different programmable mechanical states for angular tilting rotation and vertical piston-like movement were demonstrated by applying electrical pulses.

7.1.1 Problems Solved in this thesis

This work addresses the following:

- VO_2 thin films were successfully integrated into the design and fabrication of a MEMS mirror with monolithically integrated heaters.
- The fabrication of the VO_2-based MEMS mirror was optimized, with the fabrication of two generations, increasing the yield from 12.5% to 75%.

- VO_2-based MEMS mirror were characterized across the phase transition during individual actuation of each element (i.e. angular tilting rotation) and synchronous actuation of the 4 elements (i.e. vertical piston-like movement) in terms of quasi-static and dynamic responses.

- Increased energy efficiency of electrothermal MEMS mirror devices was demonstrated.

- A mathematical model that describes the movement of the VO_2-based MEMS mirror was derived based on theoretical simulations and experimental measurements of the device.

- A mathematical model that can serve as a platform for the design of future MEMS mirror devices operated by any electrothermal process was presented.

- Memory capabilities on the VO_2-based MEMS mirror were demonstrated, by programming the tilting angles and vertical displacement of the device using electrical pulses.

7.2 Future Work

The programming properties of the device will be further studied by achieving particular states using a quasi-static model of the system. The model will be used to calculate the required input to reach a desired output, where any particular output value within the hysteresis can be obtained. This would enable the programming of any particular mechanical state (within the hysteresis) of the device for any actuation mode: piston- and tilt-mode. Furthermore, this could be used as a platform for devices with hysteretic behavior to exploit the memory capabilities of each system.

BIBLIOGRAPHY

BIBLIOGRAPHY

[1] R. Cabrera, E. Merced, and N. Sepulveda, "Performance of electro-thermally driven-based MEMS actuators," *Microelectromechanical Systems, Journal of*, vol. 23, no. 1, pp. 243–251, 2014.

[2] S. T. S. Holmstrom, U. Baran, and H. Urey, "Mems laser scanners: A review," *Journal of Microelectromechanical Systems*, vol. 23, no. 2, pp. 259–275, 2014.

[3] L. Liu, L. Wu, J. Sun, E. Lin, and H. Xie, "Miniature endoscopic optical coherence tomography probe employing a two-axis microelectromechanical scanning mirror with through-silicon vias," *Journal of Biomedical Optics*, vol. 16, no. 2, pp. 026006–026006–4, 2011.

[4] L. J. Hornbeck, "The dmdtm projection display chip: A mems-based technology," *MRS Bulletin*, vol. 26, pp. 325–327, 4 2001.

[5] H. Xie, Y. Pan, and G. K. Fedder, "A cmos-mems mirror with curled-hinge comb drives," *Journal of Microelectromechanical Systems*, vol. 12, no. 4, pp. 450–457, 2003.

[6] H. Urey, "Mems scanners for display and imaging applications," vol. 5604, pp. 218–229, 2004.

[7] C. W. Tsai, H. T. Chang, S. H. Liu, and J. c. Tsai, "Magnetically-actuated swing-type mems mirror pair for a reconfigurable optical interconnect," *Journal of Lightwave Technology*, vol. 31, no. 24, pp. 4126–4134, 2013.

[8] M. Tani, M. Akamatsu, Y. Yasuda, H. Fujita, and H. Toshiyoshi, "A combination of fast resonant mode and slow static deflection of soi-pzt actuators for mems image projection display," in *Optical MEMS and Their Applications Conference, 2006. IEEE/LEOS International Conference on*, pp. 25–26, 2006.

[9] U. Baran, D. Brown, S. Holmstrom, D. Balma, W. O. Davis, P. Muralt, and H. Urey, "Resonant pzt mems scanner for high-resolution displays," *Journal of Microelectromechanical Systems*, vol. 21, no. 6, pp. 1303–1310, 2012.

[10] L. Wu, S. Dooley, E. Watson, P. F. McManamon, and H. Xie, "A tip-tilt-piston micromirror array for optical phased array applications," *Microelectromechanical Systems, Journal of*, vol. 19, no. 6, pp. 1450–1461, 2010.

[11] L. Wu and H. Xie, "A large vertical displacement electrothermal bimorph microactuator with very small lateral shift," *Sensors and Actuators A: Physical*, vol. 145, pp. 371–379, 2008.

[12] V. Eyert, "The metal-insulator transitions of vo2: A band theoretical approach," *Annalen der Physik*, vol. 11, no. 9, pp. 650–704, 2002.

[13] N. F. Quackenbush, J. W. Tashman, J. A. Mundy, S. Sallis, H. Paik, R. Misra, J. A. Moyer, J.-H. Guo, D. A. Fischer, J. C. Woicik, D. A. Muller, D. G. Schlom, and L. F. J. Piper, "Nature of the metal insulator transition in ultrathin epitaxial vanadium dioxide," *Nano Letters*, vol. 13, no. 10, pp. 4857–4861, 2013. PMID: 24000961.

[14] A. Rúa, F. l. E. Fernández, and N. Sepúlveda, "Bending in VO_2-coated microcantilevers suitable for thermally activated actuators," *Journal of Applied Physics*, vol. 107, no. 7, p. 074506, 2010.

[15] E. Merced, X. Tan, and N. Sepúlveda, "Strain energy density of VO_2-based microactuators," *Sensors and Actuators A: Physical*, vol. 196, pp. 30–37, 2013.

[16] T. Wang, D. Torres, F. E. Fernández, A. J. Green, C. Wang, and N. Sepúlveda, "Increasing efficiency, speed, and responsivity of vanadium dioxide based photothermally driven actuators using single-wall carbon nanotube thin-films," *ACS nano*, vol. 9, no. 4, pp. 4371–4378, 2015.

[17] R. Cabrera, E. Merced, and N. Sepúlveda, "A micro-electro-mechanical memory based on the structural phase transition of VO_2," *physica status solidi (a)*, vol. 210, no. 9, pp. 1704–1711, 2013.

[18] D. Torres, T. Wang, J. Zhang, X. Zhang, S. Dooley, X. Tan, H. Xie, and N. Seplveda, "Vo_2-based mems mirrors," *Journal of Microelectromechanical Systems*, vol. 25, pp. 780–787, Aug 2016.

[19] N. F. Mott and L. Friedman, "Metal-insulator transitions in vo2, ti2o3 and ti2-x v x o3," *Philosophical Magazine*, vol. 30, no. 2, pp. 389–402, 1974.

[20] A. Barker Jr, H. Verleur, and H. Guggenheim, "Infrared optical properties of vanadium dioxide above and below the transition temperature," *Physical Review Letters*, vol. 17, no. 26, p. 1286, 1966.

[21] N. Sepulveda, A. Rua, R. Cabrera, and F. Fernández, "Young's modulus of VO_2 thin films as a function of temperature including insulator-to-metal transition regime," *Applied Physics Letters*, vol. 92, no. 19, p. 1913, 2008.

[22] J. Cao, W. Fan, Q. Zhou, E. Sheu, A. Liu, C. Barrett, and J. Wu, "Colossal thermal-mechanical actuation via phase transition in single-crystal VO_2 microcantilevers," *Journal of Applied Physics*, vol. 108, no. 8, p. 083538, 2010.

[23] R. Cabrera, E. Merced, N. Davila, F. E. Fernndez, and N. Seplveda, "A multiple-state micro-mechanical programmable memory," *Microelectronic Engineering*, vol. 88, no. 11, pp. 3231 – 3234, 2011.

[24] E. Merced, R. Cabrera, N. Dávila, F. E. Fernández, and N. Sepúlveda, "A micro-mechanical resonator with programmable frequency capability," *Smart Materials and Structures*, vol. 21, no. 3, p. 035007, 2012.

[25] E. Merced, N. Davila, D. Torres, R. Cabrera, F. E. Fernndez, and N. Seplveda, "Photothermal actuation of v o 2 :cr-coated microcantilevers in air and aqueous media," *Smart Materials and Structures*, vol. 21, no. 10, p. 105009, 2012.

[26] A. Ra, R. Cabrera, H. Coy, E. Merced, N. Seplveda, and F. E. Fernndez, "Phase transition behavior in microcantilevers coated with m1-phase vo2 and m2-phase vo2:cr thin films," *Journal of Applied Physics*, vol. 111, no. 10, 2012.

[27] K. Liu, C. Cheng, Z. Cheng, K. Wang, R. Ramesh, and J. Wu, "Giant-amplitude, high-work density microactuators with phase transition activated nanolayer bimorphs," *Nano letters*, vol. 12, no. 12, pp. 6302–6308, 2012.

[28] J. Zhang, E. Merced, N. Sepúlveda, and X. Tan, "Modeling and inverse compensation of non-monotonic hysteresis in vo2-coated microactuators," *IEEE/ASME Transactions on Mechatronics*, vol. 19, no. 2, pp. 579–588, 2014.

[29] E. Merced, X. Tan, and N. Sepúlveda, "Closed-loop tracking of large displacements in electro-thermally actuated-based MEMS," *Microelectromechanical Systems, Journal of*, vol. 23, no. 5, pp. 1073–1083, 2014.

[30] E. Merced, D. Torres, X. Tan, and N. Sepúlveda, "An electrothermally actuated VO_2-based MEMS using self-sensing feedback control," *Microelectromechanical Systems, Journal of*, vol. 24, no. 1, pp. 100–107, 2015.

[31] S. D. Ha, Y. Zhou, A. E. Duwel, D. W. White, and S. Ramanathan, "Quick switch: Strongly correlated electronic phase transition systems for cutting-edge microwave devices," *IEEE Microwave Magazine*, vol. 6, no. 15, pp. 32–44, 2014.

[32] L. J. Hornbeck, "Digital light processing and mems: an overview," in *Advanced Applications of Lasers in Materials Processing/Broadband Optical Networks/Smart Pixels/Optical MEMs and Their Applications. IEEE/LEOS 1996 Summer Topical Meetings:*, pp. 7–8, 1996.

[33] R. Legtenberg, A. W. Groeneveld, and M. Elwenspoek, "Comb-drive actuators for large displacements," *Journal of Micromechanics and Microengineering*, vol. 6, no. 3, p. 320, 1996.

[34] S.-W. Chung and Y.-K. Kim, "Measurements of a fabricated micro mirror using a lateral-effect position-sensitive photodiode," *IEEE Transactions on Industrial Electronics*, vol. 45, no. 6, pp. 861–865, 1998.

[35] P. van Kessel, L. Hornbeck, R. Meier, and M. Douglass, "A MEMS-based projection display," *Proceedings of the IEEE*, vol. 86, no. 8, pp. 1687–1704, 1998.

[36] Y. Pan, H. Xie, and G. K. Fedder, "Endoscopic optical coherence tomography based on a microelectromechanical mirror," *Opt. Lett.*, vol. 26, no. 24, pp. 1966–1968, 2001.

[37] U. Krishnamoorthy, K. Li, K. Yu, D. Lee, J. Heritage, and O. Solgaard, "Dual-mode micromirrors for optical phased array applications," *Sensors and Actuators A: Physical*, vol. 97, pp. 21–26, 2002.

[38] A. Liu, X. Zhang, J. Li, and C. Lu, "Single-/multi-mode tunable lasers using {MEMS} mirror and grating," *Sensors and Actuators A: Physical*, vol. 108, no. 13, pp. 49 – 54, 2003. Selected Papers from the Pacific Rim Workshop on Transducers and Micro/Nano Technologies.

[39] D. S. Greywall, P. A. Busch, F. Pardo, D. W. Carr, G. Bogart, and H. T. Soh, "Crystalline silicon tilting mirrors for optical cross-connect switches," *Journal of Microelectromechanical Systems*, vol. 12, no. 5, pp. 708–712, 2003.

[40] W. P. Taylor, J. J. Bernstein, J. D. Brazzle, and C. J. Corcoran, "Magnet arrays for use in a 3-d mems mirror array for optical switching," *IEEE Transactions on Magnetics*, vol. 39, no. 5, pp. 3286–3288, 2003.

[41] H. Miyajima, N. Asaoka, T. Isokawa, M. Ogata, Y. Aoki, M. Imai, O. Fujimori, M. Katashiro, and K. Matsumoto, "A mems electromagnetic optical scanner for a commercial confocal laser scanning microscope," *Journal of Microelectromechanical Systems*, vol. 12, no. 3, pp. 243–251, 2003.

[42] J. J. Bernstein, W. P. Taylor, J. D. Brazzle, C. J. Corcoran, G. Kirkos, J. E. Odhner, A. Pareek, M. Waelti, and M. Zai, "Electromagnetically actuated mirror arrays for use in 3-d optical switching applications," *Journal of Microelectromechanical Systems*, vol. 13, no. 3, pp. 526–535, 2004.

[43] C. Pu, S. Park, P. B. Chu, S.-S. Lee, M. Tsai, D. Peale, N. H. Bonadeo, and I. Brener, "Electrostatic actuation of three-dimensional mems mirrors using sidewall electrodes," *IEEE Journal of Selected Topics in Quantum Electronics*, vol. 10, no. 3, pp. 472–477, 2004.

[44] D. A. Horsley, W. O. Davis, K. J. Hogan, M. R. Hart, E. C. Ying, M. Chaparala, B. Behin, M. J. Daneman, and M.-H. Kiang, "Optical and mechanical performance of a novel magnetically actuated mems-based optical switch," *Journal of Microelectromechanical Systems*, vol. 14, no. 2, pp. 274–284, 2005.

[45] A. Jain, H. Qu, S. Todd, and H. Xie, "A thermal bimorph micromirror with large bi-directional and vertical actuation," *Sensors and Actuators A: Physical*, vol. 122, no. 1, pp. 9–15, 2005.

[46] H. Xie, S. Todd, A. Jain, and G. K. Fedder, *MEMS/NEMS: Handbook Techniques and Applications*, ch. Single-Crystal Silicon Based Electrothermal MEMS Mirrors for Biomedical Imaging Applications, pp. 1429–1471. Boston, MA: Springer US, 2006.

[47] J. C. Tsai and M. C. Wu, "Design, fabrication, and characterization of a high fill-factor, large scan-angle, two-axis scanner array driven by a leverage mechanism," *Journal of Microelectromechanical Systems*, vol. 15, no. 5, pp. 1209–1213, 2006.

[48] A. D. Yalcinkaya, H. Urey, D. Brown, T. Montague, and R. Sprague, "Two-axis electromagnetic microscanner for high resolution displays," *Journal of Microelectromechanical Systems*, vol. 15, no. 4, pp. 786–794, 2006.

[49] C. Lee, F. L. Hsiao, T. Kobayashi, K. H. Koh, P. V. Ramana, W. Xiang, B. Yang, C. W. Tan, and D. Pinjala, "A 1-v operated mems variable optical attenuator using piezoelectric pzt thin-film actuators," *IEEE Journal of Selected Topics in Quantum Electronics*, vol. 15, no. 5, pp. 1529–1536, 2009.

[50] P. F. McManamon, P. J. Bos, M. J. Escuti, J. Heikenfeld, S. Serati, H. Xie, and E. A. Watson, "A review of phased array steering for narrow-band electrooptical systems," *Proceedings of the IEEE*, vol. 97, no. 6, pp. 1078–1096, 2009.

[51] L. Wu, A. Pais, S. Samuelson, S. Guo, and H. Xie, "A mirror-tilt-insensitive fourier transform spectrometer based on a large vertical displacement micromirror with dual reflective surface," in *Solid-State Sensors, Actuators and Microsystems Conference, 2009. TRANSDUCERS 2009. International*, pp. 2090–2093, 2009.

[52] C. d. Liao and J. c. Tsai, "The evolution of mems displays," *IEEE Transactions on Industrial Electronics*, vol. 56, no. 4, pp. 1057–1065, 2009.

[53] E. E. Aktakka, R. L. Peterson, and K. Najafi, "A cmos-compatible piezoelectric vibration energy scavenger based on the integration of bulk pzt films on silicon," in *Electron Devices Meeting (IEDM), 2010 IEEE International*, pp. 31.5.1–31.5.4, 2010.

[54] Y. Bai, J. T. W. Yeow, P. Constantinou, S. Damaskinos, and B. C. Wilson, "A 2-d micromachined soi mems mirror with sidewall electrodes for biomedical imaging," *IEEE/ASME Transactions on Mechatronics*, vol. 15, no. 4, pp. 501–510, 2010.

[55] J. Sun and H. Xie, "Mems-based endoscopic optical coherence tomography," *International Journal of Optics*, vol. 2011, no. 825629, p. 12, 2011.

[56] K. A. G. Prakash, S. Dhabai, E. Bhattacharya, and S. Bhattacharya, "Design and fabrication of a micro-mirror for low-resolution spectroscopy," *IEEE Sensors Journal*, vol. 11, no. 4, pp. 1019–1025, 2011.

[57] S. Samuelson, L. Wu, J. Sun, S. woon Choe, B. Sorg, and H. Xie, "A 2.8-mm imaging probe based on a high-fill-factor mems mirror and wire-bonding-free packaging for endoscopic optical coherence tomography," *Microelectromechanical Systems, Journal of*, vol. 21, no. 6, pp. 1291–1302, 2012.

[58] K. H. Koh and C. Lee, "A two-dimensional mems scanning mirror using hybrid actuation mechanisms with low operation voltage," *Journal of Microelectromechanical Systems*, vol. 21, no. 5, pp. 1124–1135, 2012.

[59] U. Hofmann, J. Janes, and H.-J. Quenzer, "High-q mems resonators for laser beam scanning displays," *Micromachines*, vol. 3, no. 2, p. 509, 2012.

[60] D. Wang, L. Fu, X. Wang, Z. Gong, S. Samuelson, C. Duan, H. Jia, J. S. Ma, and H. Xie, "Endoscopic swept-source optical coherence tomography based on a two-axis microelectromechanical system mirror," *Journal of biomedical optics*, vol. 18, no. 8, pp. 086005–086005, 2013.

[61] O. Solgaard, A. A. Godil, R. T. Howe, L. P. Lee, Y. A. Peter, and H. Zappe, "Optical mems: From micromirrors to complex systems," *Journal of Microelectromechanical Systems*, vol. 23, no. 3, pp. 517–538, 2014.

[62] S. R. Samuelson and H. Xie, "A large piston displacement mems mirror with electrothermal ladder actuator arrays for ultra-low tilt applications," *Journal of Microelectromechanical Systems*, vol. 23, no. 1, pp. 39–49, 2014.

[63] L. Y. Lin and E. G. Keeler, "Progress of MEMS scanning micromirrors for optical bio-imaging," *Micromachines*, vol. 6, no. 11, pp. 1675–1689, 2015.

[64] A. R. Cho, A. Han, S. Ju, H. Jeong, J.-H. Park, I. Kim, J.-U. Bu, and C.-H. Ji, "Electromagnetic biaxial microscanner with mechanical amplification at resonance," *Optics express*, vol. 23, no. 13, pp. 16792–16802, 2015.

[65] A. C.-L. Hung, H. Y.-H. Lai, T.-W. Lin, S.-G. Fu, and M. S.-C. Lu, "An electrostatically driven 2D micro-scanning mirror with capacitive sensing for projection display," *Sensors and Actuators A: Physical*, vol. 222, pp. 122–129, 2015.

[66] T. Naono, T. Fujii, M. Esashi, and S. Tanaka, "Non-resonant 2-D piezoelectric MEMS optical scanner actuated by Nb doped PZT thin film," *Sensors and Actuators A: Physical*, vol. 233, pp. 147–157, 2015.

[67] J. Yang, X. Deng, and T. Chong, "An electro-thermal bimorph-based microactuator for precise track-positioning of optical disk drives," *Journal of Micromechanics and Microengineering*, vol. 15, no. 5, p. 958, 2005.

[68] F. Han, W. Wang, X. Zhang, and H. Xie, "Modeling and control of a large-stroke electrothermal mems mirror for fourier transform microspectrometers," *Journal of Microelectromechanical Systems*, vol. 25, pp. 750–760, Aug 2016.

[69] C. Giles, V. Aksyuk, B. Barber, R. Ruel, L. Stulz, and D. Bishop, "A silicon MEMS optical switch attenuator and its use in lightwave subsystems," *Selected Topics in Quantum Electronics, IEEE Journal of*, vol. 5, no. 1, pp. 18–25, 1999.

[70] J.-c. Tsai and M. C. Wu, "Design, fabrication, and characterization of a high fill-factor, large scan-angle, two-axis scanner array driven by a leverage mechanism," *Microelectromechanical Systems, Journal of*, vol. 15, no. 5, pp. 1209–1213, 2006.

[71] H. Ra, W. Piyawattanametha, M. J. Mandella, P.-L. Hsiung, J. Hardy, T. D. Wang, C. H. Contag, G. S. Kino, and O. Solgaard, "Three-dimensional in vivo imaging by a handheld dual-axes confocal microscope," *Optics express*, vol. 16, no. 10, pp. 7224–7232, 2008.

[72] L. Liu, E. Wang, X. Zhang, W. Liang, X. Li, and H. Xie, "Mems-based 3d confocal scanning microendoscope using mems scanners for both lateral and axial scan," *Sensors and Actuators A: Physical*, vol. 215, pp. 89–95, 2014.

[73] H. Xie, Y. Pan, and G. K. Fedder, "A cmos-mems mirror with curled-hinge comb drives," *Journal of Microelectromechanical Systems*, vol. 12, pp. 450–457, Aug 2003.

[74] E. S. Hung and S. D. Senturia, "Extending the travel range of analog-tuned electrostatic actuators," *Journal of Microelectromechanical Systems*, vol. 8, no. 4, pp. 497–505, 1999.

[75] A. Alabqari and B. Y. Majlis, "Electrostatic pull-in behavior in 50g force balanced mems accelerometer," in *Semiconductor Electronics, 2004. ICSE 2004. IEEE International Conference on*, pp. 5 pp.–, 2004.

[76] B. Ahmad and R. Pratap, "Elasto-electrostatic analysis of circular microplates used in capacitive micromachined ultrasonic transducers," *IEEE Sensors Journal*, vol. 10, no. 11, pp. 1767–1773, 2010.

[77] K. H. Koh, T. Kobayashi, and C. Lee, "A 2-d mems scanning mirror based on dynamic mixed mode excitation of a piezoelectric pzt thin film s-shaped actuator," *Opt. Express*, vol. 19, pp. 13812–13824, Jul 2011.

[78] S. Tadigadapa and K. Mateti, "Piezoelectric mems sensors: state-of-the-art and perspectives," *Measurement Science and technology*, vol. 20, no. 9, p. 092001, 2009.

[79] S. T. Todd and H. Xie, "An electrothermomechanical lumped element model of an electrothermal bimorph actuator," *Journal of Microelectromechanical Systems*, vol. 17, no. 1, pp. 213–225, 2008.

[80] H. Xie, "Vertical displacement device," Sept. 6 2005. US Patent 6,940,630.

[81] F. Morin, "Oxides which show a metal-to-insulator transition at the neel temperature," *Physical Review Letters*, vol. 3, no. 1, pp. 34–36, 1959.

[82] A. Zylbersztejn and N. Mott, "Metal-insulator transition in vanadium dioxide," *Physical Review B*, vol. 11, no. 11, p. 4383, 1975.

[83] J. Nag, R. F. Haglund, E. Andrew Payzant, and K. L. More, "Non-congruence of thermally driven structural and electronic transitions in vo2," *Journal of Applied Physics*, vol. 112, no. 10, 2012.

[84] P. Dernier, "Structural investigation of the metal-insulator transition in {V6O13}," *Materials Research Bulletin*, vol. 9, no. 7, pp. 955 – 963, 1974.

[85] J. Feinleib and W. Paul, "Semiconductor-to-metal transition in v_2o_3," *Phys. Rev.*, vol. 155, pp. 841–850, Mar 1967.

[86] K. Kosuge, "The phase diagram and phase transition of the v2o3v2o5, system," *Journal of Physics and Chemistry of Solids*, vol. 28, no. 8, pp. 1613 – 1621, 1967.

[87] W. Burkhardt, T. Christmann, B. Meyer, W. Niessner, D. Schalch, and A. Scharmann, "W- and f-doped {VO2} films studied by photoelectron spectrometry," *Thin Solid Films*, vol. 345, no. 2, pp. 229 – 235, 1999.

[88] S. Kabashima, T. Goto, K. Nishimura, and T. Kawakubo, "Impurity conduction in ti-doped vo2 studied by microwave frequency conductivity," *Journal of the Physical Society of Japan*, vol. 32, no. 1, pp. 158–163, 1972.

[89] M. Marezio, D. B. McWhan, J. P. Remeika, and P. D. Dernier, "Structural aspects of the metal-insulator transitions in cr-doped vo_2," *Phys. Rev. B*, vol. 5, pp. 2541–2551, 1972.

[90] T. Phillips, R. Murphy, and T. Poehler, "Electrical studies of reactively sputtered fe-doped {VO2} thin films," *Materials Research Bulletin*, vol. 22, no. 8, pp. 1113 – 1123, 1987.

[91] J. MacChesney and H. Guggenheim, "Growth and electrical properties of vanadium dioxide single crystals containing selected impurity ions," *Journal of Physics and Chemistry of Solids*, vol. 30, no. 2, pp. 225 – 234, 1969.

[92] S. Lysenko, V. Vikhnin, G. Zhang, A. Rua, F. Fernandez, and H. Liu, "Insulator-to-metal phase transformation of vo2 films upon femtosecond laser excitation," *Journal of Electronic Materials*, vol. 35, no. 10, pp. 1866–1872, 2006.

[93] G. Stefanovich, A. Pergament, and D. Stefanovich, "Electrical switching and mott transition in vo 2," *Journal of Physics: Condensed Matter*, vol. 12, no. 41, p. 8837, 2000.

[94] E. Arcangeletti, L. Baldassarre, D. Di Castro, S. Lupi, L. Malavasi, C. Marini, A. Perucchi, and P. Postorino, "Evidence of a pressure-induced metallization process in monoclinic vo_2," *Phys. Rev. Lett.*, vol. 98, p. 196406, 2007.

[95] J. Cao, Y. Gu, W. Fan, L. Chen, D. Ogletree, K. Chen, N. Tamura, M. Kunz, C. Barrett, J. Seidel, *et al.*, "Extended mapping and exploration of the vanadium dioxide stress-temperature phase diagram," *Nano letters*, vol. 10, no. 7, pp. 2667–2673, 2010.

[96] K. Y. Tsai, T.-S. Chin, H.-P. D. Shieh, and C. H. Ma, "Effect of as-deposited residual stress on transition temperatures of vo2 thin films," *Journal of Materials Research*, vol. 19, pp. 2306–2314, 008 2004.

[97] F. C. Case, "Modifications in the phase transition properties of predeposited vo2 films," *Journal of Vacuum Science & Technology A: Vacuum, Surfaces, and Films*, vol. 2, no. 4, pp. 1509–1512, 1984.

[98] T. Maruyama and Y. Ikuta, "Vanadium dioxide thin films prepared by chemical vapour deposition from vanadium(iii) acetylacetonate," *Journal of Materials Science*, vol. 28, no. 18, pp. 5073–5078, 1993.

[99] J. Nag and R. F. H. Jr, "Synthesis of vanadium dioxide thin films and nanoparticles," *Journal of Physics: Condensed Matter*, vol. 20, no. 26, p. 264016, 2008.

[100] D. Yin, N. Xu, J. Zhang, and X. Zheng, "High quality vanadium dioxide films prepared by an inorganic sol-gel method," *Materials Research Bulletin*, vol. 31, no. 3, pp. 335 – 340, 1996.

[101] T. Hanlon, J. Coath, and M. Richardson, "Molybdenum-doped vanadium dioxide coatings on glass produced by the aqueous solgel method," *Thin Solid Films*, vol. 436, no. 2, pp. 269 – 272, 2003.

[102] K. Speck, H.-W. Hu, M. Sherwin, and R. Potember, "Vanadium dioxide films grown from vanadium tetra-isopropoxide by the sol-gel process," *Thin Solid Films*, vol. 165, no. 1, pp. 317 – 322, 1988.

[103] M. E. A. Warwick and R. Binions, "Advances in thermochromic vanadium dioxide films," *J. Mater. Chem. A*, vol. 2, pp. 3275–3292, 2014.

[104] T. Blanquart, J. Niinisto, M. Gavagnin, V. Longo, M. Heikkila, E. Puukilainen, V. R. Pallem, C. Dussarrat, M. Ritala, and M. Leskela, "Atomic layer deposition and characterization of vanadium oxide thin films," *RSC Adv.*, vol. 3, pp. 1179–1185, 2013.

[105] M. Borek, F. Qian, V. Nagabushnam, and R. K. Singh, "Pulsed laser deposition of oriented vo2 thin films on rcut sapphire substrates," *Applied Physics Letters*, vol. 63, no. 24, pp. 3288–3290, 1993.

[106] D. H. Kim and H. S. Kwok, "Pulsed laser deposition of vo2 thin films," *Applied Physics Letters*, vol. 65, no. 25, pp. 3188–3190, 1994.

[107] C. V. Ramana, R. J. Smith, and O. M. Hussain, "Grain size effects on the optical characteristics of pulsed-laser deposited vanadium oxide thin films," *physica status solidi (a)*, vol. 199, no. 1, pp. R4–R6, 2003.

[108] G. A. Rozgonyi and D. H. Hensler, "Structural and electrical properties of vanadium dioxide thin films," *Journal of Vacuum Science and Technology*, vol. 5, no. 6, pp. 194–199, 1968.

[109] S. J. Yun, J. W. Lim, J.-S. Noh, B.-G. Chae, and H.-T. Kim, "Vanadium dioxide films deposited on amorphous sio 2 - and al 2 o 3 -coated si substrates by reactive rf-magnetron sputter deposition," *Japanese Journal of Applied Physics*, vol. 47, no. 4S, p. 3067, 2008.

[110] H. Coy, R. Cabrera, N. Seplveda, and F. E. Fernndez, "Optoelectronic and all-optical multiple memory states in vanadium dioxide," *Journal of Applied Physics*, vol. 108, no. 11, 2010.

[111] A. Ra, F. E. Fernndez, M. A. Hines, and N. Seplveda, "Study of the resonant frequencies of silicon microcantilevers coated with vanadium dioxide films during the insulator-to-metal transition," *Journal of Applied Physics*, vol. 107, no. 5, 2010.

[112] N. Davila, E. Merced, and N. Sepulveda, "Electronically variable optical attenuator enabled by self-sensing in vanadium dioxide," *IEEE Photonics Technology Letters*, vol. 26, no. 10, pp. 1011–1014, 2014.

[113] R. Cabreara-Pizarro and N. Sepulveda-Alancastro, "Voltage-controlled resistor based on phase transition materials," Jan. 21 2016. US Patent App. 14/774,217.

[114] T. S. Teeslink, D. Torres, J. L. Ebel, N. Sepúlveda, and D. E. Anagnostou, "Reconfigurable bowtie antenna using metal-insulator transition in vanadium dioxide," *IEEE Antennas and Wireless Propagation Letters*, vol. 14, pp. 1381–1384, 2015.

[115] J. Laverock, A. R. H. Preston, D. Newby, K. E. Smith, S. Sallis, L. F. J. Piper, S. Kittiwatanakul, J. W. Lu, S. A. Wolf, M. Leandersson, and T. Balasubramanian, "Photoemission evidence for crossover from peierls-like to mott-like transition in highly strained vo_2," *Phys. Rev. B*, vol. 86, p. 195124, Nov 2012.

[116] J. Zhang, E. Merced, N. Seplúveda, and X. Tan, "Modeling and inverse compensation of hysteresis in vanadium dioxide using an extended generalized prandtlishlinskii model," *Smart Materials and Structures*, vol. 23, no. 12, p. 125017, 2014.

[117] H. Takeuchi, A. Wung, X. Sun, R. T. Howe, and T.-J. King, "Thermal budget limits of quarter-micrometer foundry cmos for post-processing mems devices," *IEEE Transactions on Electron Devices*, vol. 52, no. 9, pp. 2081–2086, 2005.

[118] L. Zhang, J. Tsaur, and R. Maeda, "Residual stress study of sio 2 /pt/pb(zr,ti)o 3 /pt multilayer structure for micro electro mechanical system applications," *Japanese Journal of Applied Physics*, vol. 42, no. 3R, p. 1386, 2003.

[119] Y. Matsui, M. Hiratani, Y. Kumagai, H. Miura, and Y. Fujisaki, "Thermal stability of pt bottom electrodes for ferroelectric capacitors," *Japanese Journal of Applied Physics*, vol. 37, no. 4B, p. L465, 1998.

[120] A. Kinbara and H. Haraki, "Internal stress of evaporated thin gold films," *Japanese Journal of Applied Physics*, vol. 4, no. 4, p. 243, 1965.

[121] B. Kebabi, C. Malek, and F. Ladan, "Stress and microstructure relationships in gold thin films," *Vacuum*, vol. 41, no. 46, pp. 1353 – 1355, 1990. Selected proceedings of the 11th international vacuum congress (IVC-11) 7th international conference on solid surfaces (ICSS-7).

[122] Y. Bai, J. T. W. Yeow, and B. C. Wilson, "A characteristic study of micromirror with sidewall electrodes," *International Journal of Optomechatronics*, vol. 1, no. 3, pp. 231–258, 2007.

[123] S. O. Isikman and H. Urey, "Dynamic modeling of soft magnetic film actuated scanners," *IEEE Transactions on Magnetics*, vol. 45, pp. 2912–2919, July 2009.

[124] J. Zhang, E. Merced, N. Sepúlveda, and X. Tan, "Optimal compression of generalized prandtl–ishlinskii hysteresis models," *Automatica*, vol. 57, pp. 170–179, 2015.

[125] J. Zhang, D. Torres, J. L. Ebel, N. Sepúlveda, and X. Tan, "A composite hysteresis model in self-sensing feedback control of fully integrated VO_2 microactuators," *IEEE/ASME Transactions on Mechatronics*, vol. 21, pp. 2405–2417, Oct 2016.

[126] D. J. Leo, *Engineering analysis of smart material systems.* John Wiley & Sons, 2007.

[127] I. Mayergoyz, *Mathematical models of hysteresis and their applications.* Springer-Verlag, 1991.

[128] X. Tan and J. Baras, "Modeling and control of hysteresis in magnetostrictive actuators," *Automatica*, vol. 40, no. 9, pp. 1469–1480, 2004.

[129] K. Gall, M. L. Dunn, Y. Zhang, and B. A. Corff, "Thermal cycling response of layered gold/polysilicon {MEMS} structures," *Mechanics of Materials*, vol. 36, no. 12, pp. 45 – 55, 2004. Fatigue of Advanced Materials.

[130] K. Gall, N. West, K. Spark, M. L. Dunn, and D. S. Finch, "Creep of thin film au on bimaterial au/si microcantilevers," *Acta Materialia*, vol. 52, no. 8, pp. 2133 – 2146, 2004.

[131] D. Qu and H. Shi, "Studies of activated carbons used in double-layer capacitors," *Journal of Power Sources*, vol. 74, no. 1, pp. 99 – 107, 1998.

[132] P. F. Ribeiro, B. K. Johnson, M. L. Crow, A. Arsoy, and Y. Liu, "Energy storage systems for advanced power applications," *Proceedings of the IEEE*, vol. 89, pp. 1744–1756, Dec 2001.

[133] W. W. Jang, J. O. Lee, H.-H. Yang, and J.-B. Yoon, "Mechanically operated random access memory (moram) based on an electrostatic microswitch for nonvolatile memory applications," *IEEE Transactions on Electron Devices*, vol. 55, no. 10, pp. 2785–2789, 2008.

[134] N. Abele, A. Villaret, A. Gangadharaiah, C. Gabioud, P. Ancey, and A. M. Ionescu, "1t mems memory based on suspended gate mosfet," in *2006 International Electron Devices Meeting*, pp. 1–4, Dec 2006.

[135] S. W. Lee, S. J. Park, E. E. Campbell, and Y. W. Park, "A fast and low-power microelectromechanical system-based non-volatile memory device," *Nature communications*, vol. 2, p. 220, 2011.

[136] A. Yao and T. Hikihara, "Logic-memory device of a mechanical resonator," *Applied Physics Letters*, vol. 105, no. 12, p. 123104, 2014.

[137] B. Charlot, W. Sun, K. Yamashita, H. Fujita, and H. Toshiyoshi, "Bistable nanowire for micromechanical memory," *Journal of Micromechanics and Microengineering*, vol. 18, no. 4, p. 045005, 2008.

[138] S. Krylov, B. R. Ilic, and S. Lulinsky, "Bistability of curved microbeams actuated by fringing electrostatic fields," *Nonlinear Dynamics*, vol. 66, no. 3, p. 403, 2011.

[139] R. Cabrera, E. Merced, N. Sepúlveda, and F. E. Fernández, "Dynamics of photothermally driven vo2-coated microcantilevers," *Journal of Applied Physics*, 2011.